The Leading Edge®

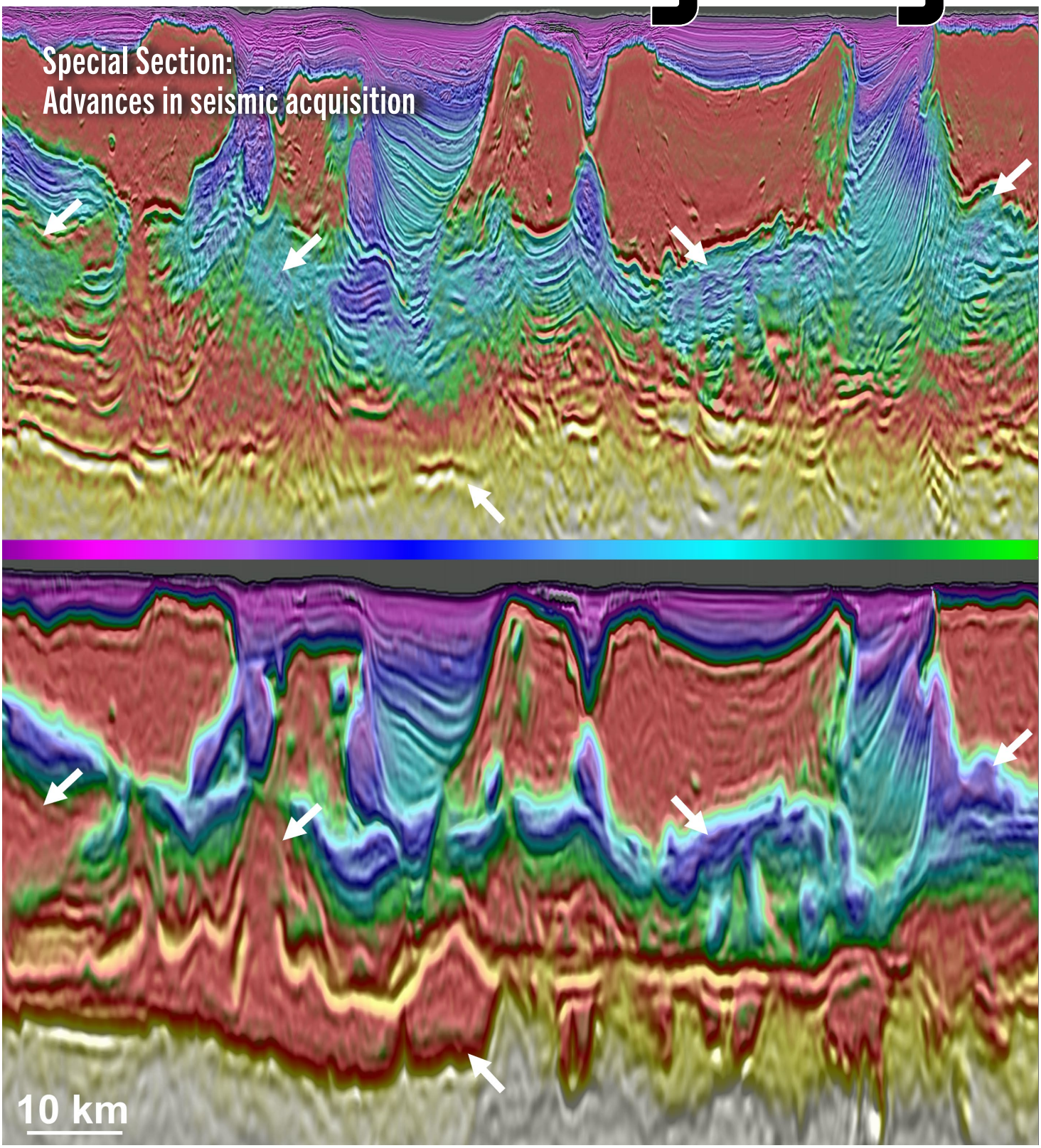

SEG SOCIETY OF EXPLORATION GEOPHYSICISTS

February 2026 · Volume 45, No. 2
ISSN 1070-485X

Downloaded from http://pubs.geoscienceworld.org/seg/tle/article-pdf/45/2/73/7765650/tle-v45-n2.pdf by Shivaji Maitra on 19 February 2026

SERCEL
A Viridien Business

TPS
(TUNED PULSE SOURCE)

Better, Safer, Greener.

INNOVATIVE LOW FREQUENCY BROADBAND MARINE SEISMIC SOURCE

TPS provides geophysical clarity by enhancing the quality and value of seismic data and enabling effective imaging of the most complex geologies.

Image Better
- Improved imaging under salt and basalt.
- Elimination of local minima in Full Waveform Inversion and improved resolution.
- Reduced dependency on well logs in building blocky reservoir models.

Stay Safer
- Safer deployment, retrieval and prevention of auto-fires.

Be Greener
- Reduced high-frequency and sound pressure exposure levels.
- Exclusion zone reduction and lower duty cycle.

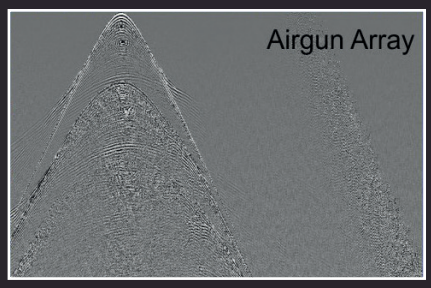

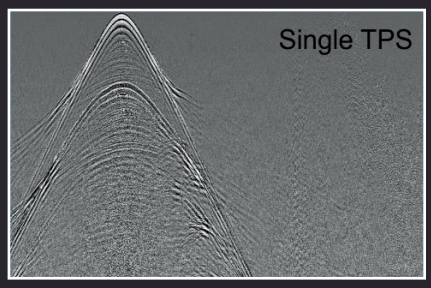



#TrueFidelity #TrueBroadband

For more information

Nantes, France
sales.nantes@sercel.com

Houston, USA
sales.houston@sercel.com

www.sercel.com

Downloaded from http://pubs.geoscienceworld.org/seg/tle/article-pdf/45/2/73/7765650/tle-v45-n2.pdf by Shivaji Maitra on 19 February 2026

SPE · AAPG · SEG

CCUS

Carbon Capture, Utilization, and Storage



From Capture to Storage:
Your Ideas Guide the Future

Register by 17 February and Save Up to $210

Waterway Marriott Hotel & Convention Center, The Woodlands, TX
30 March–1 April 2026

CCUSevent.org

Sponsoring Organizations

SPE International · AAPG · SEG

Downloaded from http://pubs.geoscienceworld.org/seg/tle/article-pdf/45/2/73/7765650/tle-v45-n2.pdf by Shivaji Maitra on 19 February 2026

DUG ELASTIC MP-FWI IMAGING IS HERE

SHEAR BRILLIANCE

Conventional Workflow

TIME PROCESSING, DEPTH IMAGING AND AVA INVERSION

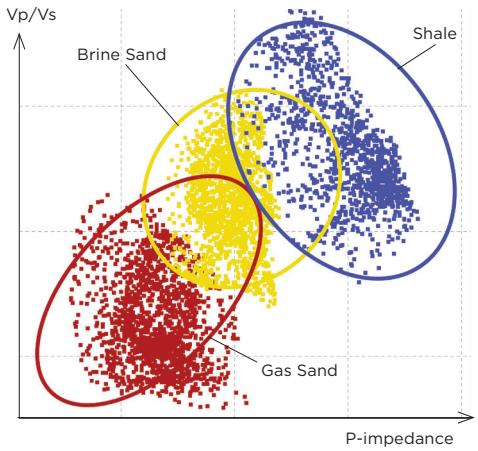

DUG Elastic MP-FWI Imaging

USING FIELD-DATA INPUT

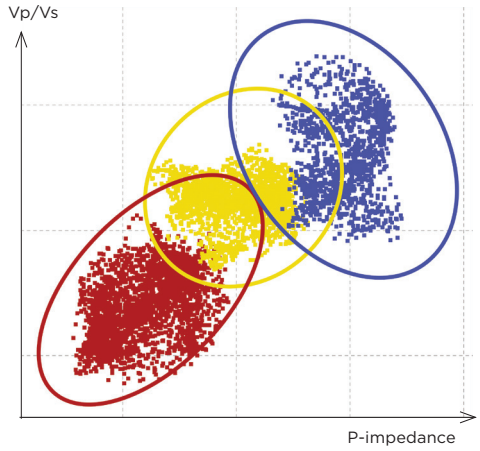

LESS SCATTER = LESS UNCERTAINTY!

BEX MC3D DATASET COURTESY OF DUG MULTI-CLIENT

Quantitative interpretation requires true amplitudes and high signal-to-noise ratio.

DUG Elastic MP-FWI Imaging eliminates the need for conventional time processing, depth imaging and AVA inversion workflows, along with their assumptions that ultimately affect AVA compliance. With DUG Elastic MP-FWI Imaging more certain predictions can be realised — all using field-data input. Brilliant!

INCLUDED IN DUG INSIGHT!

dug

info@dug.com | dug.com/fwi

Downloaded from http://pubs.geoscienceworld.org/seg/tle/article-pdf/45/2/73/7765650/tle-v45-n2.pdf by Shivaji Maitra on 19 February 2026

Table of Contents

Special Section: Advances in seismic acquisition

80 ..... **Introduction to this special section: Advances in seismic acquisition**
R. Neelamani, S. Maitra, S. Kumar, and F. Akasyah Ghazali

81 ..... **Advancing subsalt imaging in the US Gulf: Operational and technical innovations in seismic data acquisition from the Laconia sparse OBN program**
R. De Marco Centeno, S. Ji, Z. Yang, R. Flower, B. Wray, H. Zhu, S. Ronen and P. Wentzler

91 ..... **Enhancing deep pre-carbonate imaging with DAS VSP mode-converted energy: Unlocking deeper exploration potential in the prolific Asia Pacific basins**
R. Alai, A. Riza Ghazali, F. Akasyah Ghazali, M. Heng Pua, E. B. Kamarudin, G. B. Malo–Paul, H. Farhana Hasnan, G. Coskun, Y. Bt M. Sufian, S. Kumar, M. Rizam Sarif, K. H. B. Khalid, M. Preston, S. Dong, G. Zhan, F. Liu, R. Collings, S. Shaw, and O. Barrios–Lopez

98 ..... **Compressive sensing for seismic: From survey design to legacy data reconstruction**
T. Jiang, J. Latchman, P. Eick, C. Meng L. E. Chuan, M. N. B M Isa, R. Burr, J. Woolley and J. Zhu

109 ..... **Unlocking the potential of blended acquisition with independent simultaneous sourcing and dispersed source array onshore Abu Dhabi**
T. Ishiyama and A. Aljaberi

117 ..... **Self-supervised vision transformers for classification in unconventional shales**
R. Darwis Mohammad, D. Devegowda, M. Curtis, C. Rai, S. Mudduluru and S. Kiran Maryada

Departments

77 ..... Editorial Calendar
78 ..... President's Page
133 ..... Reviews
134 ..... Memorial
137 ..... Membership
138 ..... Meetings Calendar
140 ..... Seismic Soundoff

On the cover: A portion of Figure 12 from De Marco Centeno et al. (this issue) provides comparative FWI analysis of streamer (top) and ocean-bottom node inputs.

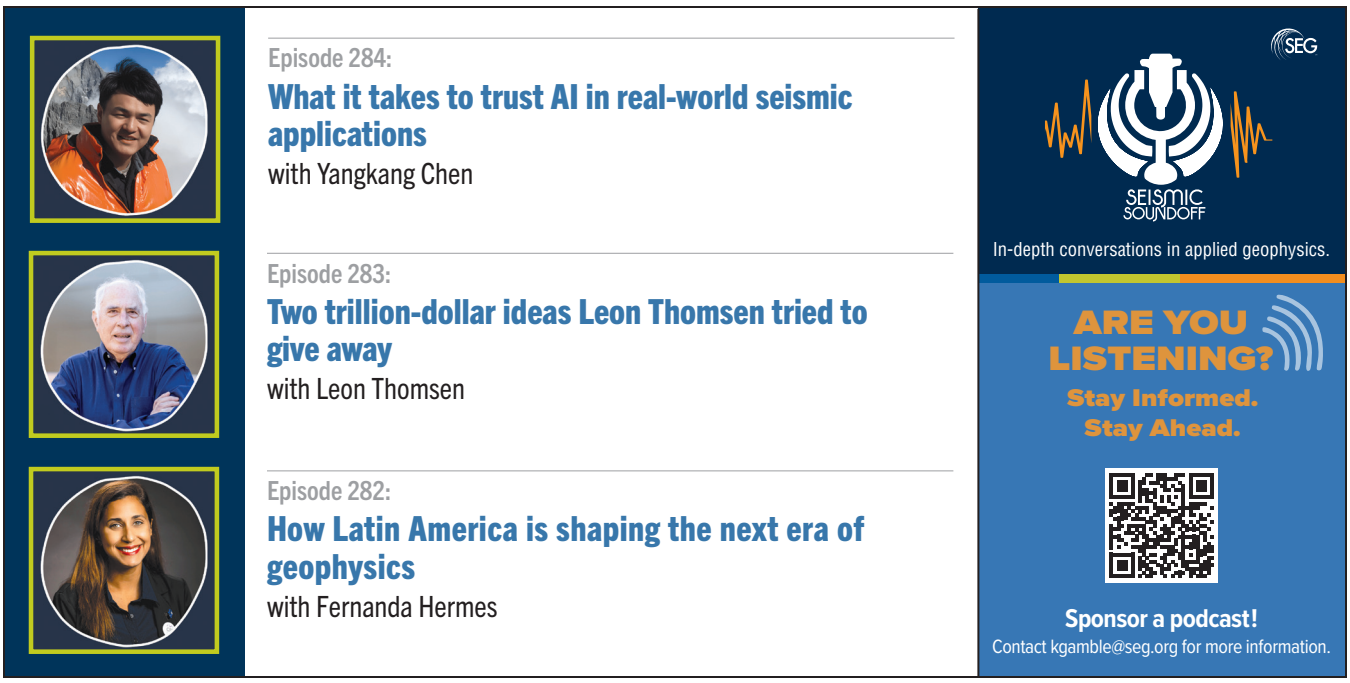

Downloaded from http://pubs.geoscienceworld.org/seg/tle/article-pdf/45/2/73/7765650/tle-v45-n2.pdf by Shivaji Maitra on 19 February 2026



Downloaded from http://pubs.geoscienceworld.org/seg/tle/article-pdf/45/2/77/7000000/tle45020077.1.pdf by Shivaji Maitra on 19 February 2026

SEG Board of Directors



PRESIDENT
Joseph Reilly
Industry, TX, USA



TREASURER

Mike Mellen
Houston, TX, USA



DIRECTOR AT LARGE

Joseph Ebeniro
University of Port Harcourt
Port Harcourt, Nigeria



PRESIDENT-ELECT
Rocky Detomo
Indialantic, Florida, USA



PAST PRESIDENT
John Eastwood
Calgary, AB, Canada



DIRECTOR AT LARGE

Lillian G. Flakes
Prospect Dimensions
Richardson, TX, USA



FIRST VICE PRESIDENT
Aria Abubakar
SLB
Houston, TX, USA



DIRECTOR AT LARGE
Aiman Bakhorji
Aramco Exploration
Dhahran, Kingdom of Saudi Arabia



CHAIR OF THE COUNCIL

Ge Jin
Colorado School of Mines
Golden, CO, USA



SECOND VICE PRESIDENT
Adriana Citlali Ramírez
TGS
London, United Kingdom



DIRECTOR AT LARGE
Sandeep Chandola
Petronas
Kuala Lumpur, Malaysia



VICE PRESIDENT, PUBLICATIONS

Alison Malcolm
Memorial University of Newfoundland
St. John's, NL, Canada



DIRECTOR AT LARGE
Patricia de Lugão
Strataimage
Rio De Janeiro, Brazil

The Leading Edge® (Print ISSN 1070-485X; Online ISSN 1938-3789) is published monthly by the Society of Exploration Geophysicists, 125 W. 15th St., Suite 100, Tulsa, Oklahoma 74119 USA; phone 1-918-497-5500. Periodicals postage paid at Tulsa, OK and at additional mailing offices.

Print subscriptions for professional members of the Society in good standing are included in membership dues paid at World Bank IV rates. Dues for Active and Associate Members for 2026 vary depending on the three-tiered dues structure based on World Bank classification of the member's country of citizenship or primary work residence. Students may purchase print subscriptions by paying a discounted fee during dues renewal or by contacting members@seg.org. Nonmembers may obtain online subscriptions by contacting books@seg.org. Copies of single issues of *The Leading Edge*® may be purchased by inquiry to books@seg.org.

Corporations, universities, and other institutions can purchase access to *The Leading Edge*® via standalone subscriptions or one of several available subscription package options. SEG's subscription pricing features three academic and three corporate tiers, providing affordable access to applied-geophysics content for institutions of any size. SEG subscription packages offer significant savings on the price of single-publication subscriptions. Special pricing is available for organizations with multiple sites and for institutional consortia. For more information on package pricing, including single-site and multisite institutional subscriptions, please contact subscriptions@seg.org. Institutional subscriptions for print delivery are available only with the purchase of a digital subscription. Rates are subject to change without notice. For more information, please visit https://seg.org/subscriptions.

Advertising rates for *The Leading Edge*® will be furnished upon request. No advertisement will be accepted for products or services that cannot be demonstrated to be based on accepted principles of the physical sciences. For more information, contact kgamble@seg.org.

Statements of fact and opinion are made on the responsibility of the authors and advertisers alone and do not imply an opinion on the part of the officers or members of SEG. Copyright 2026 by the Society of Exploration Geophysicists. *The Leading Edge*®, SEG®, and the SEG logo are registered marks of the Society of Exploration Geophysicists. All rights reserved. Material may not be reproduced without written permission. Printed in the USA.

JIM WHITE, Executive Director
SCOTT SUTHERLAND, Managing Director, Business and Geoscience Technology
JENNIFER COBB, Managing Director, Publications and Membership
STEVE BROWN, Director, Journals
MARIA GEE, Graphic Designer

Editorial information: 1-918-497-5503, sbrown@seg.org

Advertising information and rates:
1-918-497-5524
Kathy Gamble, kgamble@seg.org

Subscription information:
Members, members@seg.org
Nonmembers, books@seg.org
Institutions, subscriptions@seg.org

POSTMASTER: Send changes of address to
The Leading Edge
125 W. 15th St., Suite 100
Tulsa, OK 74119 USA

Downloaded from http://pubs.geoscienceworld.org/seg/tle/article-pdf/45/2/73/7765650/tle-v45-n2.pdf by Shivaji Maitra on 19 February 2026

THE LEADING EDGE

Editorial Calendar

Issue	Special section theme	Due date	Guest editors
All	Technical standalone articles	ongoing	*TLE* Editorial Board
March 2026	Advances in geophysics for groundwater applications	past due	Seogi Kang Michael Wilt[1]
April 2026	Geophysics for CCUS	past due	Michael Helgerud Manika Prasad Ramesh Neelamani[1]
May 2026	Quantitative interpretation	past due	Per Avseth Stephan Gelinsky Laurent Louis[1]
June 2026	Low-cost geophysics	past due	Erkan Ay Joël Le Calvez[1]
July 2026	Machine learning	15 Feb 2026	Haibin Di Stuart Farris Oleg Ovcharenko Qie Zhang Vladimir Kazei[1]
August 2026	Reservoir characterization	15 Mar 2026	Heather Bedle Satinder Chopra Karelia La Marca[1]
September 2026	Seabed geophysics	15 Apr 2026	William A. Burnett Evan S. Um G. Didem Beskardes[1]
October 2026	Applied mathematics for geophysics	15 May 2026	Matteo Ravasi Diancheng Wang Madhav Vyas[1]
November 2026	Near-surface geophysics/ geohazards	15 Jun 2026	Yudi Pan Shihao Yuan Dmitry Borisov[1]
December 2026	Multicomponent seismic	15 Jul 2026	Ramesh Neelamani[1]

[1]*TLE* Editorial Board coordinator

TLE publishes special sections and standalone articles covering all aspects of applied geophysics and related disciplines. Submission of articles is open to all. Please submit articles via the online manuscript submission system at **https://seg.kriyadocs.com/submissions/submit/seg/tle/login**. Submission instructions are available at **https://pubs.geoscienceworld.org/tle/pages/tle-ifa**. *TLE* Editorial Board coordinators work with guest editors to coordinate and support the review process and also may serve as guest editors. For additional assistance, contact **tle@seg.org.**

THE LEADING EDGE EDITORIAL BOARD



CHAIR
Vladimir Kazei
Aramco Americas
Houston, TX, USA
vladimir.kazei@aramcoamericas.com



Joël Le Calvez
SLB
Sugar Land, TX, USA
jcalvez2@slb.com



Madhav Vyas
BP America
Houston, TX, USA
madhav.vyas@bp.com



Laurent Louis
Aramco Americas
Houston, TX, USA
laurent.louis@aramcoamericas.com



Ramesh (Neelsh) Neelamani
ExxonMobil
Houston, TX, USA
ramesh.neelamani@exxonmobil.com



Michael Wilt
Lawrence Berkeley National Laboratory
Berkeley, CA, USA
mwilt@lbl.gov

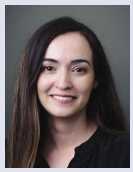

G. Didem Beskardes
Sandia National Laboratories
Albuquerque, NM, USA
gdbeska@sandia.gov

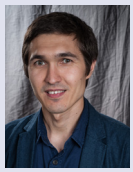

Dmitry Borisov
Kansas Geological Survey
Lawrence, KS, USA
dborisov@ku.edu



Karelia La Marca
BP America
Houston, TX, USA
karelia.la_marca@bp.com

Downloaded from http://pubs.geoscienceworld.org/seg/tle/article-pdf/45/2/73/7765650/tle-v45-n2.pdf by Shivaji Maitra on 19 February 2026

President's Page

Supporting the science and putting members first in 2026



This month's author:
Jim White, SEG Executive Director

It is hard to believe it is 2026 already. We have accomplished a lot during my short tenure at SEG, and we are extremely grateful for the efforts of staff, our volunteer leadership, as well as our engaged membership in helping to carry out our blueprint for success.

But, with a new year comes new resolutions. This next year marks another turning point, with anticipated changes that will guide our Society's continued evolution and improve how we serve our members. As Executive Director, I, along with my staff have been given clear directions from our Board of Directors to avoid complacency and forge ahead with new ideas, new initiatives that will ensure that our members recognize and appreciate the intrinsic value that a professional society like SEG can bring. So, I wanted to take the time to highlight our new and exciting platforms, programs, and global expansions that are currently ongoing by communicating how SEG is evolving for the betterment of our members.

As a professional society, access to all our efforts starts with our web page. A few years back, we started the process of upgrading our website by simplifying and providing clear navigation for learning, engagement, and leadership. Although we made headway, it was apparent that the site still needed improvement. So, our marketing department is hard at work refreshing the pages and creating a "member-first" design that we know will satisfy our organization. Roll-out for the new website is expected in early March.

Additionally, a reoccurring ask from membership has been a platform for tracking volunteer commitment. Not only did members want to follow their own efforts, but recognition for those efforts from their peers was also needed. As a result, our marketing department has engaged an outside firm, Higher Logic, to provide SEG and its members with a Digital Community Platform. With this software, SEG staff will now be able to track volunteer activity as well as allow for member connection, collaboration, and engagement. We are currently rolling out the new platform, so as a member, please do utilize it for your personal and professional benefit.

> "SEG is strong — our focus is clear and our key task at hand is to continue to provide value to our members."

There are other key initiatives underway within SEG. Global outreach continues to be a critical focus for our society's future growth. In a previous President's Page (*TLE*, November 2025), I noted that our organization's membership spans the globe. Our success in Latin America was noted, but there are other areas in the world that need commitment to those members that are located outside our core areas of activity. This includes countries and regions that currently lack adequate staff support to engage current and prospective members. To meet that demand, we have hired in-country staff in some of those other regions, such as India. The early results have been encouraging. There are more planned events (workshops, continuing education, etc.) as well as defined collaborative agreements with some of the local societies. India projects to have explosive growth in demand for energy in the near future, and we are not alone in identifying the need to staff professionals there for support. Outside of the state-run O&G companies that are active in-country, other U.S.-based supermajor organizations like ExxonMobil, Chevron, and BP have created key offices stacked with experienced geoscientists eager to assist India in their quest for energy independence. Our commitment to adding support will be widely accepted and appreciated.

SEG has historically been perceived as an applied geophysics society keying mostly on oil and gas. That inference is a bit unfair, as we have been committed to other areas of focus for applied geophysics, including near surface, environmental geophysics, as well as mining. But there is always room for improvement. Due to the increased demand for critical minerals, mining has recently taken center stage across the globe. Taking advantage of that increased awareness, our staff in the Middle East region recently launched our first critical minerals/mining symposium in Saudi Arabia late last year. Working with the kingdom, the Saudi Geological Survey, as well as other local and regional societies, SEG witnessed an overbooked and oversold event that sets the stage for how applied geophysics will be considered THE catalyst to meeting the demand to find those much-needed natural resources.

Downloaded from http://pubs.geoscienceworld.org/seg/tle/article-pdf/45/2/73/7765650/tle-v45-n2.pdf by Shivaji Maitra on 19 February 2026

Based on the incredible success of GEOMIN 2025, the Uzbekistan government entered into agreement with SEG to host GEOMIN 2026 later this year. The intent will be to rotate between the Middle East and Asia at large every other year (similar to our current co-hosted IPTC conference).

Conferences provide a platform for academic and business collaboration. But what about the proper preparation for the students to be able to fill the positions to execute the business plan, especially in areas like mining. The SEG EVOLVE program has experienced tremendous success in preparing students for O&G positions through our Reservoir Characterization syllabus. Based on that success, we are now developing an SEG EVOLVE Mining program to roll out for students. The experiential virtual platform allows SEG to reach students all over the world without the necessity of expensive travel. As such, we feel confident that through this program, the mining community will benefit greatly from a large and experienced early-career workforce to meet the demand. The challenge will be to find the key professionals with that type of experience to act as mentors to the students. To do that, we are currently engaging other professional societies that are more keenly focused on mining — our success with oil and gas should fit nicely in preparing us to shift that success to mineral exploration as well.

Late last month, on 22 January, I presented to many of our industry professionals at the Romancing Energy Forum here in Houston. The title of my talk was "SEG — Supporting the science. Connecting the stories," and it gave me the opportunity to talk about how the geosciences are evolving and how SEG's expanding role is playing a part.

To summarize my comments from that forum, and to close this column, I can say confidently that SEG is strong — our focus is clear and our key task at hand is to continue to provide value to our members. It is important for us to deliver that message every chance we get. TLE



22–27 Feb – Auckland, New Zealand
8th International Workshop on Rock Physics
Registration open

31 Mar–2 Apr – Kuala Lumpur
Offshore Technology Conference (OTC) Asia
Registration open

15–17 Apr – Bali, Indonesia
Asia Pacific Offshore Exploration Symposium (APEX): Unlocking the Depths of Asia Pacific Energy Frontiers
Registration opens soon

...and many more!

Current information as of 15 January. Please check seg.org/events for up-to-date information and more events.

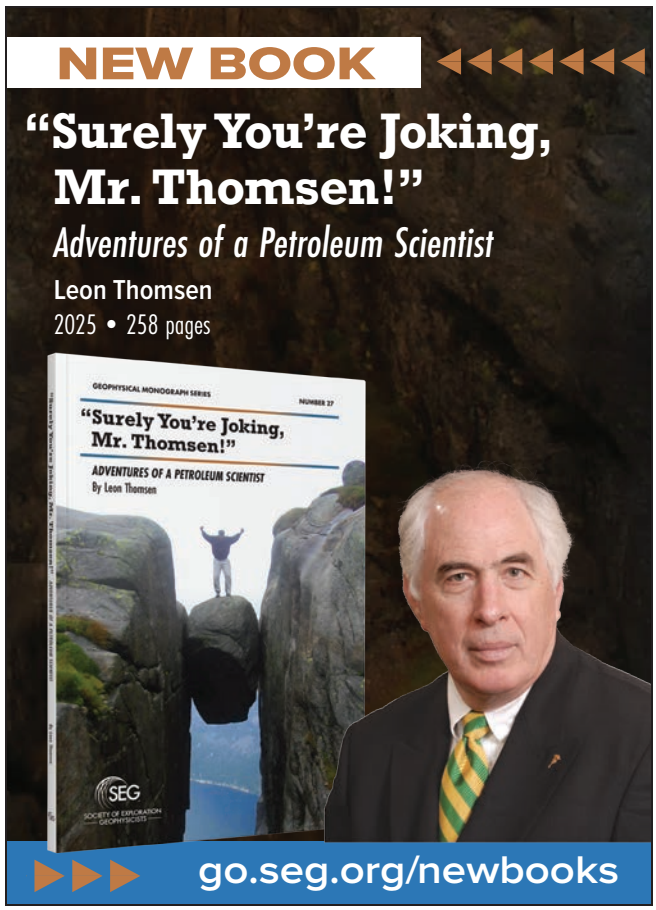

Downloaded from http://pubs.geoscienceworld.org/seg/tle/article-pdf/45/2/73/7765650/tle-v45-n2.pdf by Shivaji Maitra on 19 February 2026

Introduction to this special section: Advances in seismic acquisition

Ramesh Neelamani[1], Shivaji Maitra[2], Sandeep Kumar[3], and Faizan Akasyah Ghazali[3]

https://doi.org/10.1190/tle-4502-SS02

The field of seismic acquisition continues to evolve, driven by cutting-edge technological advancements, enhanced data analytics, and innovative field applications. New methodologies in seismic data collection, coupled with sophisticated computational tools, are enabling geophysicists to capture more accurate subsurface images and develop improved geologic understanding. These developments are pushing boundaries across a range of applications — from frontier and deepwater exploration to onshore resource identification and seismic hazard monitoring.

We are pleased to present this special section of *The Leading Edge*, showcasing four papers that highlight the latest trends and innovative approaches shaping the future of seismic acquisition. These contributions, selected for their technical depth and practical relevance, span a diverse range of geophysical challenges and solutions — from subsalt imaging in the Gulf of Mexico to advanced wavefield utilization in Southeast Asia. Together, they underscore the evolving landscape of exploration geophysics and the creative methodologies driving its future.

The first paper, "Advancing subsalt imaging in the U.S. Gulf: Operational and technical innovations in seismic data acquisition from the Laconia sparse OBN program" by De Marco Centeno et al., presents a large-scale, low-frequency ocean-bottom node (OBN) survey that integrates full-waveform inversion (FWI) and novel source technologies to improve imaging beneath complex salt structures. The success of this program demonstrates the scalability and effectiveness of multiclient OBN acquisition for basin-wide exploration.

In "Enhancing deep pre-carbonate imaging with DAS VSP mode-converted energy," Alai et al. investigate the use of mode-converted and multiple energy in distributed acoustic sensing (DAS) vertical seismic profiling (VSP). Conducted in a geologically complex Asia Pacific basin, the study demonstrates how unconventional wavefields can improve imaging beneath high-impedance carbonate layers.

The third paper, "Compressive sensing for seismic: From survey design to legacy data reconstruction" by Jiang et al., presents a multidimensional compressive sensing (CS) framework that optimizes acquisition geometry and enables efficient reprocessing of legacy data. By applying mutual coherence maps, the study connects theoretical CS principles with practical field implementation.

In "Unlocking the potential of blended acquisition with independent simultaneous sourcing and dispersed source array onshore Abu Dhabi," Ishiyama and Aljaberi describe a pioneering 3D pilot program that combines independent simultaneous sourcing and dispersed source array techniques. The results demonstrate tangible improvements in acquisition efficiency and cost-effectiveness without compromising data quality.

Together, these papers showcase the innovation and collaboration propelling seismic acquisition and exploration geophysics forward. We invite readers to explore the special section and discover the technologies and insights shaping the future of geophysics. TLE

[1]ExxonMobil, Houston, Texas, USA. E-mail: ramesh.neelamani@exxonmobil.com.
[2]Viridien, Kuala Lumpur, Malaysia. E-mail: shivaji.maitra@viridiengroup.com.
[3]Petronas, Kuala Lumpur, Malaysia. E-mail: sandeepkumar@petronas.com; faizan_akasyah@petronas.com.



Downloaded from http://pubs.geoscienceworld.org/seg/tle/article-pdf/45/2/73/7765650/tle-v45-n2.pdf by Shivaji Maitra on 19 February 2026

Advancing subsalt imaging in the US Gulf: Operational and technical innovations in seismic data acquisition from the Laconia sparse OBN program

Ricardo De Marco Centeno[1], Shuo Ji[1], Zhiping Yang[1], Richard Flower[1], Brad Wray[2], Huifeng Zhu[2], Shuki Ronen[3], and Paul Wentzler[3]

https://doi.org/10.1190/tle-2025-1013

Abstract

The Laconia program marks a major advancement in the design and execution of long-offset, low-frequency (LOLF) ocean-bottom node (OBN) seismic acquisition programs for subsalt imaging in the U.S. Gulf. With more than 18,000 km^2 of source coverage and more than 8000 node locations, this multiphase program builds on recent breakthroughs in full-waveform inversion (FWI) methodologies, sparse OBN geometry, and new source technology. A low-frequency-rich source — the Sercel Tuned Pulse Source (TPS) — was used to deliver LOLF OBN data with offsets greater than 50 km and ultra-low-frequency signal down to 1 Hz in the Garden Banks and northern Keathley Canyon. These LOLF OBN data enable the application of FWI to address long-standing challenges in salt velocity model building and in imaging the Wilcox Paleogene play beneath the notoriously complex salt structures in this region. The use of 150-day endurance nodes and a large node inventory enabled acquisition of ultra-long offsets consistently across the entire survey, demonstrating the scalability of multiclient OBN for basin-scale projects. Real-time telemetry of down-sampled hydrophone data enabled early FWI testing, allowing interpreters to gain insights on 5 Hz acoustic OBN FWI volumes three months before the fast-track delivery. Results from early-out FWI demonstrate substantial improvements in imaging the complex subsalt structures by resolving the velocity of overburden allochthonous salt and mobile shales. The program was executed with exceptional health, safety, and environment performance. The Laconia program sets a new benchmark for cost-effective, high-impact seismic acquisition and imaging at basin scale, delivering geophysical and geological value in structurally complex offshore environments, reducing structural and depth uncertainty beneath salt, and de-risking future drilling decisions.

Introduction

Seismic imaging in the deep water of the U.S. Gulf continues to demand innovative approaches due to the complexity of the geologic settings. In recent years, full-waveform inversion (FWI) has emerged as a powerful tool for velocity model building and subsalt imaging, resulting in step-change improvements in subsalt images never seen before (Shen et al., 2017, 2018; Zhang et al., 2018; Wang et al., 2019; Wu et al., 2022). It has become clear that FWI is most effective when long-offset, full-azimuth, and low-frequency data are available. Workflows based on wide- or full-azimuth towed-streamer data, even with the most advanced FWI algorithms, have reached performance limits, as streamer data lack the low-frequency signal-to-noise ratio (S/N) and the offset and azimuthal coverage needed to build accurate models and resolve complex structures such as highly deformed salt bodies and mobile shale formations (Lin et al., 2018; Ren et al., 2022).

Building on the proven value of sparse ocean-bottom node (OBN) geometries and recent advances in low-frequency seismic sources (Merritt et al., 2024), the Laconia program (see map in Figure 1) was designed to deliver a transformational uplift in model accuracy and structure clarity. With more than 18,000 km^2 of source coverage and more than 8000 node locations, Laconia integrates long-offset sparse OBN acquisition with a low-frequency-rich source (LFS) — an enhanced pneumatic source with high output at low frequencies below 2 Hz. This combination addresses long-standing constraints in FWI performance related to cycle skipping and limited diving wave illumination in subsalt zones (Figure 2).

Executed over a 9-month period with a five-vessel fleet, the Laconia phases I and II survey maintained on-schedule performance despite multiple weather interruptions, delivering stable source and data quality across all acquisition phases. The program was executed with exceptional health, safety, and environment (HSE) performance, recording more than 528,000 exposure hours with zero environmental incidents and a total recordable case frequency (TRCF) of 1.89 — demonstrating a strong commitment to protecting people and the environment. Quasi-real-time quality control (QC) of down-sampled hydrophone data, enabled via the data telemetry systems onboard, allowed for the validation of 1 Hz signal content and early FWI updates — setting the stage for accelerated interpretation workflows.

This article outlines the advances in survey design, acquisition configuration, operational execution, and

Manuscript received 29 July 2025; accepted 14 November 2025.

[1]Viridien (Earth Data), Houston, Texas, USA. E-mail: ricardo.demarcocenteno@viridiengroup.com; shuo.ji@viridiengroup.com; zhiping.yang@viridiengroup.com; richard.flower@viridiengroup.com.

[2]Viridien (Geoscience), Houston, Texas, USA. E-mail: brad.wray@viridiengroup.com; huifeng.zhu@viridiengroup.com.

[3]Viridien (Sensing & Monitoring), Houston, Texas, USA. E-mail: shuki.ronen@sercel.com; paul.wentzler@sercel.com.

Downloaded from http://pubs.geoscienceworld.org/seg/tle/article-pdf/45/2/73/7765650/tle-v45-n2.pdf by Shivaji Maitra on 19 February 2026

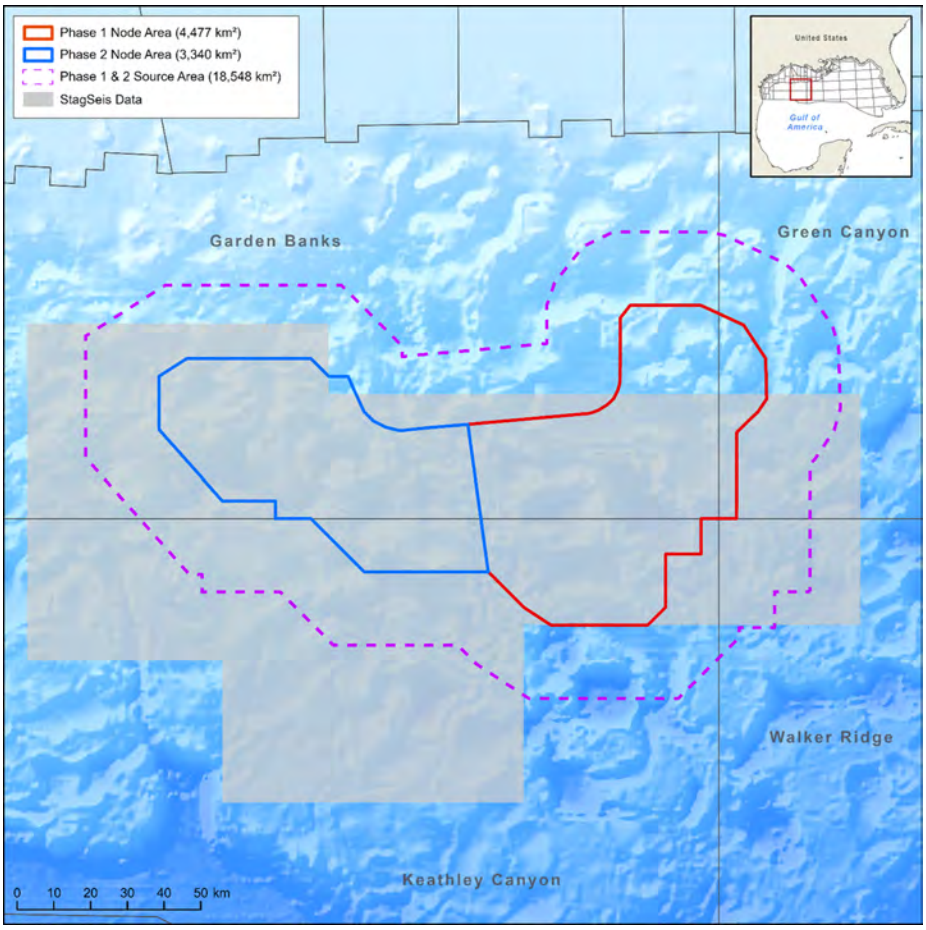

Figure 1. Location map of the Laconia phases I and II survey in the deepwater Gulf of America. The red polygon delineates the phase I node deployment area (4477 km^2), and the blue polygon outlines the phase II node area (3340 km^2). The dashed line represents the combined source area for both phases, including a 20-km shot halo, totaling 18,548 km^2. Gray boxes indicate the legacy full-azimuth towed-streamer (FATS) StagSeis data coverage across Garden Banks, Keathley Canyon, Walker Ridge, and Green Canyon.

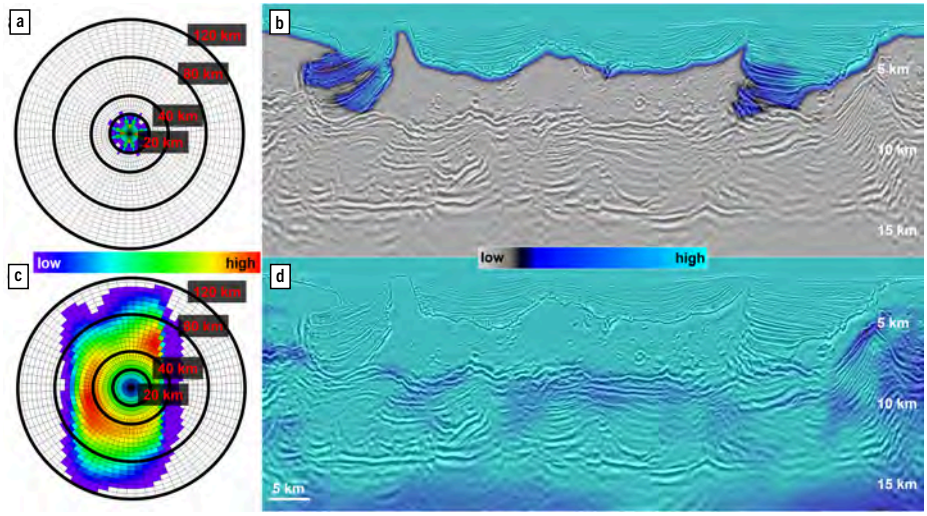

Figure 2. Top: Rose diagram and diving wave illumination from legacy FATS survey. (a) Acquisition fold and azimuth distribution showing the full-azimuth towed-streamer geometry. Although this geometry provided broad coverage, the long-offset content was constrained by limitations of the towed streamer spread. (b) Seismic volume overlay with diving wave illumination obtained using FATS data. Bottom: Rose diagram and diving wave illumination from the Laconia program. (c) Azimuthal fold coverage from Laconia sparse OBN survey, showing ultra-long offset coverage. (d) Overlay of diving wave illumination on the seismic volume highlights the uplift in subsalt illumination achieved with the Laconia survey.

geophysical outcomes of the Laconia program, with an emphasis on its ability to reveal deeper geological features through high-fidelity model building and imaging.

Geophysical rationale, survey design, and acquisition geometry

The Laconia program was designed to maximize the effectiveness of FWI in one of the most structurally complex regions of the U.S. Gulf. Building on synthetic studies by bp (Dellinger et al., 2017; Lin et al., 2021) and practical lessons from the Momentum project (Merritt et al., 2024), two geophysical parameters were identified as essential: (1) offset ranges exceeding 30 km to enable diving wave penetration of subsalt targets and (2) low-frequency content with high S/N down to 2 Hz, ideally 1 Hz, to drive robust FWI velocity updates.

Although effective in delivering high-frequency content suited for structural imaging, conventional air gun sources tend to offer limited S/N at ultra-low frequencies (<2 Hz), which can limit the effectiveness of FWI in the presence of large velocity errors. Enhancing low-frequency S/N is particularly beneficial for improving model convergence and interpretability in these challenging environments. In addition, streamer-based acquisition geometries are often restricted by narrow azimuths and limited long-offset content, which may result in insufficient diving wave illumination. Wide- or full-azimuth towed-streamer (WATS or FATS) surveys improve azimuth and offset coverage relative to conventional streamer designs, but even the best full-azimuth streamer solutions still fall short of what can be achieved with OBN acquisitions. To address these challenges, Laconia adopted a sparse OBN geometry acquiring ultra-long offset data (exceeding 50 km) using a new purpose-built low-frequency pneumatic source. A few such low-frequency sources have become available commercially in recent

Downloaded from http://pubs.geoscienceworld.org/seg/tle/article-pdf/45/2/73/7765650/tle-v45-n2.pdf by Shivaji Maitra on 19 February 2026

years (Ronen and Chelminski, 2017; Chelminski et al., 2021; Rentsch et al., 2022; Udengaard et al., 2024). The TPS, designed by Viridien's Sensing & Monitoring business, was chosen for Laconia.

It is a completely new design engineered to operate at lower pressures and emit larger volumes of air with a long rise time and dominant bubble oscillations. Figure 3 shows that the new data deliver signal down to 1 Hz.

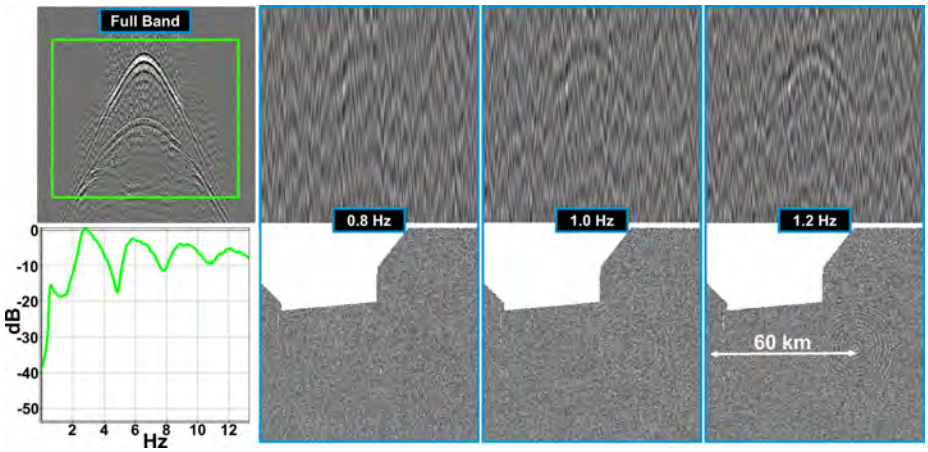

Figure 3. Raw data QC from the Laconia survey. Top row: Common receiver gather showing the full-band signal (left) and corresponding bandpass filters isolating low frequencies below 0.8, 1, and 1.2 Hz high cuts. Coherent diving wave energy is visible down to 1 Hz, demonstrating the effectiveness of the LFS in generating ultra-low-frequency content. The blending noise from the adjacent source unit (deployed from the same vessel with 200 m crossline separation) is observable on the upper left, a result of this dual-source wide-tow configuration. Bottom row: Average amplitude spectrum of the data on the left shows a bubble oscillating at a resonance frequency of 2.7 Hz. Frequency slice "phase rings" at 0.8–1.2 Hz validate the presence of coherent signal across the critical 1–1.2 Hz range.

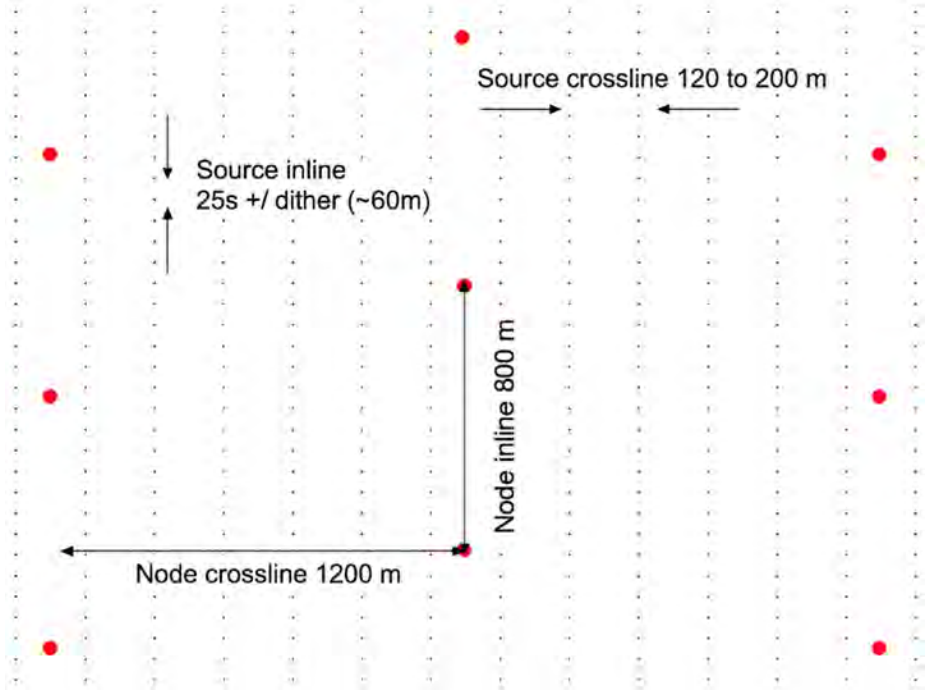

Figure 4. Preplot layout for nodes and sources in the Laconia I and II survey. Node spacing was 800 m inline by 1200 m crossline, yielding a receiver density of 1 node per square kilometer. Dual sources were fired every 60 m inline and every 200 m crossline, with a randomized dither of ±1.5 s applied to a 25 s shot interval — resulting in a shot density of approximately 83 shots per square kilometer. The diagram shows inline stagger of 400 m between node lines and a wide-tow source configuration with 120–200 m crossline separation.

By fulfilling both geophysical criteria — low-frequency richness and long-offset illumination — the survey design enabled FWI to resolve complex deep velocity anomalies that have eluded previous imaging efforts on legacy streamer surveys.

The Laconia I and II survey implemented a staggered node layout covering approximately 336 Outer Continental Shelf (OCS) blocks (approximately 8000 km^2) with a nominal inline spacing of 800 m and crossline spacing of 1200 m. This node geometry matched the Momentum survey layout, whereas the Laconia survey introduced further enhancements in source configuration. The Momentum survey used an array configuration with two LFS units towed in close proximity (20 m apart) and fired simultaneously. Thanks to execution experience gained on the Momentum survey and the newly enhanced source deployment technology, Laconia increased the crossline separation between these two LFS units to 120–200 m (Figure 4) and fired them in single point source mode with independent dithering between firings (Elboth and Vinje, 2019). This staggered firing increased shot density without raising the total emitted energy, effectively doubling shot line coverage per sail line (Ji et al., 2025).

The source grid was acquired using 400 m sail line spacing with flip-flip shooting on time with ±1.5 s dithering between shots. This created an extensive shot footprint with over 1.5 million shots and a 20 km effective shot halo. This design extended the source coverage to approximately 800 OCS blocks, enabling data capture at ultra-long offsets beyond 50 km (Ji et al., 2025).

The acquisition geometry was tailored to satisfy offset constraints such that the diving wave could penetrate deep through key subsalt formations. Simulation results and early FWI test results confirmed the effectiveness of this design, showing improved energy propagation through allochthonous salt and mobile shale — geobodies known to impede imaging in legacy streamer-based surveys (Merritt et al., 2024; Jonke et al., 2024).

Downloaded from http://pubs.geoscienceworld.org/seg/tle/article-pdf/45/2/73/7765650/tle-v45-n2.pdf by Shivaji Maitra on 19 February 2026

Figure 5a and 5b demonstrates the consistent azimuthal coverage and a balanced offset distribution achieved, setting the foundation for subsequent FWI and imaging workflows.

Breakthroughs in seismic source technology

The Sercel TPS LFS was a cornerstone of the Laconia program's low-frequency acquisition strategy. To meet the project's geophysical goals — including ultra-long offset coverage and enhanced FWI performance — TPS units with 28,000 in^3 chambers were deployed as single-point sources. This configuration targeted the 1–2 Hz band, where conventional air guns are weakest, enabling better resolution of large-scale velocity errors often associated with complex salt structures.

The TPS design includes a large cylindrical air chamber with approximately 360° radial ports and a smooth release mechanism engineered to reduce high-frequency energy and avoid cavitation-producing water jets. This architecture supported Laconia's FWI objectives by improving low-frequency signal quality and minimizing environmental impact (Ronen and Chelminski, 2017). For the Laconia program, the dual LFS system was configured with asynchronous dithers and 120–200 m crossline separation, improving crossline sampling without increasing the emitted energy per unit area.

The LFS was tested with chambers ranging from 600 to 28,000 in^3. Figure 6 shows the relationship between bubble frequency and chamber volume across pneumatic sources. The bubble period T is proportional to the cubic root of volume V times pressure P:

$$T \propto \sqrt[3]{VP}. \quad (1)$$

Despite operating at only half the pressure of conventional air guns, the much larger volume of the LFS enables significantly longer bubble periods, producing useful signal down to approximately 1 Hz — critical for low-frequency FWI.

At its resonance frequency of 2.7 Hz, the 28,000 in^3 LFS configuration used in Laconia produced signal levels approximately 28 dB higher than a typical air gun array (Figure 7). The discontinuity in the slope between the air guns and the LFS is due to the pressure difference between the systems. Because the bubble period is proportional to the cubic root of the pressure multiplied by the volume, the relation between the volume and the bubble frequency is linear on this log-log plot. Although its high-frequency output is lower, Shang et al. (2023) demonstrates that effective processing of near-field hydrophone data can recover signal up to 60 Hz.

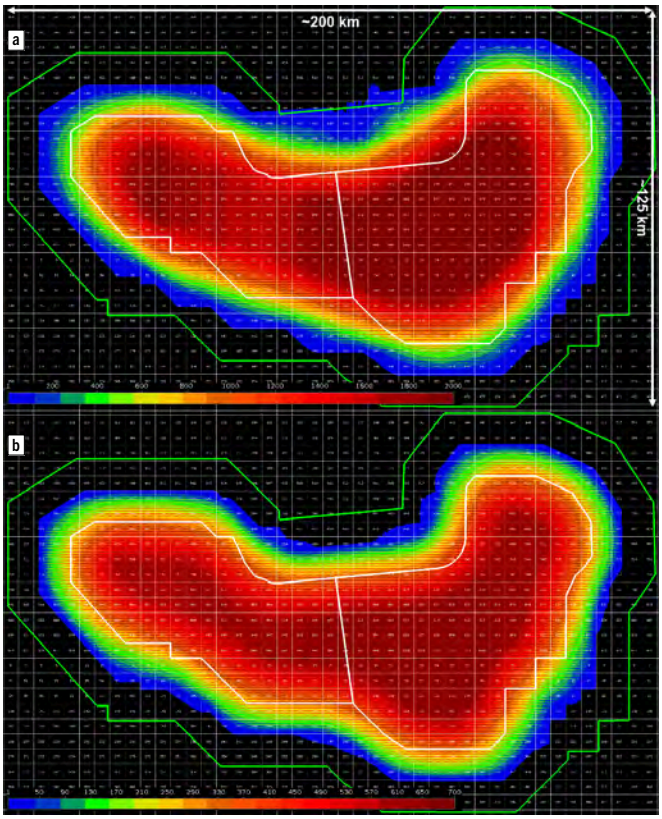

Figure 5. Offset fold maps for the combined Laconia phases I and II node areas, computed on a 100 m × 30 m CDP grid. (a) The full-offset fold distribution reflects uniform coverage across the 800 m × 1200 m sparse OBN layout, supported by consistent long-offset shooting. (b) This view isolates the contribution of near- and mid-offset (<30 km) data to the fold, illustrating dense and consistent coverage throughout the central node patch. The background is an OCS block map.

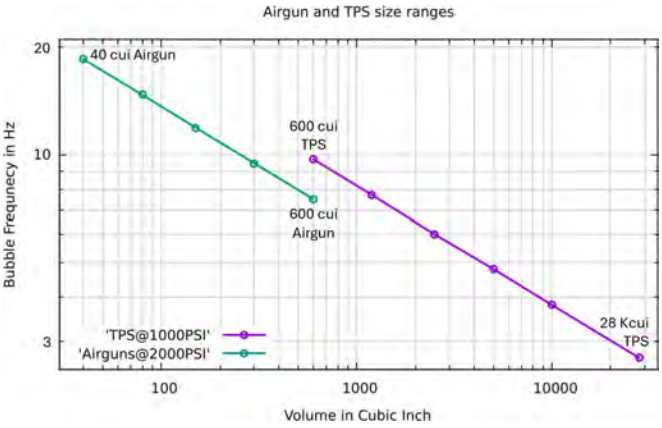

Figure 6. Bubble frequency versus chamber volume for air guns and LFS systems. Air guns (green) operate at 2000 PSI and range from 40 to 600 in^3, whereas LFS (purple) operates at 1000 PSI with volumes tested up to 28,000 in^3. The circles denote examples of chambers at various volumes. The smallest volume tested is 600 in^3. The largest volume tested is 28,000 in^3. LFS achieves significantly lower bubble frequencies, producing useful signal down to near 1 Hz.

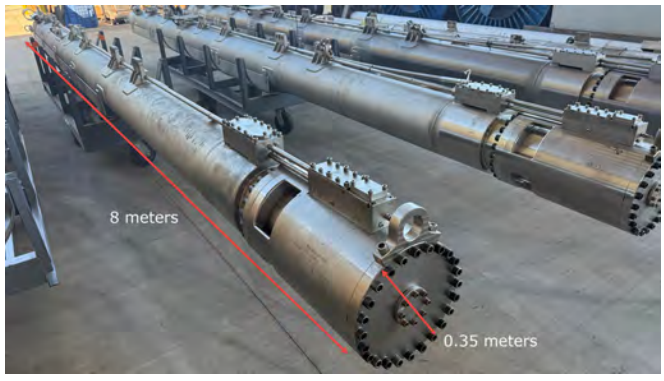

Figure 7. TPS on the assembly line. The full unit is approximately 8 m long. The head on the right is mounted on a 28,000 in^3 firing chamber — as used in the Laconia survey. One of four radial ports is visible. Two additional heads can be seen stored beneath the workbench in the background.

Downloaded from http://pubs.geoscienceworld.org/seg/tle/article-pdf/45/2/73/7765650/tle-v45-n2.pdf by Shivaji Maitra on 19 February 2026

Without the need for complex source arrays, the LFS enhanced operational efficiency through simplified deployment logistics and reduced shot-to-shot variability. The LFS was used as a single-point source (Figure 8). Compared to conventional arrays where the signature is azimuth and dip angle-dependent, single-point sources produce perfectly isotropic radiation. They are not subject to intra-array geometry variations from shot to shot and therefore have more stable signatures. Its lower sound pressure level (SPL) — approximately 8 bar-m, or 12 times lower than a typical air gun array — helped avoid receiver saturation, also known as max-level overdrive, and improved the dynamic range between weak diving waves at far offsets and strong direct arrivals in the near offsets. Additionally, the longer rise time reduced the SPL slope to approximately 1 bar-m/ms, compared to 3 bar-m/ms for a single air gun and up to 90 bar-m/ms for a 30-gun array. Because pressure slope is proportional to particle acceleration, a lower slope implies reduced potential for environmental disturbance.

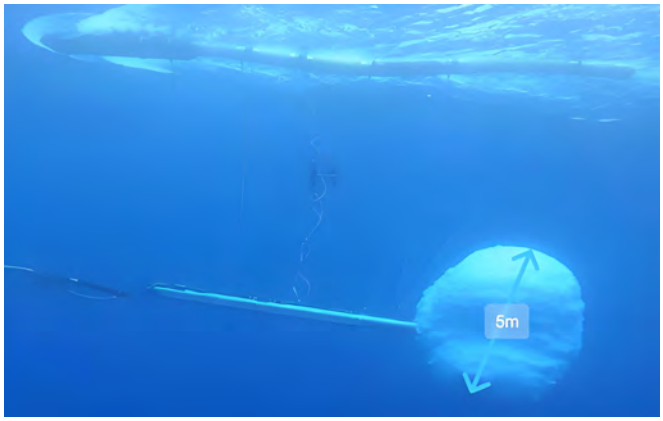

Figure 8. Underwater view of the LFS during firing. Unlike conventional air guns deployed in arrays, the LFS functions as a single-point source, generating a large oscillating bubble with a radius of more than 2 m and a period of almost 400 ms. The point-source design offers operational benefits such as faster deployment and recovery, lower technical downtime, and enhanced geophysical performance, including reduced risk of receiver overdrive, consistent shot-to-shot signature, improved shot positioning, and a more isotropic radiation pattern.

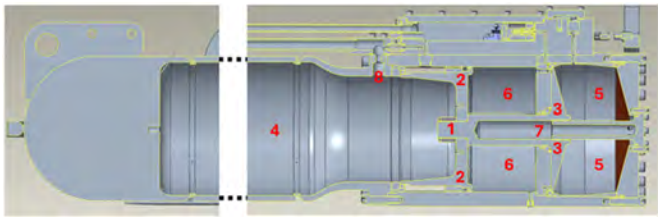

Figure 9. Schematic cross-section of the TPS. The shuttle assembly (1) consists of a shaft and two pistons: a firing piston (2) and an operating piston (3). This source contains four air-filled chambers: the large firing chamber (4), the operating chamber (5), the mid chamber (6), and the shaft chamber (7), which collectively control piston motion and prevent ballistic behavior. The use of air in all chambers avoids cavitation — a common issue in water-filled air guns. Air is supplied and drained via an orifice (8) located outside the shaft, preventing unintentional auto-fires and enhancing crew safety.

Environmental and safety performance were further supported by specific design features of the LFS (Figure 9). Its air-filled mid-chamber and zero-acceleration firing flange eliminate water jet cavitation common in conventional air guns. Air guns, originally designed to emulate explosive sources, rely on an acceleration distance and water-filled mid-chambers. The acceleration distance causes quicker opening of the ports, providing the shorter rise time that was requested by customers who had been using explosive sources. The water in the mid chamber is discharged at high velocity and generates high-frequency noise. By contrast, the TPS has zero acceleration distance, and its air-filled mid chamber avoids cavitation, reducing unnecessary environmental impact. A safety feature of the TPS is that the firing chamber is filled and emptied directly from the umbilical, rather than through the operating chamber — eliminating the risk of auto-firing and improving crew safety.

To meet Laconia's acquisition parameters — including rapid shot cycling, reliable pressure control, and integration with standard umbilicals — an in-sea pressure regulator system (PRS) was developed and deployed, mounted between the umbilical and the source. This in-sea unit regulates pressure from the vessel's manifold and ensures consistent chamber recharge rates regardless of umbilical configuration.

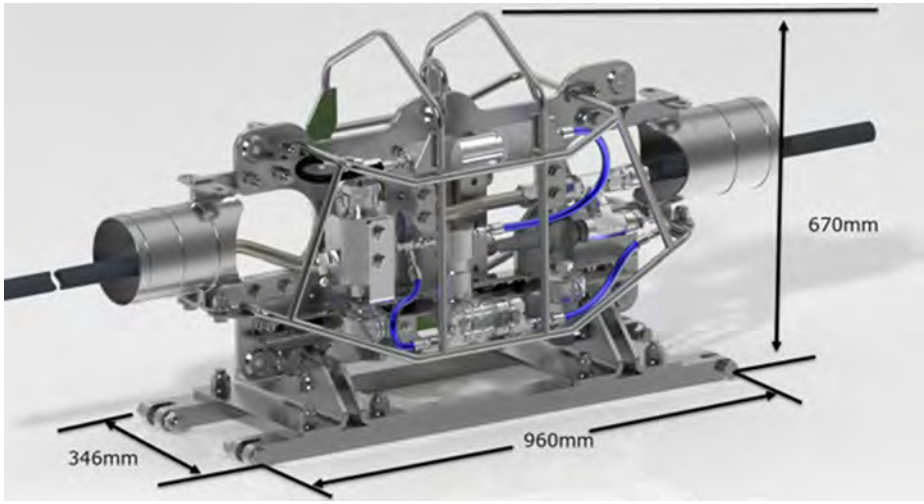

Figure 10. Rendered image of the PRS. The system is responsible for modulating the firing and recharge pressure of the firing chambers. It features high-precision pneumatic control components with reinforced stainless-steel framing for structural integrity. Note the blue high-pressure lines for controlling air routing and the compact configuration designed for integration within vessel deck layouts.

Figure 10 shows the PRS, and Figure 11 illustrates its impact on refill time. Pressure on the umbilical dry side ranged from 1060 to 1800 PSI, depending on compressor settings. A downstream pressure sensor measured pressure recovery after shots fired at 0 and 25 s. The LFS was ready to fire again when pressure reached 1000 PSI, which occurred in approximately 25 s at 1060 PSI and in approximately half that time at 1800 PSI. This demonstrated the scalability of LFS shot rates with available pressure and

Downloaded from http://pubs.geoscienceworld.org/seg/tle/article-pdf/45/2/73/7765650/tle-v45-n2.pdf by Shivaji Maitra on 19 February 2026

confirmed PRS effectiveness in maintaining consistent source performance during high-duty-cycle acquisition.

Operational efficiency, cost, and scalability strategies

Executing the Laconia program required careful orchestration of technology, logistics, and vessel coordination to meet ambitious data quality and turnaround goals in a challenging offshore environment. Despite multiple significant weather disruptions over a 9-month period, the survey was completed on schedule with no lost-time HSE-related incidents, underscoring the strength of the operational planning and execution framework.

The campaign mobilized five vessels: two source vessels equipped with dual LFS, two node-handling vessels for deployment and retrieval, and one support vessel. More than 200 offshore personnel were deployed in round-the-clock operations, spanning a node footprint of approximately 336 OCS blocks (approximately 8000 km^2). These operations delivered a receiver carpet of more than 8000 node locations and more than 1.5 million source shots, extending shot coverage to nearly 800 OCS blocks (approximately 18,000 km^2) including a minimum 20 km shot halo (Ji et al., 2025).

One of the most compelling outcomes of the Laconia program was its demonstration that high-end subsalt imaging using sparse OBN geometry and low-frequency sources can be achieved at scale without a prohibitive cost. The survey design leveraged lessons from previous programs to maximize efficiency across three critical dimensions: shot coverage, node density, and acquisition duration.

Sparse geometry with purposeful illumination. The use of sparse OBN geometry — 800 × 1200 m node spacing — was a deliberate cost-control strategy. By optimizing placement to achieve sufficient fold and offset coverage for FWI, the project reduced node count while still satisfying model-building requirements. Strategic staggering of node lines optimized spatial sampling without increasing the receiver count (Lin et al., 2018).

Similarly, the source configuration, although unconventional, contributed to cost efficiency. The dual-source arrangement with 120–200 m crossline separation and independent dithering allowed for denser source XL sampling while maintaining the same vessel count and fuel budget as a conventional dual-source setup. The extended 20 km shot halo and approximately 46,000 km of total shot lines maximized the value of each sail line.

Effective node deployment/retrieval management. The use of long-endurance deepwater nodes with battery life exceeding 150 days allowed extended deployment cycles and reduced handling frequency. Combined with a large node inventory, this enabled the expansion of XL offset from 30 to about 40 km. The consistent receiver footprint and strategic planning underscored the scalability and economy of large multiclient OBN programs. This approach ensured efficient asset utilization and helped demonstrate that operational reliability and geophysical quality can coexist in large-scale surveys.

Source reliability and compatibility. Initially, the operation was constrained by refill time dependency on a specific umbilical diameter to regulate air pressure delivery, limiting the umbilical length and the separation between the port and starboard sources to 120–140 m with a 400 m sail line interval. The PRS was developed during the surveys and enabled longer umbilicals and the operational flexibility of physical crossline interval separation between sources deployed from the same vessel — an important factor in minimizing acquisition footprint overlap to a uniform 200 m crossline interval. The development and integration of a dedicated pressure regulator module enables LFS deployment across the industry. This enhancement allows the LFS to function effectively with any conventional source acquisition system, eliminating the need for custom rigging or infrastructure modifications.

From a source reliability perspective, the performance of LFS exceeded expectations. Despite its novelty compared to conventional air guns, and thanks to lessons learned and improvements made after the Momentum survey, source technical downtime for Laconia was kept below 4%, on par with mature systems. This success reflects the robustness of the TPS design, as well as strong collaboration between

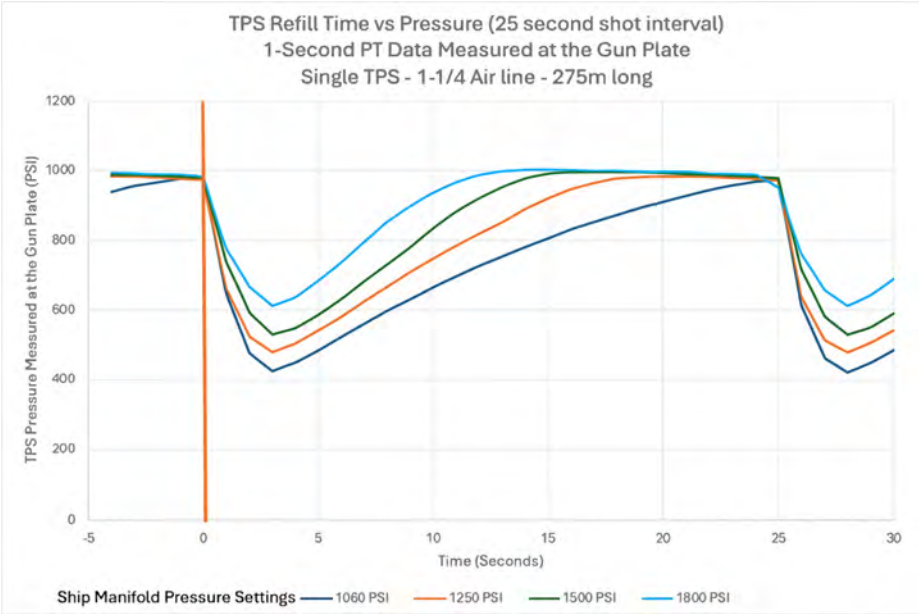

Figure 11. Refill time versus vessel manifold pressure. Pressure was measured at the gun plate (downstream of the PRS) at 1 s intervals following source activation at 0 and 25 s. At the moment the shot is fired, pressure at the firing chamber drops sharply (not shown), triggering recharge from the umbilical. Refill rates depend on the manifold pressure: at 1060 PSI, the LFS returns to 1000 PSI readiness in approximately 25 s; at 1800 PSI, the system recharges in approximately half the time. These results demonstrate refill rate scalability with available pressure, influencing maximum achievable shot rate.

Downloaded from http://pubs.geoscienceworld.org/seg/tle/article-pdf/45/2/73/7765650/tle-v45-n2.pdf by Shivaji Maitra on 19 February 2026

acquisition and technical support teams. The high uptime ensured consistent signal quality and energy output, critical for maintaining the integrity of a seismic dataset built to maximize low-frequency energy for FWI.

Real-time processing and turnaround acceleration. A critical enabler of efficiency and early imaging was the integration of quasi-real-time data telemetry. Upon each node retrieval, hydrophone data were downsampled to 16 ms and streamed to shore via the on-board telemetry capabilities. This meant that the processing team could conduct quality control and FWI tests while the acquisition was still underway. The survey started in mid-2024, and retrieval of the first 2000 nodes ready for FWI testing was completed by December 2024. By early January 2025, a test dataset of approximately 2000 nodes was already being processed, and by late February — just 40 days after the retrieval of the final node from phase I — the team delivered a full-area 5 Hz acoustic full-waveform inversion (AFWI) model and image volume.

The seamless handoff between offshore acquisition, real-time telemetry, and early imaging workflows created a highly compressed feedback loop. Interpreters were able to assess geologic features in the 5 Hz AFWI model well in advance of the fast-track volume release, gaining valuable lead time for prospect evaluation. This operational synergy across vessels, data systems, and teams reflects a maturing model for efficient, high-impact seismic programs in deepwater exploration (Ji et al., 2025).

Operational partners and technical support. Operational support teams contributed to the operational efficiency and technical robustness of the Laconia OBN campaign through a dedicated onboard presence focused on acquisition optimization and quality control. Positioned on the Sanco Sword vessel, acquisition optimization specialists served as a bridge between Viridien and the acquisition contractor, facilitating real-time communication, situational awareness, and execution alignment. The team supported acquisition with reshoot planning, transit times monitoring, and providing continuous time and motion analysis. High-resolution positional QC was performed — validating 99.8% node placement within 5 m of preplot targets — and supported compliance with survey specifications through navigation attribute validation. Weekly reporting, web-based Marlin dashboards, and productivity tracking tools aided operational visibility and decision-making. These contributions added value in managing geophysical risk and maintaining technical integrity throughout this complex deepwater acquisition program, contributing to overall project efficiency and delivery.

Modular and replicable framework. Ultimately, the success of Laconia underscores how sparse OBN acquisition with a low-frequency emphasis is scalable and replicable in other basins — especially where complex overburden precludes reliable imaging with streamer-only geometries. The modular nature of LFS deployment and sparse node layout allows adaptation to basin size, risk profile, and investment thresholds.

Geophysical and geological results

The early-out imaging results from Laconia phase I confirmed the transformative impact of combining long-offset sparse OBN with LFS-driven low-frequency content and FWI. FWI updates derived from the initial 2000-node test set had already delivered significant uplifts in velocity model accuracy and structural clarity compared to previous streamer-based solutions.

Comparative FWI analysis between streamer and OBN inputs revealed stark contrasts (see Figure 12). Although streamer FWI appeared to improve subsalt reflector continuity at some locations, its updates below the diving wave penetration depth were very limited. The Laconia OBN FWI, by contrast, produced proper updates aligned with geologic expectations, leading to more accurate and interpretable structural outcomes thanks to its high S/N ratio at low frequency and long-offset coverage.

The mobile shales imaged in the Laconia OBN volume emerged as critical geologic features. Although their presence had been inferred from regional geology, their geometry and seismic expression remained elusive in legacy datasets. The Laconia dataset provided the first clear and consistent images of these bodies, revealing their sharp velocity contrasts relative to surrounding sediments. These features play a similar geophysical role to salt: distorting wavefields and complicating inversion unless properly resolved. Laconia imaging revealed these bodies with great detail, improving risk assessment for exploration wells near these features. The Mesozoic section and deeper basement structure became apparent on the OBN AFWI model and OBN AFWI Image. Large sections of deep salt missing from the

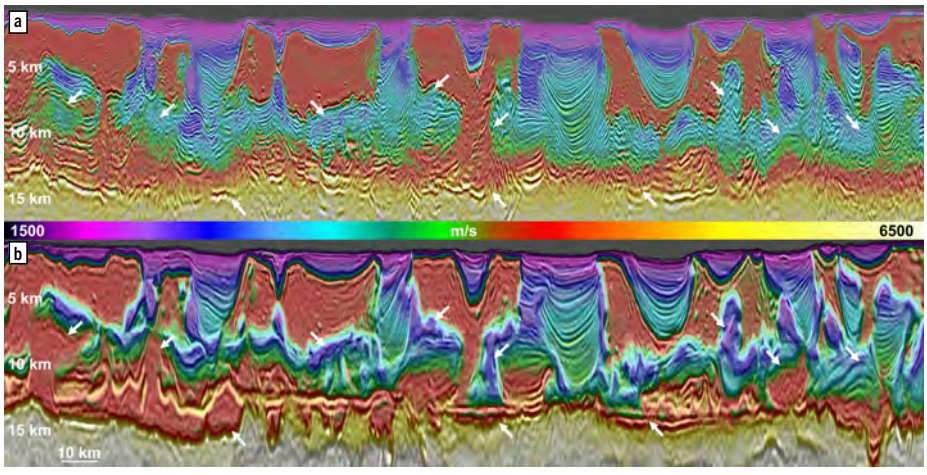

Figure 12. (a) 15 Hz streamer RTM and 6 Hz streamer AFWI model overlaid (b) 5 Hz OBN FWI Image with 5 Hz OBN AFWI model overlaid. The LOLF OBN AFWI completely redefines the subsalt velocities. Extensive slow-velocity zones are detected. The Mesozoic section is clearly delineated, and the complexity at the basement level becomes visible. Arrows mark zones of slow-velocity mobile shales, improved basement reflectivity, large-scale changes to the Mesozoic, and detection of deep salt missing in the streamer AFWI model.

Downloaded from http://pubs.geoscienceworld.org/seg/tle/article-pdf/45/2/73/7765650/tle-v45-n2.pdf by Shivaji Maitra on 19 February 2026

streamer FWI were detected and updated by the OBN AFWI. The LOLF OBN AFWI update already provides a step change in image quality compared to what could be achieved with streamer data.

Additionally, OBN-enabled FWI enhanced the delineation of the highly rugose base-of-salt surface and deeper reflectors within the Wilcox play. These improvements are pivotal for drilling decisions, as the interplay between salt geometries, mobile shale deformation, and potential reservoirs directly impacts prospectivity and well planning.

Together, the Laconia results suggest that the combination of sparse OBN and low-frequency source is not only a technological milestone — it is a practical toolset for unlocking complex geologic provinces with meaningful operational efficiency.

Seismic wave propagation within the earth is elastic by nature. The acoustic assumption in AFWI breaks down at places where large impedance contrasts induce strong elastic effects. Unexplained elastic energies not only blur the sharp velocity boundaries in the AFWI model, they also manifest themselves as noise, which reduces the S/N of the AFWI velocity model. Incorporating elastic propagation into the FWI engine allows modeled data to better match real data in terms of phase and amplitude. For Laconia, a 5 Hz elastic FWI (EFWI) update was carried out using the LOLF OBN data starting from the 5 Hz LOLF OBN AFWI velocity model. Figure 13a and 13c show a reduction in the salt halo at TOS and BOS on the EFWI model. Including elastic effects in FWI allows for better explanation of the data, leading to improved convergence and fewer artifacts. This results in sharper formation interfaces, better event continuity, and higher S/N on the EFWI Image than its acoustic counterpart (Figure 13b and 13d). Anisotropy parameters were updated based upon well information. The subsequent 5 Hz LOLF OBN EFWI update reduced misties of major salt boundaries and key subsalt events to approximately 1% or less on average.

The 5 Hz LOLF OBN EFWI provides another step-change improvement over AFWI. However, to move beyond large-scale structural interpretation, higher resolution is needed. With the kinematics resolved by the 5 Hz LOLF OBN EFWI update, underlying FATS streamer data, with its denser spatial sampling, is incorporated into the inversion for higher-frequency updates. The 12 Hz OBN + streamer EFWI update shows increased resolution top down on the model and FWI Image. The salt halo is also further reduced with the increase in frequency. The improvement in subsalt resolution is obvious with small-scale features and sedimentary layers becoming visible on the 12 Hz EFWI Image. This increase in resolution is critical for understanding detailed structure at the reservoir level. The 12 Hz OBN + streamer EFWI model and EFWI Image (Figure 14c and 14d) can be compared against what can be achieved with streamer data (Figure 14e and 14f). The 12 Hz EFWI Image offers similar or better resolution to the 15 Hz streamer RTM with far superior illumination and S/N.

Discussion

The Laconia program sets a new benchmark for scalable seismic acquisition in geologically complex deepwater environments. It demonstrated that sparse OBN acquisition — when paired with low-frequency source technology and EFWI — can deliver transformative subsalt imaging.

Geophysically, the program validated that a purpose-driven acquisition design — featuring ultra-long offsets, low-frequency signals down to 1 Hz, and full azimuthal coverage — leads to more accurate velocity models and structurally consistent images. Geobodies that historically impeded imaging, including mobile shales and complex salt geometries, were resolved with greater clarity. These improvements directly benefit interpretation in the Wilcox Paleogene and Mesozoic plays by enabling deeper structural understanding and reducing geologic uncertainty.

Operationally, the program showed that the low-frequency sources that we used are reliable — with less than 4% downtime — and compatible with conventional acquisition systems, thanks to the introduction of a pressure regulator system near the source. This enabled source separation beyond 200 m on a single vessel, improving design flexibility and field efficiency. The campaign also logged more than 528,000 exposure hours without environmental incidents and maintained a TRCF of 1.89, underscoring its HSE performance.

The integration of 150-day battery life nodes and low-latency telemetry enabled consistent ultra-long offset coverage and accelerated time to imaging, with a 5 Hz AFWI model delivered just 40 days after acquisition. The long-endurance node inventory minimized

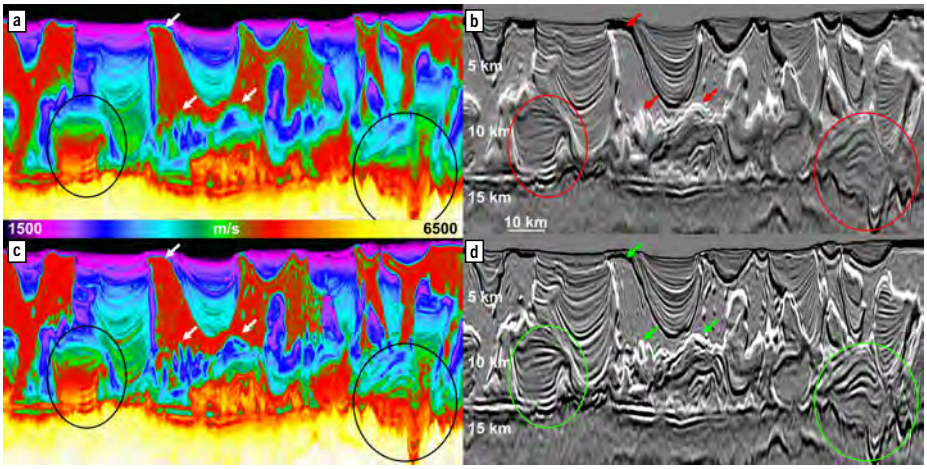

Figure 13. Comparison of FWI velocity models and FWI images from AFWI and EFWI for the Laconia survey. (a) AFWI velocity model and (b) corresponding AFWI Image. (c) EFWI velocity model and (d) corresponding EFWI image. The EFWI update refined salt boundaries and improved velocity definition in subsalt overpressure zones, resulting in enhanced clarity and continuity compared to AFWI. Arrows indicate areas of sharpened salt boundaries. Circles mark zones of improvement in resolution and S/N on the EFWI model and EFWI Image.

Downloaded from http://pubs.geoscienceworld.org/seg/tle/article-pdf/45/2/73/7765650/tle-v45-n2.pdf by Shivaji Maitra on 19 February 2026

redeployments and enhanced crossline offset coverage — supporting the scalability of multi-client programs.

Strategically, Laconia offers a modular and replicable model for future frontier exploration, particularly in basins where streamer-based surveys are limited by overburden complexity or illumination gaps.

The sparse OBN geometry and dual-source wide-tow configuration optimized vessel time and coverage efficiency, delivering basin-scale illumination without a proportional cost increase.

The combined AFWI-EFWI workflow reduced structural and depth uncertainty beneath the salt canopy by improving low-frequency constraints and elastic consistency along complex interfaces. By combining the sparse LOLF OBN data with the underlying streamer data, a higher resolution EFWI model and EFWI Image can be generated.

These improvements directly de-risk future drilling by clarifying trap geometries, fluid-sensitive intervals, and velocity hazards in the Wilcox and deeper Mesozoic sections.

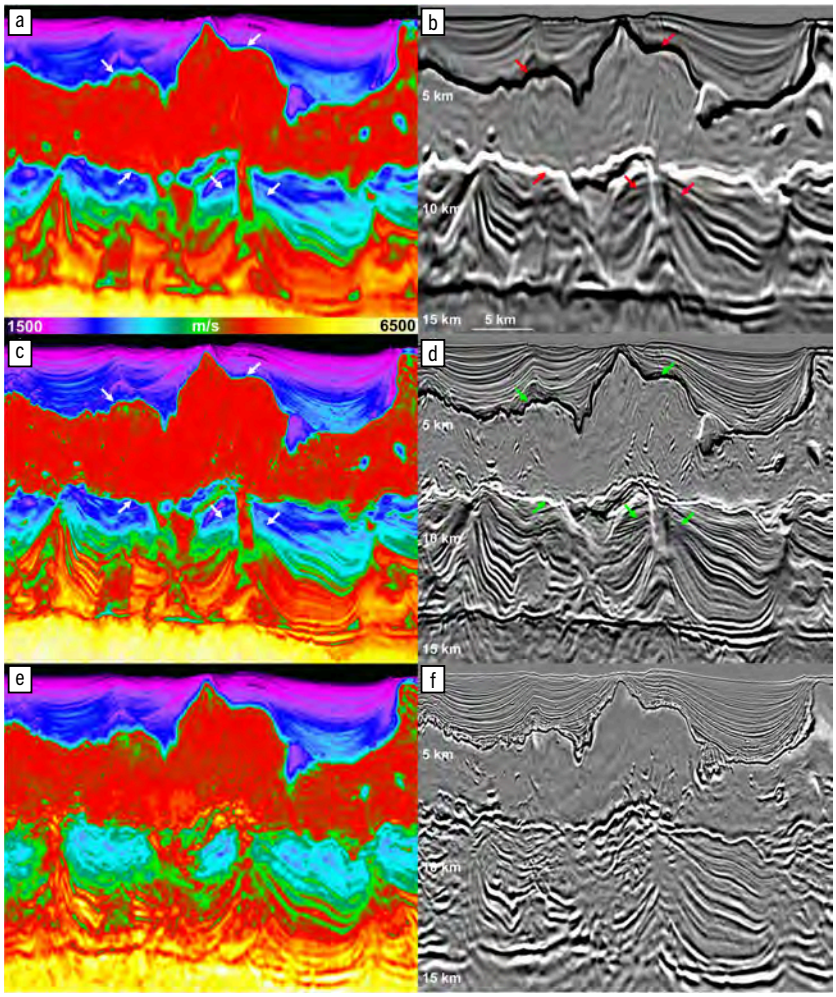

Figure 14. (a) 5 Hz OBN EFWI velocity model and (b) corresponding EFWI Image; (c) 12 Hz OBN + streamer EFWI velocity model and (d) EFWI Image; (e) 6 Hz streamer AFWI velocity model and (f) 15 Hz streamer RTM image. As the inversion bandwidth increases from 5 to 12 Hz, the salt halo contracts and resolution increases — top-down — in the velocity model and the FWI Image. The 12 Hz OBN + streamer EFWI results (c and d) show clearer subsalt stratigraphy and more coherent events than the streamer-only results (e and f), demonstrating the benefit of OBN-derived kinematics and FWI imaging for tracking fine-scale events from deep subsalt into feeder flanks.

Conclusions

The step change achieved in Laconia subsalt imaging confirms the effectiveness of the proposed LOLF sparse OBN plus FWI combination in areas with complex geology, emphasizing the importance of acquiring FWI-friendly data — with the necessary offsets, frequencies, and azimuthal coverage. The project highlights the practical scalability of such designs, which has been further improved when coupled with innovations developed and implemented during the project, for example, the pressure regulator system.

Higher-frequency EFWI using OBN and legacy streamer data provides an even richer characterization of subsalt reservoirs. Laconia confirms that the convergence of innovative acquisition design, operational scalability, and advanced FWI algorithms unlocks new levels of imaging fidelity in deepwater exploration.

Ultimately, Laconia demonstrates that the path to better imaging lies not in acquiring more data, but in acquiring the right data in the right way — at the right scale. TLE

Acknowledgments

We thank Viridien for permission to publish this work and acknowledge the valuable contributions of its Subsurface Imaging team, whose continued commitment to technology development and operational excellence made the Laconia program possible. We are grateful to TGS for their close partnership throughout the project lifecycle and to Sercel for their technical expertise, collaborative approach, and on-going support during planning, acquisition, and processing of the Laconia surveys. We extend our appreciation to the many individuals who played key roles in the program's success: Scott Downie and Michael Whitehead (Viridien) for program management and coordination; Alain Viau (Viridien) for permitting oversight and engagement with regulators; Dillon Thomassee (TGS) for project management and commercial alignment; Joe Zhou and Christian Milne (Viridien) for business sponsorship and strategic guidance; Curt Schneider (TGS) for source and field expertise; Dan Carruthers (Viridien) for interpretation expertise and integration of the results into subsurface workflows;

Downloaded from http://pubs.geoscienceworld.org/seg/tle/article-pdf/45/2/73/7765650/tle-v45-n2.pdf by Shivaji Maitra on 19 February 2026

and Julien Large (Sercel) for technical support and implementation of the source technology. Their collective contributions to operations, technical innovation, and interpretation were essential to advancing this work and to demonstrating the value of the Laconia program to the wider Gulf of Mexico exploration community. We also thank the TLE editorial team for the invitation to share our work in this publication and for their constructive guidance during the review and revision process.

Data and Materials Availability

Acquisition data and derived imaging products from the Laconia program are proprietary to Viridien and its commercial partners and are therefore not publicly available. Because these data form part of an actively marketed multiclient product, unrestricted release through a public repository is not possible at this time. However, aggregate metadata required to reproduce the survey design and acquisition concept (e.g., node spacing, source configuration and parameters, source/receiver geometry, and nominal shooting schedule) are documented within this article and its figures. These materials are sufficient for readers to understand and replicate the overall experimental design and to benchmark against comparable surveys. Additional non-confidential technical information may be provided by the authors upon reasonable request and subject to commercial, licensing, and confidentiality constraints.

Corresponding author:
ricardo.demarcocenteno@viridiengroup.com

References

Chelminski, S., F. Chelminski, G. Steel, S. Ronen, G. Baeten, T. Chen, K. Hunt, et al, 2021, Sea trial of a low-frequency enhanced pneumatic source: 1st International Meeting for Applied Geoscience & Energy, Denver, CO and virtual, SEG/AAPG, Expanded Abstracts, 11–15, https://doi.org/10.1190/segam2021-3594214.1.

Dellinger, J., A. J. Brenders, J. R. Sandschaper, C. Regone, J. Etgen, I. Ahmed, and K. J. Lee, 2017, The garden banks model experience: The Leading Edge, **36**, no. 2, 64–71, https://doi.org/10.1190/tle36020151.1.

Elboth, T., and V. Vinje, 2019, System and method for generating dithering sequences for seismic exploration.US patent US 2019/0120990.

Ji, S., Z. Yang, R. De Marco Centeno, H. Zhu, and B. Wray, 2025, Acquisition and early imaging of a long-offset, low-frequency sparse node survey in the Gulf of Mexico: 5th International Meeting for Applied Geoscience & Energy, SEG/AAP, Expanded Abstracts.

Jonke, K., J. Kang, S. Garzon, G. Alexander, G. Xia, G. Ritter, and A. Afifi, 2024, Unraveling US GoM North Green Canyon subsalt complexities with sparse nodes: Fourth International Meeting for Applied Geoscience & Energy, Houston, Texas, SEG/AAPG, Expanded Abstracts, 1460–1463, https://doi.org/10.1190/image2024-4100566.1.

Lin, F., B. Asmerom, R. Huang, B. Kuntz, G. Gehman, and M. Tanis, 2018: Improving subsalt reservoir imaging with reflection FWI: An OBN case study at Conger field, Gulf of Mexico: SEG Annual Meeting, Expanded Abstracts, https://doi.org/10.1190/segam2018-2996264.1.

Lin, F., D. Ren, J. Mei, Z. Xue, J. Blanch, M. Cahoj, J. Jarvis, et al, 2021, Exploring the full potential of a sparse nodes survey in the western Gulf of Mexico: 1st International Meeting for Applied Geoscience & Energy, Denver, CO and virtual, SEG/AAPG, Expanded Abstracts, 51–55, https://doi.org/10.1190/segam2021-3584248.1.

Merritt, M., G. Baeten, V. Rambaran, K. Godfrey, K. Bianchini, T. Brothers, F. Chelminski, et al, 2024, Revealing the subsalt in Garden Banks with a sparsely-shot TPS OBN and FWI: 4th International Meeting for Applied Geoscience & Energy, Houston, Texas, SEG/AAPG, Expanded Abstracts, 958–961, https://doi.org/10.1190/image2024-4099710.1.

Ren, D., X. He, S. Xu, F. Gao, F. Lin, and J. Mei, 2022, FWI for the complex Walker Ridge salt province using streamer data: 2nd International Meeting for Applied Geoscience & Energy, Houston, Texas, SEG/AAPG, Expanded Abstracts, 822–826, https://doi.org/10.1190/image2022-3744364.1.

Rentsch, S., E. Hager, L. Wing, and S. Holland, 2022, Enhancing low frequencies in airgun arrays, analysis of various field tests: 2nd International Meeting for Applied Geoscience & Energy, Houston, Texas, SEG/AAPG, Expanded Abstracts, 26–30, https://doi.org/10.1190/image2022-3745670.1.

Ronen, S., and S. Chelminski, 2017, Tuned pulse source -- A new low frequency seismic source: 87th Annual International Meeting, Houston, Texas, SEG, Expanded Abstracts, 6085–6088, https://doi.org/10.1190/segam2017-w16-04.1.

Shang, X., M. Kryvohuz, H. Macintyre, G. Baeten, T. Allemand, P. Herrmann, S. Laroche, et al, 2023, Broadband data with a new low frequency source — Acquisition and processing example from the Gulf-of-Mexico: International Meeting for Applied Geoscience & Energy, Houston, Texas, SEG) Expanded Abstracts(, https://doi.org/10.1190/image2023-3915083.1.

Shen, X., I. Ahmed, A. Brenders, J. Dellinger, J. Etgen, and S. Michell, 2017, Salt model building at Atlantis with full-waveform inversion: 87th Annual International Meeting, Houston, Texas, SEG, Expanded Abstracts, 1507–1511, 1507, https://doi.org/10.1190/segam2017-17738630.1.

Shen, X., I. Ahmed, A. Brenders, J. Dellinger, J. Etgen, and S. Michell, 2018, Full-waveform inversion: The next leap forward in subsalt imaging: The Leading Edge, **37**, no. 1, 67b1–67b6, https://doi.org/10.1190/tle37010067b1.1.

Udengaard, C., D. Brookes, H. Flores, and M. Rocke, 2024, An enhanced source for modern marine seismic surveys: 85th Annual Meeting, EAGE, Expanded Abstracts, Oslo, Norway, https://doi.org/10.3997/2214-4609.202410567.

Wang, P., Z. Zhang, J. Mei, F. Lin, and R. Huang, 2019, Full-waveform inversion for salt: A coming of age: The Leading Edge, **38**, no. 3, 204–213.

Wu, Z., Z. Wei, Z. Zhang, J. Mei, R. Huang, and P. Wang, 2022, Elastic FWI for large impedance contrasts: 2nd International Meeting for Applied Geoscience & Energy, Houston, Texas, SEG/AAPG, Expanded Abstracts, 3686–3690, https://doi.org/10.1190/image2022-w17-02.1.

Zhang, Z., J. Mei, F. Lin, R. Huang, and P. Wang, 2018, Correcting for salt misinterpretation with full-waveform inversion: 88th Annual International meeting, Anaheim, California, SEG, Expanded Abstracts, 1143–1147, https://doi.org/10.1190/segam2018-2997711.1.

Downloaded from http://pubs.geoscienceworld.org/seg/tle/article-pdf/45/2/73/7765650/tle-v45-n2.pdf by Shivaji Maitra on 19 February 2026

Enhancing deep pre-carbonate imaging with DAS VSP mode-converted energy: Unlocking deeper exploration potential in the prolific Asia Pacific basins

Riaz Alai[1], Ahmad Riza Ghazali[1], Faizan Akasyah Ghazali[1], Ming Heng Pua[1], Edysuzaily B Kamarudin[1], Garry B Malo-Paul[1], Hasnor Farhana Hasnan[1], Gundogan Coskun[1], Yusliza Bt M Sufian[1], Sandeep Kumar[1], Mohamad Rizam Sarif[1], Khairul Hamidi B Khalid[1], Mitch Preston[2], Shuqian Dong[2], Ge Zhan[2], Faqi Liu[2], Rachel Collings[2], Simon Shaw[3], and Oscar Barrios-Lopez[3]

https://doi.org/10.1190/tle-2025-1023

Abstract

The South Asia region hosts multiple prolific play types in its Tertiary basins. It is common to see cycles of carbonates and siliciclastic reservoir targets distributed from very shallow levels to deep early basin fills. The presence of thick, high-impedance carbonate layers with highly variable geometry at mid-section poses significant challenges for imaging productive deeper target levels. Over the years, numerous studies have explored methods to enhance pre-carbonate imaging, from acquisition strategies to the application of specialized technologies during seismic data processing. Here, mode conversions at the high-impedance contrast interfaces of these carbonate layers were explored and used in improving imaging of the target sections. In a shallow-water survey in the Asia Pacific region, surface data (marine and ocean-bottom node) and borehole data (3-component vertical incidence vertical seismic profiling [VSP] and 3D distributed acoustic sensing [DAS] VSP) were acquired to advance subsurface imaging. In standard DAS VSP data processing workflows, energy not associated with primary P-waves is often attenuated or removed as noise. In contrast, the importance of this noise, comprising mode-converted and multiple energy, was highlighted, as it played a critical role in improved pre-carbonate imaging. Imaging using this mode-converted and multiple energy was shown to have great potential to provide additional insight into the reservoir structures beneath the shallow carbonates. A 3D VSP survey using a wireline fiber-optic cable was conducted in a deviated well. Despite the single-component limitation of DAS recording, the acquired 3D DAS VSP data captured P-waves and notable converted waves, resulting from mode conversions within a shallow, high-velocity carbonate layer. This paper highlighted key findings from the analysis of the 3D DAS VSP data and examined the possibility of using converted waves and multiple energy for DAS VSP deeper carbonate imaging in a geologically complex setting.

Introduction

Seismic imaging in complex carbonate settings, particularly in shallow-water environments, remains highly challenging. These difficulties originate from a complex overburden dominated by a shallow, high-velocity carbonate layer with strong acoustic impedance contrasts. As a result, conventional surface seismic data often produce poor-quality images with limited continuity of subsurface reflectors. To address these limitations and improve the imaging fidelity, four complementary data sets were acquired: marine streamer data for initial velocity model building and broad coverage, an ocean-bottom node (OBN) configuration to enhance the low-frequency content and accommodate full-azimuth illumination, a 3-component vertical incidence vertical seismic profiling (3-C VIVSP) for anisotropy analysis and high-resolution borehole imaging, and 3D distributed acoustic sensing (DAS) VSP data for dense spatio-temporal sampling and improved vertical resolution. This integrated acquisition strategy was designed to address imaging challenges and to enable advanced processing workflows such as elastic inversion, reverse time migration (RTM), and high-fidelity reservoir characterization (see Figure 1).

Figure 2 [left] shows a perspective view of the surface shot locations (in red) and the geometry of the downhole fiber-optic cable used in the 3D DAS VSP (in blue and orange). A reservoir horizon is also highlighted in yellow within the same plot. The data acquisition covered a source patch measuring 8 km × 8 km, with a shot spacing of 50 m × 50 m, resulting in a total of 24,400 shot points. Figure 2 [right] presents six raw DAS VSP shot gathers sampled at various offsets along a single-shot line (the source locations are indicated by green dots in Figure 2 [left]). These field records demonstrate DAS VSP data with a reasonably good signal-to-noise ratio, despite being acquired using wireline fiber, which is known for suboptimal coupling. Additionally, it was observed that the

Manuscript received 2 September 2025; revision received 22 October 2025; accepted 3 November 2025.

[1]PETRONAS Carigali Sdn. Bhd., Kuala Lumpur, Malaysia. E-mail: riaz.alai@petronas.com; rizag@petronas.com; faizan_akasyah@petronas.com; pua.mingheng@petronas.com; edysuzaily_kamarudin@petronas.com; garrymalo@petronas.com; farhana.hasnan@petronas.com; gundogan.coskun@petronas.com; yusliza_s@petronas.com; sandeepkumar@petronas.com; mrizam.sarif@petronas.com; hamidik@petronas.com.

[2]TGS, Houston, Texas, USA. E-mail: mitch.preston@tgs.com; shuqian.dong@tgs.com; ge.zhan@tgs.com; faqi.liu@tgs.com; rachel.collings@tgs.com.

[3]Halliburton, Houston, Texas, USA. E-mail: simon.shaw@halliburton.com; oscaraugusto.barrios@halliburton.com.

Downloaded from http://pubs.geoscienceworld.org/seg/tle/article-pdf/45/2/73/7765650/tle-v45-n2.pdf by Shivaji Maitra on 19 February 2026

upgoing P-wave (P-Up) signal for shots located opposite to the well deviation is weak, and in some cases absent, due to the inherent fiber directivity in DAS acquisition, whereas the upgoing P-to-S converted wave (PS-Up) signal can be strongest for these shots.

DAS used for VSP has emerged as a transformative tool for subsurface characterization, using existing fiber-optic cables as dense seismic arrays to deliver high-resolution imaging without geophones (Mateeva et al., 2012). This approach reduces costs, broadens monitoring accessibility, and has proven effective in exploration and carbon storage projects. Studies highlight its scalability across diverse geologic settings, including time-lapse monitoring to track subtle subsurface changes (Daley et al., 2013). Recent advances in full-waveform inversion (FWI) and imaging workflows further enhance resolution and velocity model building (Liu et al., 2025Zhan et al., 2024). Multiwell surveys with preinstalled fiber-optic cables extend subsurface illumination beyond the borehole (Zhan and Nahm, 2020), and the integration of surface and borehole data enables true-3D imaging beneath complex overburdens (Ghazali et al., 2018). Recent advances in processing techniques include the use of deep learning for denoising and wavefield separation (Cheng et al., 2025). All these developments position 3D DAS VSP as a versatile and increasingly mature technology with significant geophysical applications.

Alai et al. (2024) challenge conventional imaging approaches in complex carbonate environments by integrating mode-converted shear waves and electromagnetic data to reduce interpretational ambiguity and enhance subsurface characterization. Alai et al. (2025) demonstrate the value of imaging shear waves in carbonate environments identified from DAS VSP data.

Figure 3 illustrates the comparison of VIVSP shots recorded using geophones and DAS. Note the interesting similarities observed in both displays. For the DAS VSP data, selective source–receiver extractions have been made to match the source–receiver Walkabove VSP configuration for optimal comparison of both VSP data. The analysis of the recorded DAS VSP data revealed essential acoustic-to-elastic wave mode conversions at the carbonate layer.

To better understand the mode-converted energy in DAS VSP data, elastic finite-difference modeling was performed. Figure 4a shows a complex overburden (the velocity model was estimated from the streamer data), dominated by a shallow, high-velocity carbonate layer with significant acoustic impedance. Figure 4b shows a snapshot of mode conversions obtained using constant-density elastic forward numerical modeling. A linear V_P–V_S relationship was derived from the compressional- and shear-sonic logs via least-squares regression, ensuring the best agreement between estimated and observed V_S, and then applied to the streamer 3D V_P model (Figure 4a) to obtain the V_S model.

Figure 4c and 4d shows the comparison of elastic modeled and field data, emphasizing their similarities and confirming that downgoing P-waves undergo multiple mode conversions at the top of carbonate (TOC) and base of carbonate (BOC), generating prominent P-to-S converted waves.

These converted waves significantly interfere with P-waves, posing challenges for conventional VSP imaging that relies on P-wave data only. On the other hand, because mode-converted waves are dominant over P-waves, they provide additional insight into pre-carbonate imaging.

VSP wavefield separation and shear velocity estimation

As shown in Figures 1–4, the DAS VSP data show a reasonably good signal-to-noise ratio, despite being acquired using wireline fiber.

Imaging VSP converted waves requires isolating the upgoing converted wavefield from the full wavefield, making wavefield separation a critical step in the processing workflow. In this paper, the separation was performed in two stages: the full wavefield was separated into upgoing and downgoing components using a dip-separation-based approach.

In addition, the upgoing wavefield was decomposed into upgoing PP- and PS-wave components based on their moveout characteristics (Figure 5a [left] and [center]). Ray-tracing-based moveout correction was applied to flatten the upgoing P-wave events in the shot domain, after which P-wave energy was separated from the PS signal via curvelet-domain filtering. Figure 5a [right] presents a color-coded integrated display of the upgoing S-waves (red) overlaid on the upgoing P-waves (blue), highlighting that the upgoing S-waves are more prominent

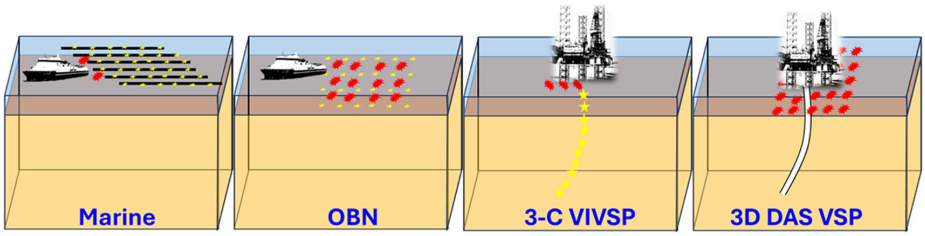

Figure 1. Different acquisition types (from left to right): marine streamer data, OBN data, 3-C VIVSP data, and 3D DAS VSP data.

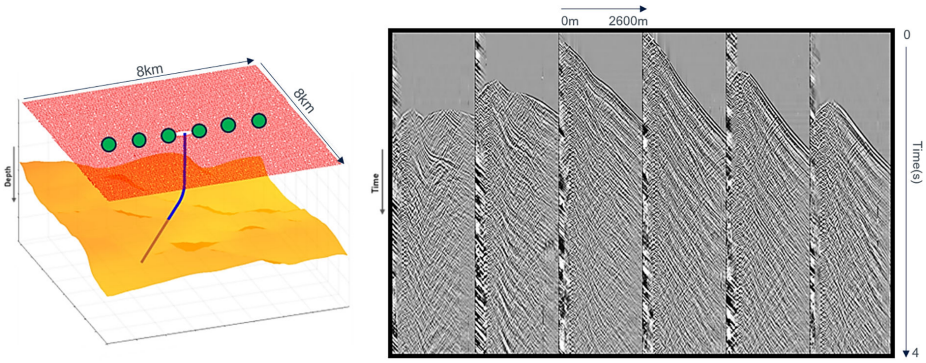

Figure 2. A 3D view of the acquisition geometry and display of six field DAS VSP shot gathers at various offsets. The green dots indicate the source locations.

Downloaded from http://pubs.geoscienceworld.org/seg/tle/article-pdf/45/2/73/7765650/tle-v45-n2.pdf by Shivaji Maitra on 19 February 2026

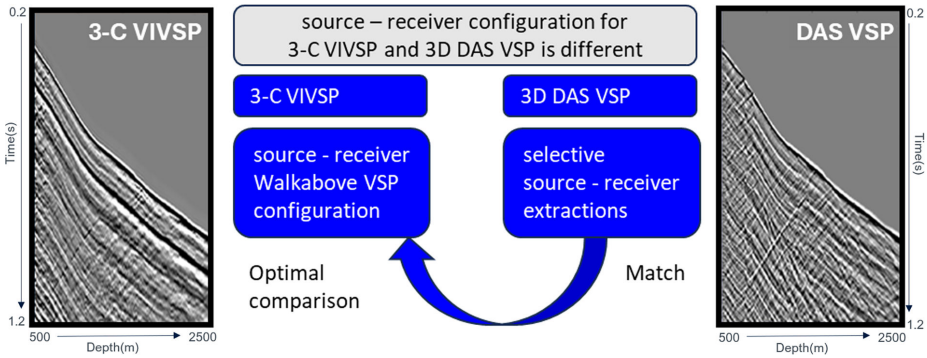

Figure 3. Comparison of VIVSP shots recorded using geophones and DAS: vertical component of geophone VSP data [left] and DAS VSP data [right]. For the DAS VSP, selective source–receiver extractions have been made to match the source–receiver Walkabove VSP configuration for optimal comparison of both VSP data.

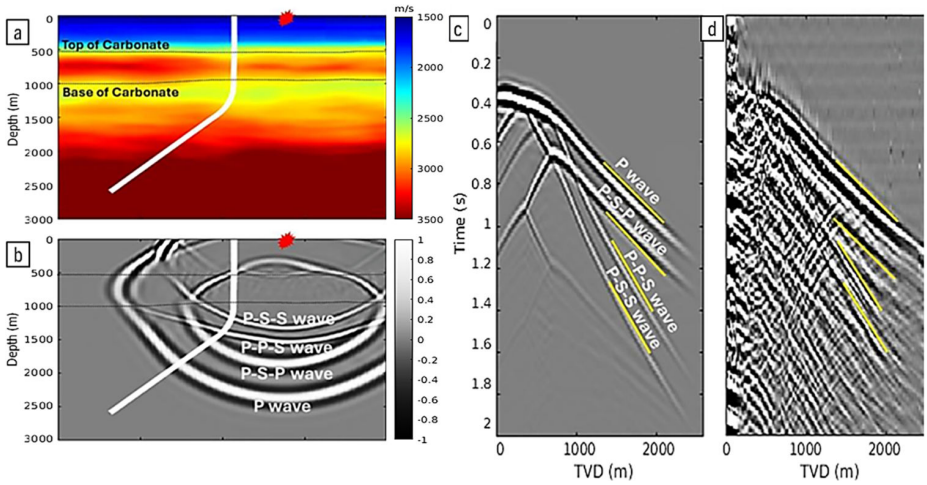

Figure 4. Wave mode conversions with P-waves propagating through a carbonate layer: (a) P-wave velocity model, with the red dot indicating the surface shot location and the white line representing the fiber-optic cable; (b) snapshot of the elastic wavefield, highlighting multiple mode conversions at the carbonate layer; (c) synthetic modeled VSP; and (d) DAS VSP.

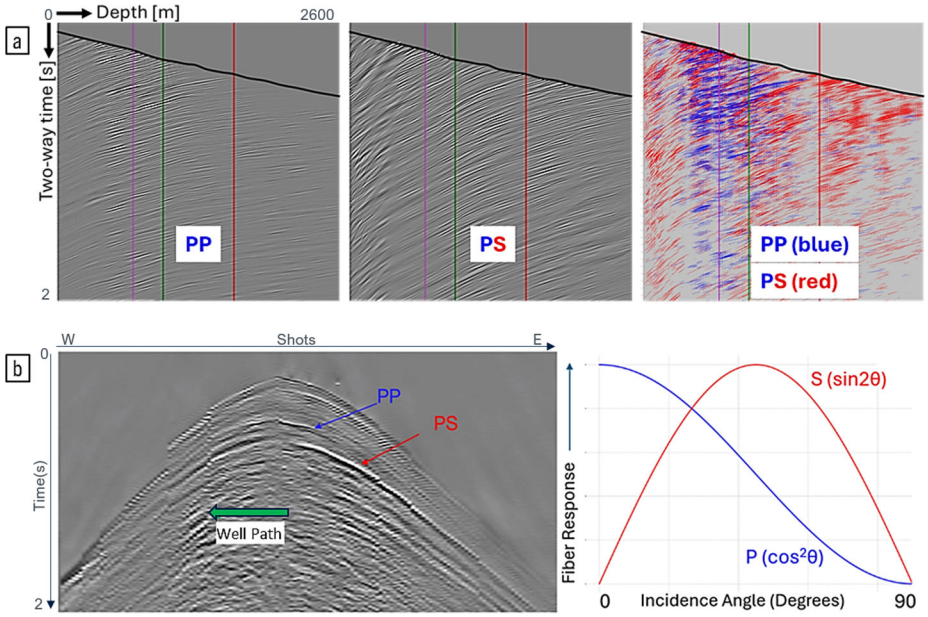

Figure 5. Upgoing waves in DAS VSP data: (a) from left to right: PP waves, PS waves, and integrated display of PS waves (red) overlaid on PP waves (blue). (b) DAS VSP channel gather showcasing PP versus PS signal dominance on a sail line parallel to the well path [left] and plot of theoretical fiber response to P ($\cos^2\theta$) and S ($\sin 2\theta$) waves [right].

than the upgoing P-waves, particularly in the deeper deviated section of the fiber.

The recorded amplitude in DAS depends on the incidence angle θ between the incoming wavefield and the fiber axis. The P-wave response scales as $\cos^2\theta$ (blue curve, Figure 5b [right]): it is maximum for waves parallel to the fiber (θ = 0°) and decreases toward zero at 90°. The shear-wave response scales as $\sin 2\theta$ (red curve, Figure 5b [right]), vanishing at 0° and 90° and peaking at 45°. The S response exceeds the P response for θ > 26.6° (where $\cos^2\theta = \sin 2\theta$). This trend appears in the channel gather from the deviated section (Figure 5b [left]). There is a clear transition where the P-wave energy diminishes, whereas PS energy strengthens and becomes dominant energy in the record.

For improved understanding of the acquired DAS VSP data, Figure 6 shows the recordings for a source offset of 1500 m. Note the shallow water multiples: the P-wave interbed multiples bouncing between water bottom (WB) and TOC and the P-wave and S-wave interbed multiples bouncing between the TOC and BOC. It is noted that the mode-converted S-waves are dominant (indicated with the red arrows) in the pre-carbonate section.

It is interesting to observe the interbed multiples generated at the BOC: the wave propagation and reflections colored indicate P-wave (blue) and S-wave (red) interbed multiples generated at the BOC. This important finding emphasizes that using P-waves alone makes it very challenging to obtain high-quality and accurate actual pre-carbonate images.

The DAS VSP data were obtained to improve the mapping of geologic structures and deliver more accurate insights into the VSP well, especially for characterizing reservoirs beneath the shallow carbonate layer. As emphasized above, in early stages of processing DAS VSP data, all signals not associated with P-waves are

Downloaded from http://pubs.geoscienceworld.org/seg/tle/article-pdf/45/2/73/7765650/tle-v45-n2.pdf by Shivaji Maitra on 19 February 2026

typically eliminated from the data. In this paper, we recommend retaining these; however, for illustrative purposes, we present the following example. Figure 7a shows three shots parallel to the well path, full wavefield (grayscale), input to FWI after PS attenuation (blue). To achieve these gathers, forward elastic numerical modeling was performed to accurately model all mode-converted energy followed by the removal of all of these from the shot gathers. Figure 7b illustrates the cross-correlation maps of the direct arrival between field and synthetic data modeled using acoustic engine for FWI updates (from left to right): starting model, 10, 12, and 15 Hz. Stronger blue and red values represent high mismatch, whereas white represents a good match.

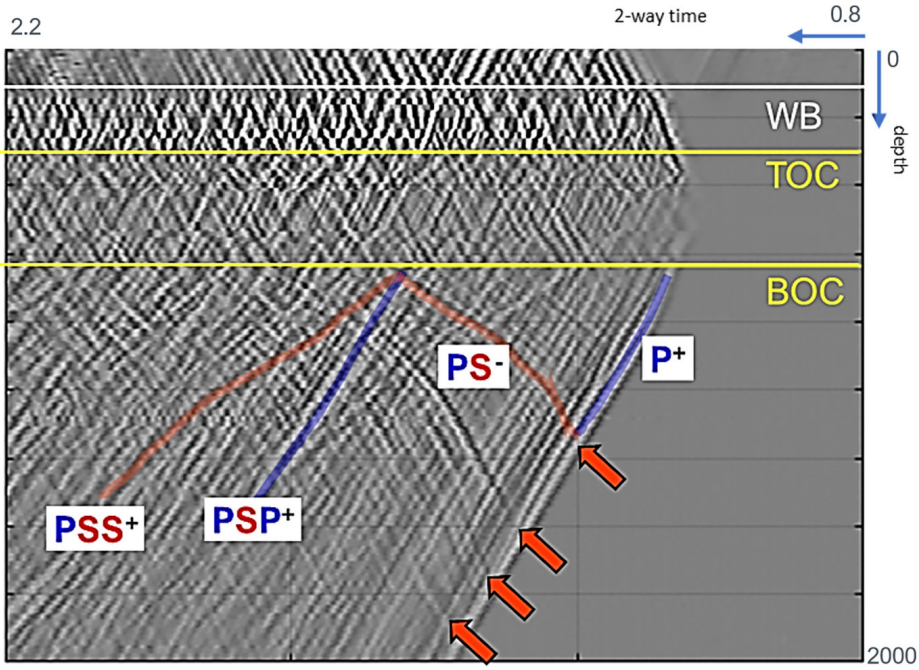

Figure 6. 3D DAS VSP data for a source offset of 1500 m. Note the shallow water multiples: the P-wave interbed multiples bouncing between WB and TOC and the P-wave interbed multiples bouncing between the TOC and BOC. Interestingly, in the pre-carbonate section, mode-converted S-waves are dominant (red arrows). The colored wave propagation and reflections indicate P-wave (blue) and S-wave (red) interbed multiples generated at BOC. This important finding emphasizes that using P-waves alone makes it very challenging to obtain high-quality and accurate deeper pre-carbonate images.

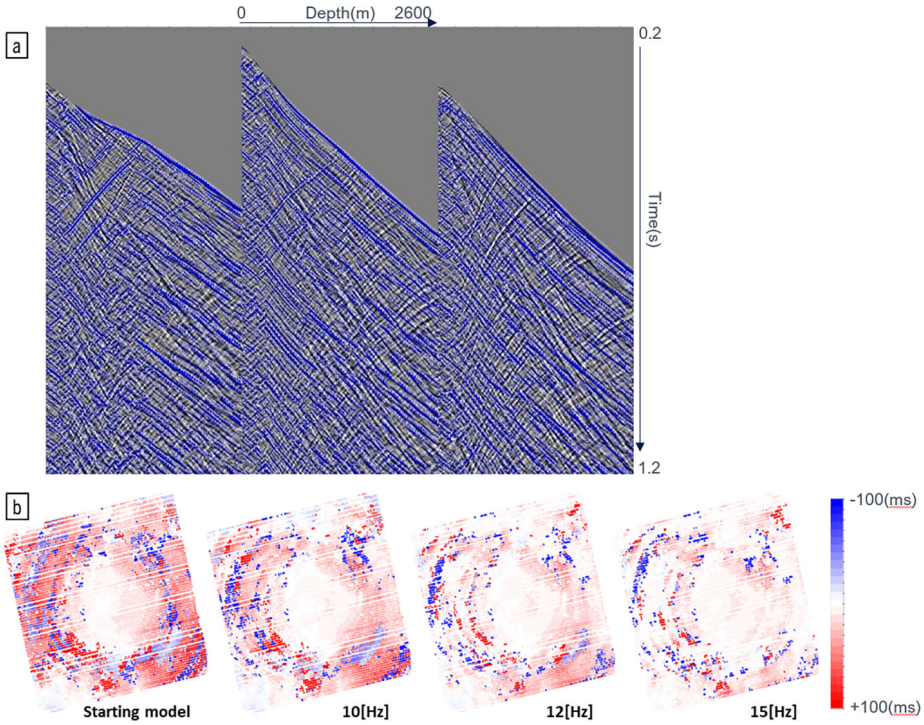

Figure 7. (a) Three shots parallel to the well path, full wavefield (grayscale), input to FWI after PS attenuation (blue). (b) Cross-correlation misfit maps of the direct arrival between field and synthetic acoustic modeling for FWI updates (from left to right): starting model, 10, 12, and 15 Hz. Stronger blue and red values represent high mismatch, whereas white represents a good match.

Converted waves and multiple imaging with RTM

Using the P-wave interval velocity estimated from the acoustic FWI, we first used RTM to generate a P-Up image. Compared with the marine surface-seismic image, the 3D DAS VSP P-Up image shows a broader bandwidth and higher dominant frequencies. This is a typical benefit of VSP acquisition: borehole receivers are closer to the formation, so the upgoing wavefield travels a shorter, less-attenuative path in the subsurface.

Figure 8a shows the comparisons of the DAS VSP P-Up image [left] and DAS VSP PS-Up image [center]. Imaging the primaries shows that the illumination area obtained from using the upgoing wavefields is limited to around the borehole and is not present within the shallow section where no receivers are present. To overcome this, imaging with multiples (Lu et al., 2015), also known as separated wavefield imaging (SWIM), was used to extend the illumination area and obtain an image of the near surface (Figure 8a [right]). SWIM uses each shot as a "virtual" receiver, expanding the surface coverage of the seismic experiment to the shot patch and enhancing the subsurface illumination. This results in a survey that has a spatial sampling richer in offsets and azimuths. The improved spatial sampling greatly enhances the angular diversity of the data at every image point, which results in the imaging of reflectivity above the fiber.

Figure 8b shows the multiple imaging raypath diagrams (from left to right): P-Down direct

Downloaded from http://pubs.geoscienceworld.org/seg/tle/article-pdf/45/2/73/7765650/tle-v45-n2.pdf by Shivaji Maitra on 19 February 2026

arrival, P-Down first-order surface-related multiples, P-Down second-order surface-related multiples, and P-Down higher order surface-related multiples.

A comparison between the streamer seismic Kirchhoff prestack depth migrated (KPSDM) image (Figure 9 [left]) and the 3D DAS VSP multiple image (Figure 9 [center]), and the cross-correlation between them (Figure 9 [right]) shows clearly their similarities between both data sets, with DAS VSP data exposing higher frequency content. Both seismic sections have been stretched to two-way time with their own respective velocities for the cross-correlation applications. All sections have been mapped back to depth for comparison purposes (Figure 10). It should be noted that the imaging of multiples of 3D DAS VSP covers only a certain lateral distance around the well but has significantly contributed to the lateral imaging in comparison with imaging primaries only.

Prior to migrating the upgoing converted waves, a shear model (V_S) was determined using the sonic and shear logs.

The PS imaging input was generated by first aligning the upgoing PS arrivals. We computed PS traveltimes via ray tracing using the P-wave velocity for the downgoing leg and the S-wave velocity for the upgoing leg and applied the resulting dual-velocity moveout to flatten PS events in the shot domain. After flattening, curvelet-domain filtering suppressed PP leakage and incoherent noise.

The upgoing S-waves were migrated using reciprocity with dual-velocity acoustic RTM as proposed by Alai et al. (2022).

In this approach, the forward source propagation is carried out downhole using the constructed S-wave velocity, whereas the upgoing S-wave field is backward propagated from surface shot locations to the subsurface using either the P-wave velocity or various types of converted wave velocities. This process is graphically illustrated in the ray diagrams shown in Figure 11a.

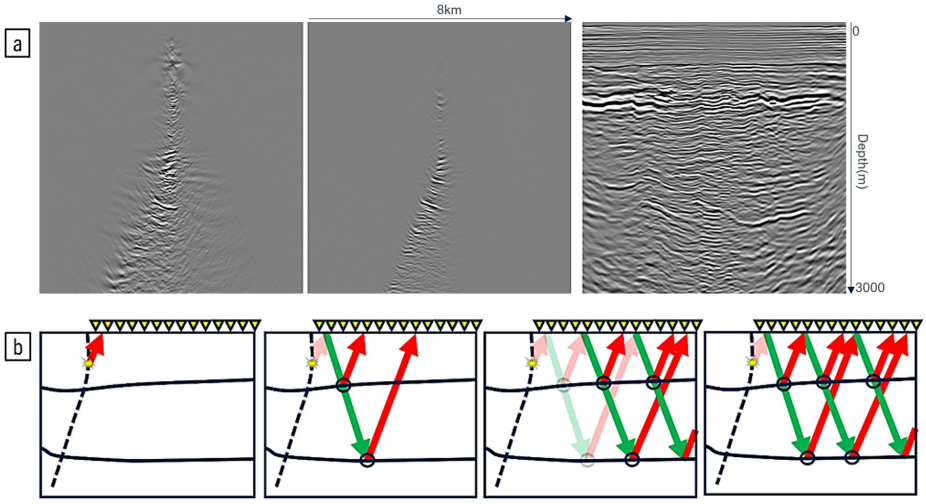

Figure 8. (a) DAS VSP P-Up image [left], DAS VSP PS-Up image [center], and DAS VSP multiple image using all-order surface-related multiples [right]. (b) Multiple imaging raypath diagrams (from left to right): P-Down direct arrival, P-Down first-order surface-related multiples, P-Down second-order surface-related multiples, and P-Down all-order surface-related multiples.

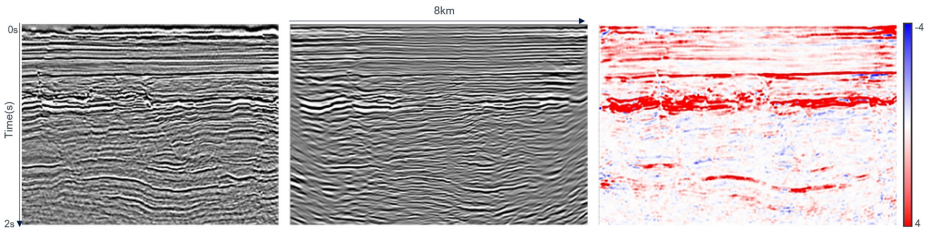

Figure 9. Streamer seismic KPSDM raw image [left], 3D DAS VSP multiple image [center], and cross-correlation between both [right]. Both seismic sections have been stretched to two-way time with their own respective velocities for the cross-correlation applications.

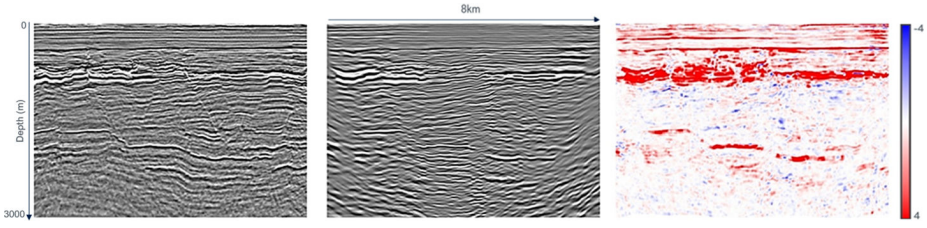

Figure 10. Streamer seismic KPSDM raw image [left], 3D DAS VSP multiple image [center], and cross-correlation between both [right]. Both seismic sections have been stretched to two-way time with their own respective velocities for the cross-correlation applications, and all sections have been mapped back to depth for comparison purposes.

For comparison purposes, the surface seismic PP image (grayscale) and the conventional DAS VSP image of the upgoing P-waves (PPPP) are shown in Figure 11b (left and center, respectively). Note that the VSP images are overlaid in gold color on the surface seismic across the wellbore direction. Figure 11b [right] demonstrates improved imaging of deeper reflectors (indicated by the yellow arrow) using upgoing shear waves (PPPS). Figure 11c shows a schematic ray diagram illustrating some possible mode-converted PSPP, PPPS, and PSPS waves in carbonate settings. These are a subselection of all the possible configurations PPPP, PPSP, PSPP, PSSP, PPSS, PSPS, and PSSS.

Finally, Figure 12 shows the comparison of the KPSDM surface data and DAS VSP RTM images using mode-converted waves. Note the depth coincidence of all the images (indicated with yellow and cyan arrows), even though dual velocities have been used in the RTM. The orange arrows indicate the improved deeper imaging.

The strong alignment between the DAS VSP converted wave images and the surface seismic image demonstrates that this complex carbonate geologic setting is well-suited for using converted waves in DAS VSP imaging. Furthermore,

Downloaded from http://pubs.geoscienceworld.org/seg/tle/article-pdf/45/2/73/7765650/tle-v45-n2.pdf by Shivaji Maitra on 19 February 2026

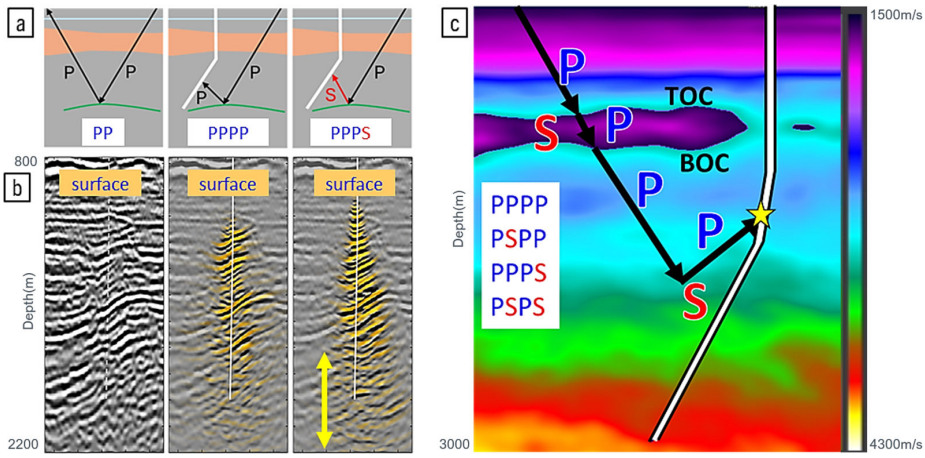

Figure 11. (a) Composite plot with ray diagrams, (b) surface seismic image (grayscale) and DAS VSP PPPP and PPPS images (gold) overlaid on surface seismic across wellbore direction, and (c) schematic diagram illustrating possible mode-converted PSPP, PPPS, and PSPS waves in carbonate settings with the TOC and BOC. Only a subselection of all the possible configurations PPPP, PPSP, PSPP, PSSP, PPSS, PSPS, and PSSS is shown.

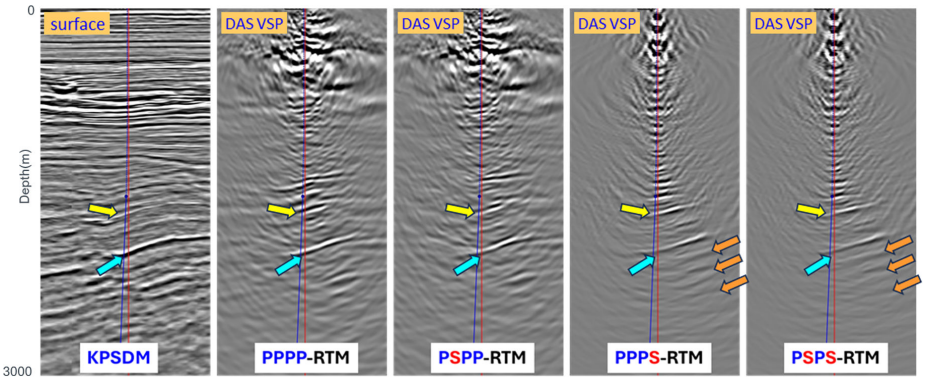

Figure 12. Comparisons of migrated images (from left to right): KPSDM, PPPP RTM, PSPP RTM, PPPS RTM, and PSPS RTM. Note the depth coincidence of all images (yellow and cyan arrows), even though dual velocities have been used in the RTM. Orange arrows indicate improved deeper imaging.

the DAS VSP converted wave images provide subsurface imaging comparable to the conventional P-wave images while also resolving additional features that complement the P-wave only images.

Conclusions

This paper introduces an innovative seismic imaging approach for complex carbonate environments by leveraging converted waves and multiple energy from DAS VSP data. Unlike conventional methods that rely heavily on P-wave data and often struggle beneath high-velocity carbonate layers, this study successfully used converted S-waves and multiples to improve subsurface resolution. The 3D DAS VSP data were acquired using a wireline-deployed fiber-optic cable in a shallow water setting, demonstrating the feasibility and effectiveness of this technique.

Rather than following industry standard routinely removing nonprimary-P-wave energy as noise in DAS VSP data, this paper demonstrated that these mode-converted waves and multiple energy can be used in deeper pre-carbonate imaging, opening deeper exploration opportunities. We imaged mode-converted energy to extract valuable information. Our analyses have provided critical insights into acoustic-to-elastic mode-converted waves within and beneath the carbonate layers.

The resulting images clearly demonstrate improvement in comparison to surface seismic and conventional DAS VSP upgoing P-wave images in the vicinity of the well.

Our success in imaging mode-converted energy in 3D DAS VSP data establishes a novel foundation for advanced elastic wavefield analyses in complex carbonate geologic settings.

Future processing of the OBN data and integration with the 3D DAS VSP may provide more accurate shear interval velocities. With joint updates of P- and S-wave interval velocities, full elastic RTM needs to be performed to achieve optimal results taking all elastic boundary conditions into account. TLE

Acknowledgments

The authors thank PETRONAS Management for the support and permission to publish the results. We thank TGS and Halliburton for the collaboration efforts.

Data and Materials Availability

PETRONAS is owner of the data. Therefore the data can not be released.

Corresponding author: riaz.alai@petronas.com

References

Alai, R., A. R. Ghazali, F. A. Ghazali, P. M. Heng, E. Kamarudin, M. Preston, S. Dong, et al., 2025, Insights from DAS VSP converted wave imaging in complex carbonate geological settings: Fifth International Meeting for Applied Geoscience & Energy, SEG/AAPG, Expanded Abstracts.

Alai, R., A. R. Ghazali, L. MacGregor, F. A. Ghazali, E. Kamarudin, A. H. Azmi, G. Malo-Paul, et al., 2024, Challenging preconceptions in complex carbonate imaging: Using shear waves and electromagnetic data for improved subsurface understanding: Fourth International Meeting for Applied Geoscience & Energy, SEG/AAPG, Expanded Abstracts, 587–591, https://doi.org/10.1190/image2024-4101222.1.

Alai, R., F. Liu, D. Armentrout, D. Brookes, T. Johnson, M. Cvetkovic, G. Coskun, et al., 2022, Improved subsalt imaging in Brazil Campos basin - cascaded application of hybrid interbed demultiple, P- and S-salt velocity joint migration, and subsalt converted wave

Downloaded from http://pubs.geoscienceworld.org/seg/tle/article-pdf/45/2/73/7765650/tle-v45-n2.pdf by Shivaji Maitra on 19 February 2026

suppression: Second International Meeting for Applied Geoscience & Energy, SEG/AAPG, Expanded Abstracts, 2680–2684, https://doi.org/10.1190/image2022-3740399.1.
Cheng, M., J. Lin, X. Dong, and T. Zhong, 2025, A multitask deep-learning model for the denoising, interpolation, and wavefield separation of distributed acoustic sensing-vertical seismic profiling data: Geophysics, **90**, no. 6, V559–V568, https://doi.org/10.1190/geo2024-0531.1.
Daley, T. M., B. M. Freifeld, J. Ajo-Franklin, S. Dou, R. Pevzner, V. Shulakova, S. Kashikar, et al., 2013, Field testing of fiber-optic distributed acoustic sensing (DAS) for subsurface seismic monitoring: The Leading Edge, **32**, no. 6, 699–706, https://doi.org/10.1190/tle32060699.1.
Ghazali, A. R., N. ElKady, M. F. Abd Rahim, R. J. J. Hardy, F. S. Dzulkelfi, S. Chandola, S. Kumar, et al., 2018, Reservoir delineation beneath a heterogeneous shallow gas overburden using 'True-3D' seismic imaging approaches: First Break, **36**, no. 11, 89–96, https://doi.org/10.3997/1365-2397.n0137.
Liu, F., C. Macesanu, H. Xing, M. Romanenko, G. Zhan, C. Calderón-Macías, and B. Wang, 2025, Elastic full-waveform inversion: Enhance imaging for legacy and modern acquisition: The Leading Edge, **44**, no. 5, 338–343, https://doi.org/10.1190/tle44050338.1.
Lu, S., D. N. Whitmore, A. A. Valenciano, and N. Chemingui, 2015, Separated-wavefield imaging using primary and multiple energy: The Leading Edge, **34**, no. 7, 770–778, https://doi.org/10.1190/tle34070770.1.
Mateeva, A., J. Mestayer, B. Cox, D. Kiyashchenko, P. Wills, J. Lopez, S. Grandi, et al., 2012, Advances in distributed acoustic densing (DAS) for VSP: 82nd Annual International Meeting, SEG, Expanded Abstracts, 1–5, https://doi.org/10.1190/segam2012-0739.1.
Zhan, G., F. Gao, R. Malik, M. Preston, C. Macesanu, H. Hu, C. Calderón, et al., 2024, Optimizing DAS VSP value through FWI imaging: 85th EAGE Annual Conference & Exhibition, 1–5, https://doi.org/10.3997/2214-4609.202410927.
Zhan, G., and J. Nahm, 2020, Multi-well 3D DAS VSPs: Illumination and imaging beyond the wellbores: 90th Annual International Meeting, SEG, Expanded Abstracts, 3798–3802, https://doi.org/10.1190/segam2020-3426032.1.

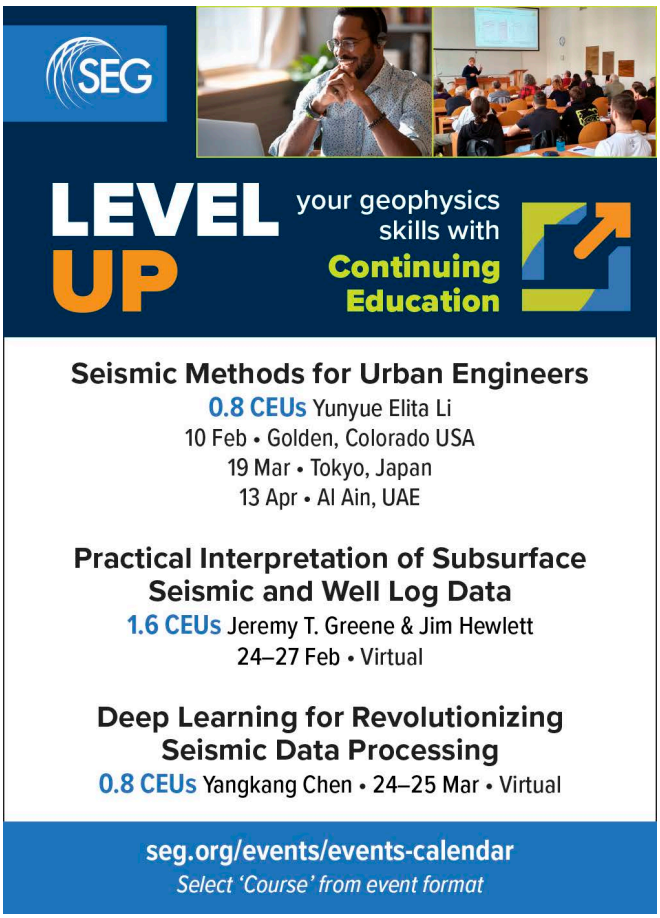



Downloaded from http://pubs.geoscienceworld.org/seg/tle/article-pdf/45/2/73/7765650/tle-v45-n2.pdf by Shivaji Maitra on 19 February 2026

Compressive sensing for seismic: From survey design to legacy data reconstruction

Tao Jiang[1], Joel Latchman[1], Peter Eick[1], Cody Meng[1], Lau Eng Chuan[2], M Nasrul B M Isa[2], Rika Burr[3], Jonathan Woolley[3], and Jinming Zhu[4]

https://doi.org/10.1190/tle-2025-1016

Abstract

Compressive sensing (CS) has emerged as a transformative approach for seismic acquisition, enabling sparser sampling while maintaining data quality. Although 1D CS designs along shot or receiver lines are well-suited for traditional surveys with large line spacing, modern acquisitions, such as ocean-bottom node (OBN) and high-density land surveys, require multidimensional optimization to mitigate spatial aliasing and improve cost efficiency. In this study, two novel applications of CS in seismic were introduced: (1) a 2D CS survey design framework leveraging mutual coherence (MC) maps to optimize source/receiver sampling in inline and crossline directions and (2) a legacy data bin-reduction method that uses MC maps to assist in reconstruction of high-resolution volumes from irregular historical acquisitions. The 2D CS framework was validated using SEG Advanced Modeling Corporation Phase II (SEAM II) synthetic data and an OBN field survey, demonstrating that it achieves about 5 dB higher signal-to-noise ratio (SNR) than 1D CS designs at equivalent sampling or reduces source/receiver requirements by 20% for comparable results. For legacy data, the MC maps provided a quantitative metric to assess reconstructability, enabling safe bin reduction to 75% of the original bin size while preserving the SNR, as demonstrated on a North American land data set. These advancements help bridge the gap between theoretical CS and field applications, offering practical guidelines for survey design and reprocessing. The MC map's dual role as a design optimizer for new acquisitions and a quality-control tool for legacy data establishes it as a unifying framework for compressive seismic across the data lifecycle.

Introduction

Seismic acquisition has long been constrained by the Nyquist–Shannon theorem, requiring dense, regular sampling to avoid aliasing artifacts. Although this paradigm ensures fidelity, it increases costs and logistical complexity, especially in modern surveys such as ocean-bottom node (OBN) or high-density land acquisitions, where sampling demands rise significantly in multidirectional geometries. Compressive sensing (CS) theory (Donoho and Elad, 2003; Candès, 2006Candes, Romberg, and Tao, 2006; Candes, Romberg, and Tao, 2006; Donoho, 2006) challenges this status quo by demonstrating that signals can be accurately recovered from sub-Nyquist sampling if two conditions are met: (1) sparsity: the data must be compressible in a transform domain (e.g., Fourier, curvelet, or tau-p) and (2) incoherency: the sampling strategy must avoid coherent aliasing by maximizing randomness relative to the sparsity domain.

Early CS applications in seismology focused either on 1D optimizations, such as jittered undersampling along lines (Hennenfent and Herrmann, 2008), regular-indexed CS field trials (Jiang et al., 2018; Lewis et al., 2024), or random sampling on 2D surfaces (Herrmann, 2010). Most production implementations to date have relied on 1D or simple 2D strategies due to ease of deployment and robustness. A notable example is a Permian Basin field case, where CS-based acquisition and reconstruction were successfully applied to address shallow anomalies and permit holes in a complex operating environment (Li et al., 2021).

Figure 1 illustrates representative examples: (a) orthogonal coarse survey, (b) dense nodal survey, (c) 1D CS survey derived from (a) with 50% sampling, and (d) 2D CS survey derived from (b) with 50% sampling. Although 1D remains the prevalent approach in field applications, 2D CS designs, especially those informed by optimization, offer future potential for improved spatial fidelity and efficiency in increasingly dense acquisition settings.

However, two critical challenges remain for advancing CS in seismic acquisition:

1) Multidimensional CS design: Although modern OBN and nodal surveys acquire densely sampled data in inline and crossline directions, most current CS implementations continue to treat each direction independently, primarily leveraging 1D optimizations. A truly 2D design, guided by objective criteria, has the potential to further reduce acquisition effort while controlling spatial aliasing, particularly in the context of high-density, multiazimuth geometries.
2) Legacy data potential: Vast volumes of historical seismic data, often acquired under logistical or environmental constraints, exhibit irregular sampling patterns. Applying

Manuscript received 12 August 2025; revision received 29 October 2025; accepted 21 November 2025.

[1]In-Depth Geophysical, Houston, Texas, USA. E-mail: taojiang@indepthgeo.com; jlatchman@indepthgeo.com; peick@indepthcompressive.com; cmeng@indepthgeo.com.

[2]PETRONAS, Kuala Lumpur, Malaysia. E-mail: lauengchuan@petronas.com; mnasrul_isa@petronas.com.my.

[3]Expand Energy Corporation, Oklahoma City, Oklahoma, USA. E-mail: rika.burr@expandenergy.com; jonathan.woolley@expandenergy.com.

[4]Bright Reflections, Houston, Texas, USA. E-mail: jinming.zhu@chk-nonemp.com.

Downloaded from http://pubs.geoscienceworld.org/seg/tle/article-pdf/45/2/73/7765650/tle-v45-n2.pdf by Shivaji Maitra on 19 February 2026

CS principles retrospectively to perform bin reduction offers a cost-effective path to improving resolution without new acquisition.

This study addresses both gaps through mutual coherence (MC) maps, a quantitative framework for assessing and optimizing sampling geometry. MC maps serve two roles: (1) guiding the design of 2D CS surveys by identifying source/receiver patterns that minimize aliasing energy and (2) evaluating the reconstructability of legacy surveys by measuring their incoherency relative to a sparsity domain. We validate these applications using synthetic SEG Advanced Modeling Corporation Phase II (SEAM II) and field data (including OBN and land surveys) and provide practical recommendations for CS implementation in modern and historical contexts.

Multidimensional CS survey design

The multidimensional CS framework builds upon the compressive seismic acquisition (CSA) design methodology from Jiang et al. (2018), enhancing it through localized windowed processing that addresses key field challenges. Unlike conventional matrix-based approaches, our method operates directly in the sparsity-promoting transform domain within optimized local windows across the survey area. This localized implementation maintains computational efficiency while providing superior aliasing control and explicitly accommodating geologic variations and operational constraints through adaptive sampling design. Examples of such transform-domain methods include Fourier-based reconstruction approaches applied to irregular sampling (Zwartjes and Sacchi, 2007) and the use of sampling functions to analyze aliasing behavior in seismic grids (Naghizadeh and Sacchi, 2010), both of which underscore the importance of working in the transform domain for compressive recovery.

At the core of our method lies the multidimensional MC map calculation, which evaluates local reconstruction quality at every potential source and receiver location. The MC value at position (x, y) is defined as the ratio between the second-largest coefficient and the maximum coefficient in the sparsity-promoting transform domain for a local window around that point. Mathematically, this is expressed as follows:

$$\mathrm{MC}(x,y) = \frac{\max\|U_s^{`}\|}{\max\|U_s\|}, U_s^{`} \in U_s, \quad (1)$$

where U_s represents the coefficients of the multidimensional sampling function in the transform domain (typically Fourier or curvelet) and U_s' contains all coefficients except the dominant one (Jiang et al., 2018). Intuitively, this ratio quantifies the sparsity of the signal in the transform domain: a lower secondary-to-dominant coefficient ratio indicates that the signal energy is concentrated in relatively few components, satisfying the CS requirement and enabling accurate local reconstruction via sparse inversion from limited measurements.

The practical implementation of this method involves three primary stages that form a complete workflow for field applications (see Figure 2). First, the survey area is parameterized by defining a fully sampled target grid that represents the ideal acquisition scenario. This includes specifying the nominal source and receiver spacing in inline and crossline directions, typically based on the minimum desired bin size and Nyquist requirements for the target depth. Second, we perform MC-driven optimization to determine the actual source and receiver locations. This process uses the MC map as an objective function to be minimized, subject to various field constraints. The optimization

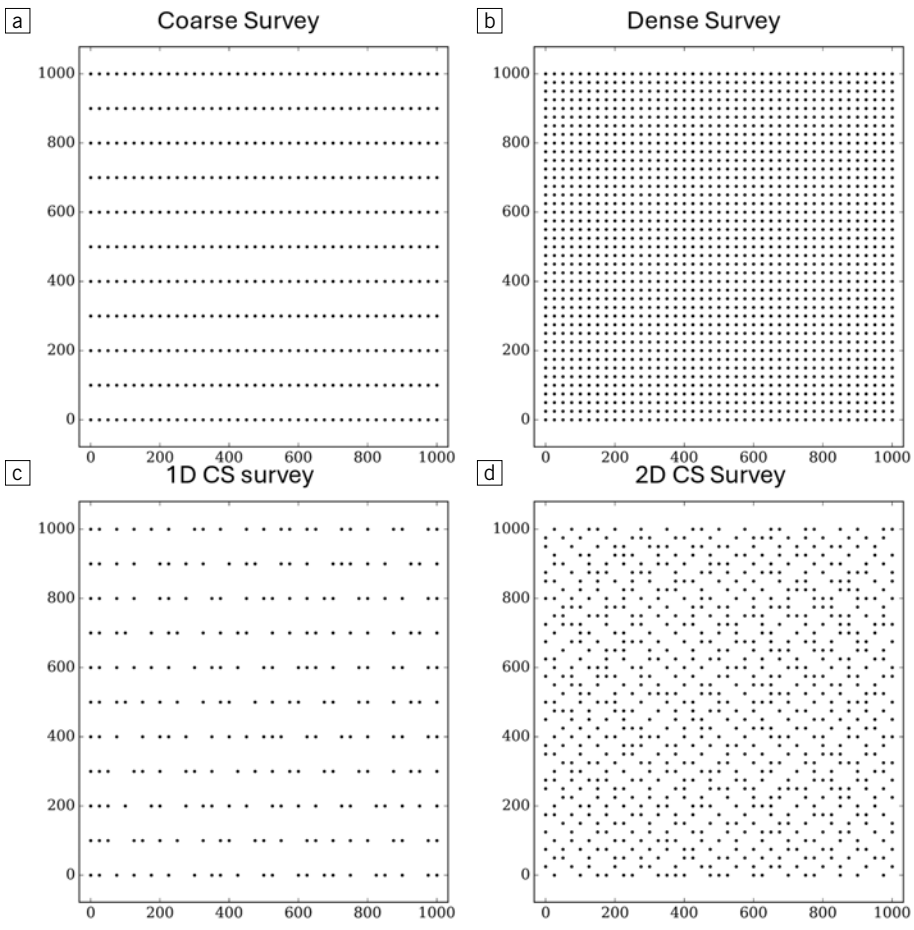

Figure 1. Examples of source or receiver maps: (a) orthogonal coarse survey, (b) dense nodal survey, (c) 1D CS survey derived from (a) with 50% sampling, and (d) 2D CS survey derived from (b) with 50% sampling.

Downloaded from http://pubs.geoscienceworld.org/seg/tle/article-pdf/45/2/73/7765650/tle-v45-n2.pdf by Shivaji Maitra on 19 February 2026

considers not just the overall sampling percentage but also incorporates real-world limitations such as surface obstacles, access restrictions, and equipment availability. The result is an acquisition geometry that provides the best possible reconstruction quality within the given constraints. Finally, the generated MC map serves as a powerful quality control tool. By visualizing the MC values across the survey area, acquisition planners can immediately identify problematic zones that may require additional infill shots or modified receiver placement. The color-coded MC map (with cooler colors indicating better reconstruction potential) provides an intuitive yet quantitative assessment of the design's effectiveness.

Figure 3 compares two CS acquisition designs based on a real survey geometry. Two designs have similar total sampled locations. The left panel shows a 1D CS layout using 25% sampling independently in the inline directions, whereas the right panel demonstrates a 2D CS design with the same sampling ratio. The MC map background highlights reconstructability, with blue regions indicating high-fidelity recovery and red regions showing poor performance. Here, the MC values are computed following Jiang et al. (2018) and serve as a quantitative indicator of how well local sampling patterns support CS reconstruction. The 2D design achieves more uniform and lower MC values across the area, reflecting improved spatial incoherency and reconstruction potential. The obstacles were used as conditions during CS design optimization, and from the related MC maps, we can see that the impact from the large gaps is more severe in the 1D case, as the MC and resulting sparsity are harmed by the large gaps along the 1D east–west axis. In the 2D case, however, this impact can easily be mitigated by the near samples along the orthogonal axis.

SEAM II synthetic test. The Barrett unconventional model in the SEAM II data set is used for the synthetic tests (Regone et al., 2017). The Barrett model is about 10 × 10 × 3.75 km in size with 6.25 m cubic cells. The synthetic data set was generated with orthorhombic anisotropic wave equation modeling, and the data were recorded with 100-m shot line spacings, 25-m station spacings, and 6.25 m × 6.25 m receiver spacings. Because we know the ground truth in the full data set, we can calculate the signal-to-noise ratio (SNR) of reconstruction from different CS sampling with the following equation:

$$\mathrm{SNR(dB)} = 10\log_{10}\left(\|\mathbf{d}_{\mathrm{true}}\|^2 / \|\mathbf{d}_{\mathrm{true}} - \mathbf{d}_{\mathrm{CSR}}\|^2\right) \qquad (2)$$

Previous results (Table 1 and Figure 4) demonstrated a general trend: higher-dimensional CS designs, particularly 2D designs, led to lower MC map values and higher SNRs. This suggests that 2D CS strategies offer improved reconstruction quality compared with traditional 1D approaches. However, no direct correlation was observed between MC values and SNRs across all cases. Although lower MC values often aligned with higher SNRs, some variability indicated that additional factors, such as the specific arrangement of retained receivers, edge effects, or local density, may influence reconstruction quality. To further examine this relationship, a dedicated numerical study was conducted.

In this experiment, a synthetic data set was used as the ground truth, consisting of full shot gathers recorded on a fixed dense receiver grid of 641 × 641 nodes spaced at 12.5 m intervals (see Figure 5). A series of optimized, compressively subsampled receiver layouts were then created using the CS regular-indexed method (Jiang et al., 2018), with 1D and 2D designs at sampling ratios ranging from 10% to 90%. Importantly, the source geometry was held constant, allowing the analysis to isolate the effects of receiver-side compressive acquisition.

Each subsampled receiver geometry was CS-reconstructed (CSR) onto a regular grid using the extended projection onto convex sets (EPOCS) algorithm (Jiang et al., 2017) and then compared with the full data set to calculate the SNR. In parallel, MC maps were computed based on each acquisition layout to assess theoretical reconstructability (Jiang et al., 2018). By analyzing SNR and MC values across the range of CS designs and sampling ratios, this study aims to quantify how MC maps predict practical reconstruction outcomes.

Figure 6–8 provide a visual comparison of the MC map distributions and reconstruction differences for CS 1D and CS 2D designs across a wide range of sampling ratios (10%–90%). Figure 6 presents the MC maps computed for each sampling level using the regular-indexed CS-A (CSA-RI) method. The 2D CS designs consistently yield lower MC values than their 1D counterparts, indicating stronger reconstruction potential. Figure 7 shows the absolute differences between the full data set (Figure 5b) and

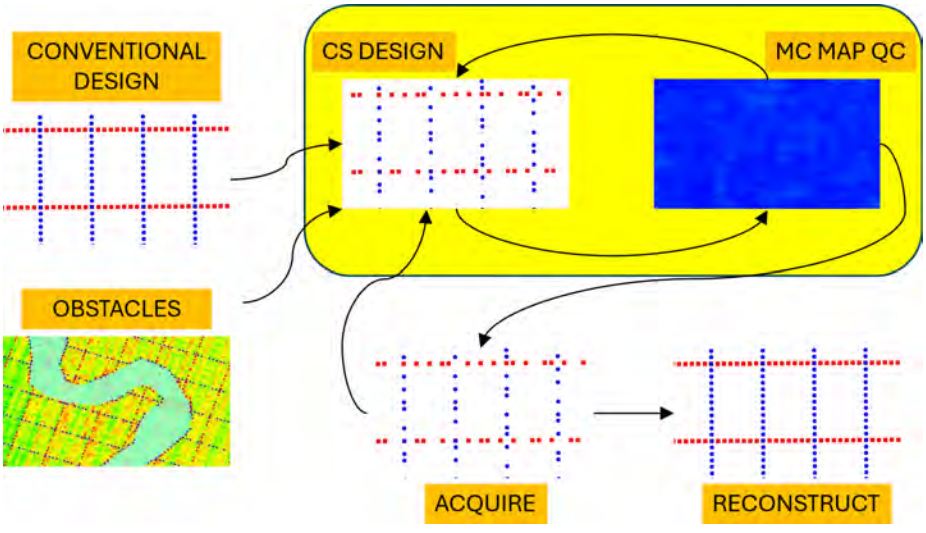

Figure 2. Example of a practical CSA survey design workflow.

Downloaded from http://pubs.geoscienceworld.org/seg/tle/article-pdf/45/2/73/7765650/tle-v45-n2.pdf by Shivaji Maitra on 19 February 2026

reconstructions from CS 1D sampling, and Figure 8 shows the same for CS 2D sampling. As the sampling ratio increases, differences decrease in both cases; however, CS 2D clearly maintains better fidelity across all levels, with notably lower residuals even at aggressive undersampling. These figures illustrate the qualitative benefits of 2D CS design in preserving signal continuity and reducing reconstruction artifacts.

The results summarized in Table 2 and illustrated in Figure 9 reveal several important trends. First, 2D CS designs consistently produce lower MC map values and higher reconstruction SNRs than their 1D counterparts across all sampling ratios. As shown in Figure 9a, MC values decrease with increasing sampling density for both designs, but the decline is slower for 2D CS. Figure 9b demonstrates a general inverse relationship between MC values and SNRs. This reflects the underlying principle that MC, which quantifies the worst-case correlation between sampling and sparsity bases, can serve as a useful objective function for CS performance. Lower MC map values correspond to higher incoherence and thus better reconstruction quality. Although the practical relevance of MC has been debated in some contexts, these results provide empirical support for its continued utility in CS survey design. Figure 9c highlights the practical benefit: for a given SNR, 2D CS designs require approximately 20% fewer samples than 1D designs, or alternatively, they offer a higher SNR of around 5 dB at the same sampling level. These results underscore the efficiency and robustness of 2D CS acquisition strategies, particularly for modern surveys with dense, multidirectional sampling requirements.

Validation on the SEAM II data set demonstrates the method's effectiveness, showing that 2D CS designs achieve a higher SNR of 5 dB than 1D approaches at equivalent sampling or can reduce source/receiver requirements by 20% for comparable results.

Table 1. MC map statistics and CS-R SNR for test 1, where all cases sample 50% in each axis and keep 25% traces (Jiang et al., 2019).

CS sampling designs	1D CS in *x*,*y* (no gap control)	1D CS in *x*,*y* (with gap control)	1D CS in *x*; 1D CS in each *y*-line	2D CS
Mean MC map	0.282	0.317	0.305	0.121
Minimum MC map	0.181	0.223	0.209	0.079
CS-Recon SNR (dB)	18.56	24.23	24.74	27.58

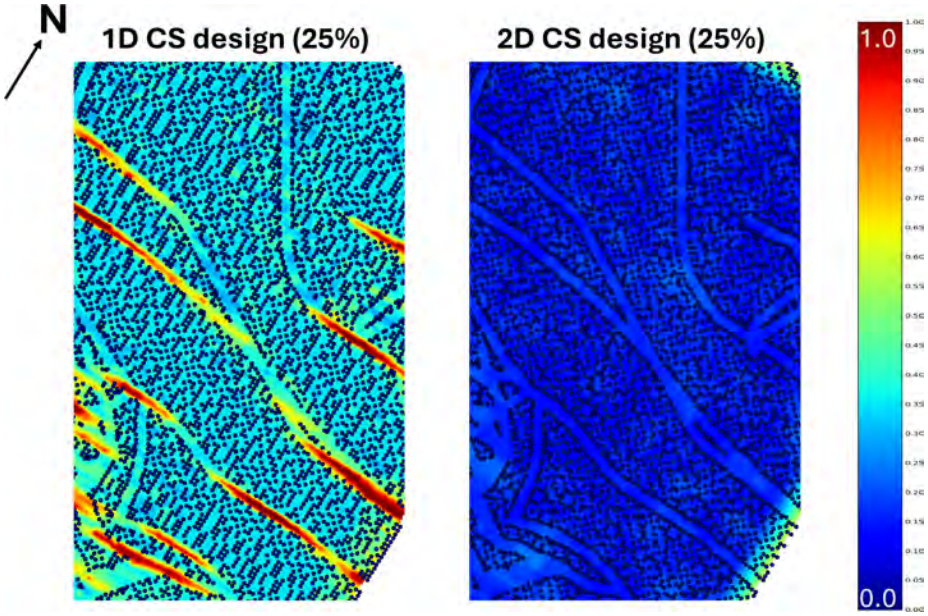

Figure 3. Comparison of CSA strategies on a real survey geometry. The inline (IL) direction is NW–SE (upper-left to lower-right). The left panel shows a 1D CS design with 25% sampling applied independently along IL. The right panel shows a 2D CS design with 25% sampling jointly optimized across both dimensions. Background color denotes the MC map values: blue (0.0) indicates the highest reconstructability (minimal aliasing energy), and red (1.0) indicates the lowest reconstructability.

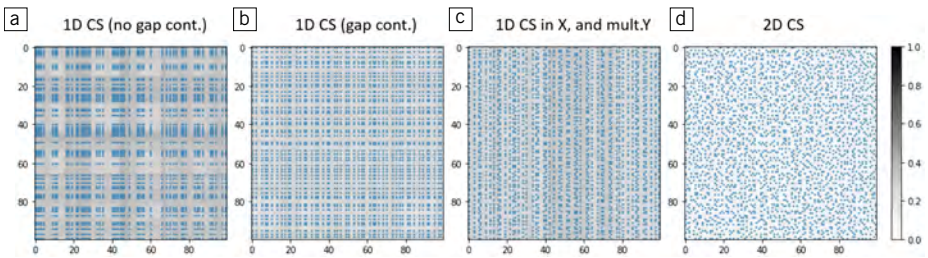

Figure 4. CS sampling overlaying on the MC map for designs with different dimensions. Gray color represents the MC value in the MC map (Jiang et al., 2019).

OBN data test. During 2024, a CS test project was carried out in collaboration with PETRONAS, involving a 3D four-component (4C) OBN survey acquired offshore Sabah, Malaysia. The survey covered approximately 170 km^2. Among the various test scenarios, two cases are of particular interest: CS subsampling and reconstruction applied to sources and to receivers. The general workflow involved applying an optimized CS sampling design to the fully acquired field data, followed by data reconstruction using the EPOCS algorithm (or other CS reconstruction methods), and subsequent comparison with the original full data set. This type of evaluation, commonly performed on existing data sets to assess the effectiveness of CS acquisition and reconstruction in a specific geologic setting, will hereafter be referred to as a "drop-and-recon" test.

The first test is a shot "drop-and-recon" experiment performed on node gathers, where the input data had already undergone regular grid shot reconstruction. Two CS shot-sampling strategies were evaluated at

Downloaded from http://pubs.geoscienceworld.org/seg/tle/article-pdf/45/2/73/7765650/tle-v45-n2.pdf by Shivaji Maitra on 19 February 2026

a 75% shot reduction level (i.e., 25% retained): an optimized 2D CS design and a production-feasible 1D CS design. In the 1D case, CS sampling was applied only to line spacing, and shots were retained on alternating stations (even or odd) to mimic a realistic flip-flop shooting pattern, a common operational constraint in the field.

Figure 10 illustrates the MC map distributions (a-d) and zoomed-in shot maps (e-h) for four acquisition scenarios: (a, e) full data, (b, f) legacy field sampling, (c, g) optimized 2D CS design, and (d, h) 1D CS design. The MC maps reveal that the 2D CS layout (c) achieves the lowest MC values, indicating its stronger potential for accurate reconstruction. The 1D CS design (d) shows elevated MC values due to its constrained geometry but still performs significantly better than the legacy CS sampling (b), which shows significant unevenness in the MC map. Visually, the 2D CS layout (g) demonstrates a more uniform and randomized distribution of shot points compared with the 1D CS layout (h), which in turn is more optimized than the legacy pattern (f). From an acquisition perspective, the 2D CS design may further reduce the number of shots or receivers required, offering larger potential cost savings. However, its implementation is more complex and may not be appropriate for all surveys. The 1D CS layout represents a practical compromise, improving reconstruction over legacy sampling while maintaining simple field logistics. These results underscore the trade-off between optimal CS design for reconstruction and the practical considerations of acquisition speed and cost.

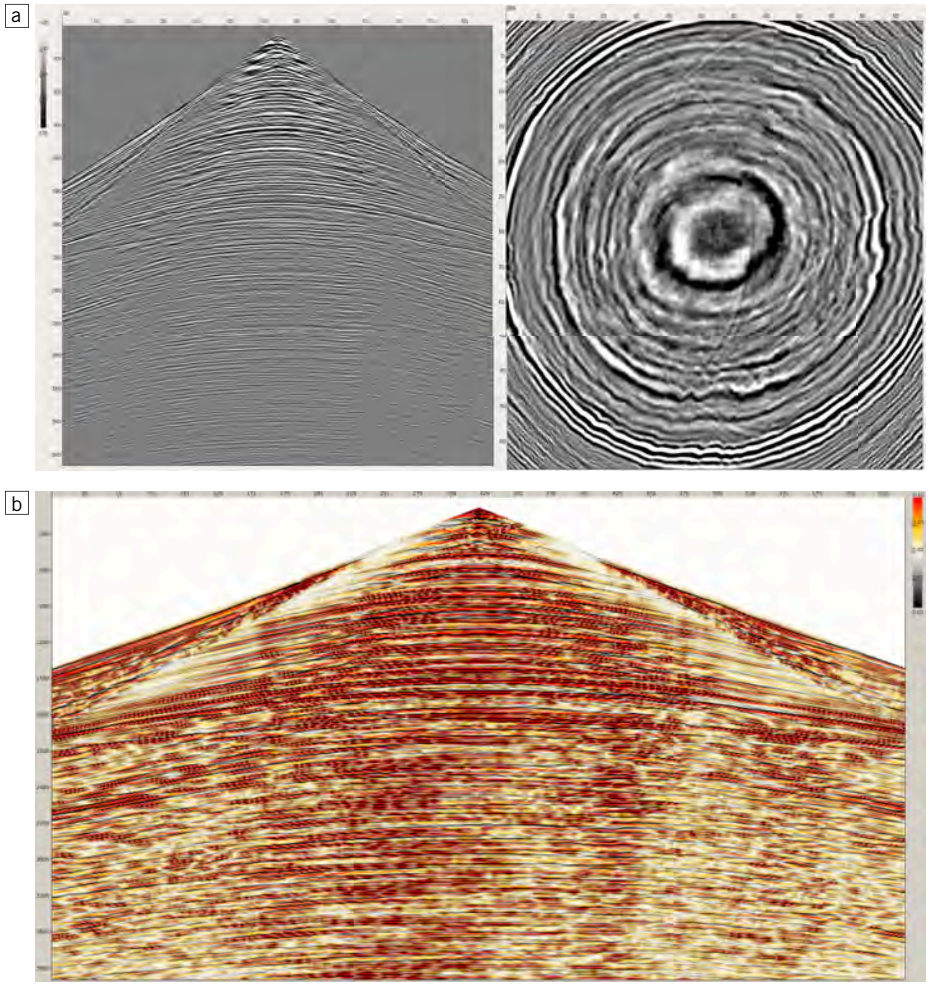

Figure 5. (a) SEAM II data set shot gather example: 641 × 641 receivers on a 12.5 m × 12.5 m grid. Left: inline view (641 × 4 Sec traces). Right: time slice (641 × 641). (b) SEAM II data set full data set used in the CS 1D and CS 2D sampling test. Display scaling uses T-power gain = 1 and amplitude scale = 5 for visibility.

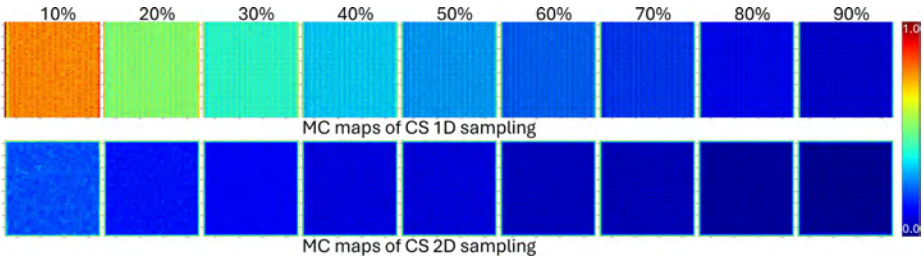

Figure 6. MC maps of CS 1D and CS 2D sampling, from 10% to 90% sampling by the CSA-RI method. Cooler colors represent low MC values, indicating better reconstruction potential.

In contrast to the theoretical MC assessment, Figure 11 provides a practical view by showing reconstruction differences between the full data set and the CSR. Although both CS approaches approximate the full data well, residuals from the 2D CS design exhibit less coherent structure and lower overall energy. This suggests that the 2D layout more effectively preserves primary seismic signals and suppresses aliasing, especially in complex wavefields. The 1D design, although operationally convenient, shows slightly more structured leakage, underscoring the balance between field feasibility and optimality.

Further insight is provided by the amplitude spectra in Figure 12. Both CS reconstructions closely follow the spectral profile of the full data set, but the 2D CS result better retains high-frequency components, reflecting improved fidelity in finer-scale features. This spectral advantage highlights the benefit of increased spatial incoherence in 2D CS, which helps preserve broader bandwidths during reconstruction.

Downloaded from http://pubs.geoscienceworld.org/seg/tle/article-pdf/45/2/73/7765650/tle-v45-n2.pdf by Shivaji Maitra on 19 February 2026

Together, these results highlight a critical trade-off: 2D CS designs offer superior reconstruction quality, but 1D CS layouts remain a practical and significantly improved alternative to legacy field practices, especially in production scenarios where geometric flexibility is limited.

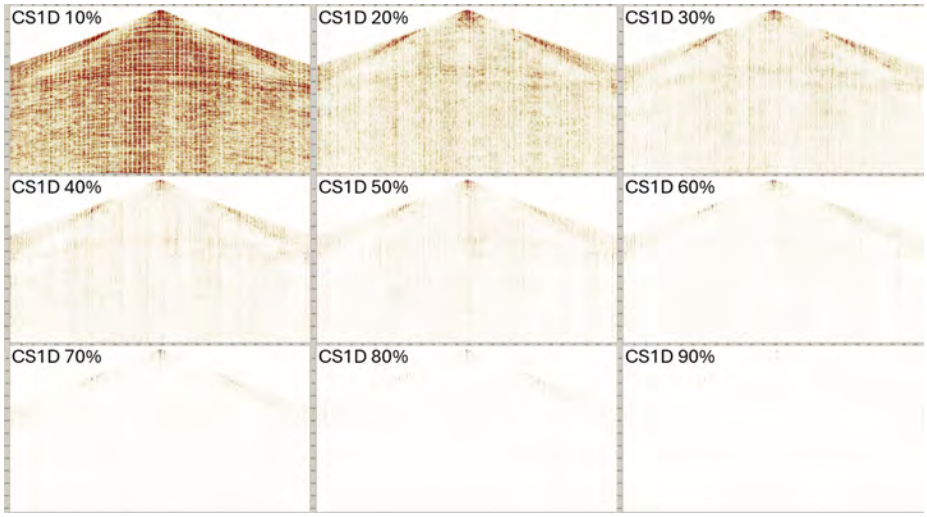

Figure 7. Differences between the full data set and reconstructed results using CS 1D sampling at various ratios from 10% to 90%. Lower differences indicate better reconstruction quality. Display scaling uses T-power gain = 1 and amplitude scale = 5 for visibility.

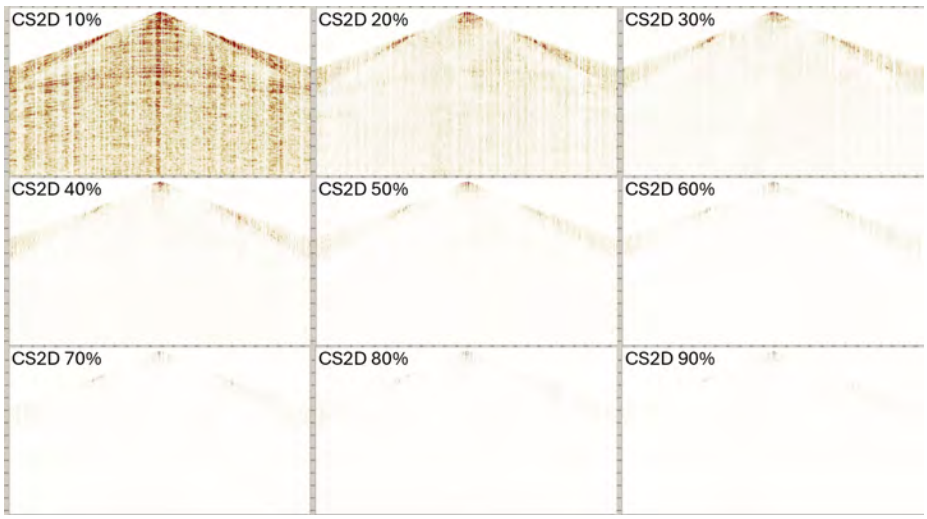

Figure 8. Differences between the full data set and reconstructed results using CS 2D sampling at various ratios from 10% to 90%. Lower differences indicate better reconstruction quality. Display scaling uses T-power gain = 1 and amplitude scale = 5 for visibility.

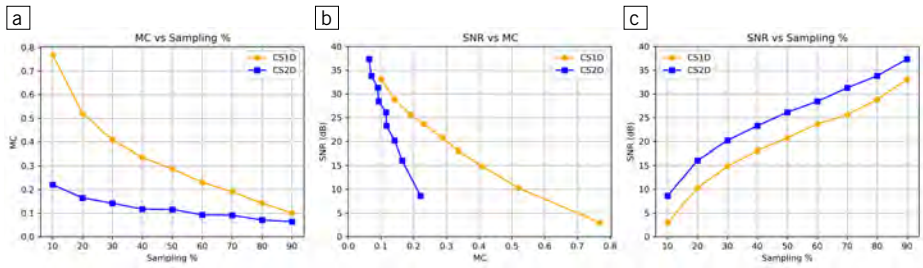

Figure 9. Evaluation of CS performance at different sampling levels. (a) MC map values decrease as sampling increases, indicating more favorable conditions for CS reconstruction with higher sampling percentage. (b) The SNR improves as MC map values decrease, reflecting better reconstruction quality with higher incoherence. (c) The SNR increases with increasing sampling percentage, illustrating the effectiveness of CS in sparse recovery. Results are shown for 1D (orange) and 2D (blue) CS implementations.

The second test is a node "drop-and-recon" experiment, aiming to show the possibility of skipping nodes in an OBN survey, which has a significant impact on the acquisition cost. In this test, two 2D CS node sampling strategies were applied at 70% and 50% node retention, respectively, using optimized CS designs. The raw node gathers were reconstructed to a regular grid using the EPOCS algorithm, followed by stacking without any additional denoising, deconvolution, or regularization. Figure 13 shows the node sampling and related MC maps from different CS sampling strategies, namely, 2D CS sampling with 70% or 50% nodes. As expected, higher sampling leads to lower MC map values and theoretically higher SNRs from CSR. The relatively low SNR values observed, approximately 15 dB for 70% node sampling and 12 dB for 50%, are below the idealized curve established earlier between the sampling ratio and SNR. However, this reduction in the SNR is expected due to the use of raw input data and the absence of noise attenuation or signal enhancement processes typically applied before reconstruction. Additionally, the node spacing in this field is 150 m, which poses a considerable challenge for sparse acquisition and reconstruction, further contributing to the lower SNR. Nevertheless, as shown in Figure 14, the reconstructed stacks closely resemble the full-data stack in overall structure and continuity, especially in the 70% case. The amplitude spectra comparison in Figure 15 also demonstrates that the 2D CS reconstruction maintains high-frequency content more effectively at higher sampling levels, reinforcing the value of optimized CS design even under field-imposed limitations.

In summary, the multidimensional CS framework builds on theoretical principles of MC to optimize sampling in inline and crossline directions, effectively reducing aliasing and improving

Downloaded from http://pubs.geoscienceworld.org/seg/tle/article-pdf/45/2/73/7765650/tle-v45-n2.pdf by Shivaji Maitra on 19 February 2026

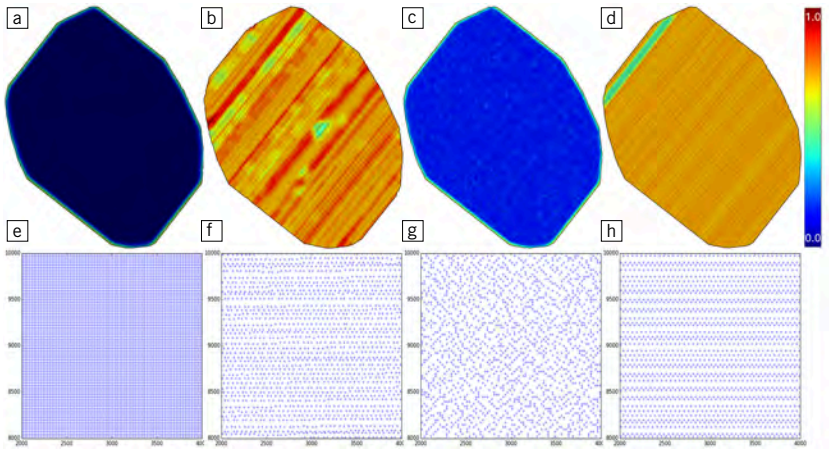

Figure 10. MC maps (a-d) and corresponding zoom-in views of shot point distributions (e-h) for various acquisition strategies. (a, e) Full data set, (b, f) legacy CS field sampling, (c, g) optimized 2D CSA design with 25% sampling, and (d, h) 1D CSA design with 50% line and 50% station sampling. MC map values range from 0.0 (best) to 1.0 (worst).

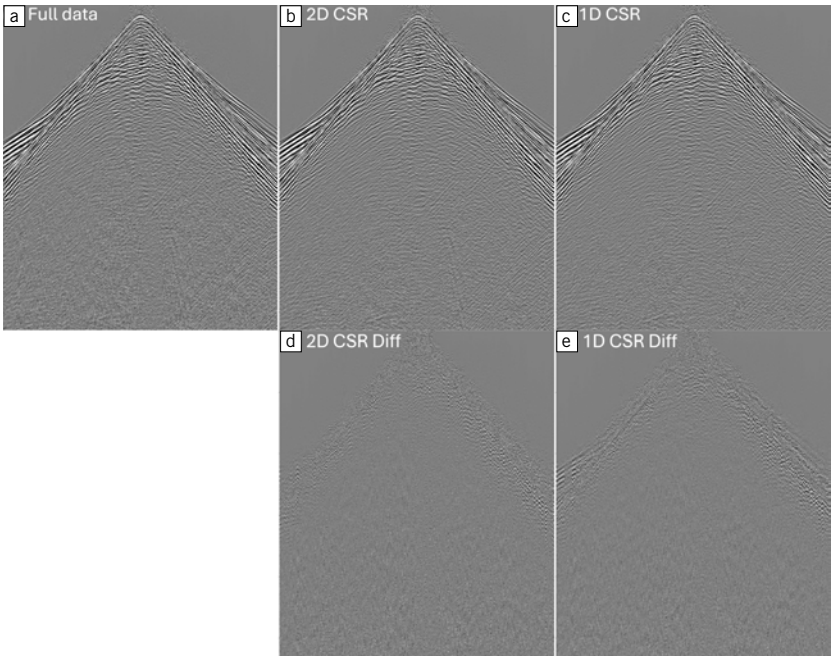

Figure 11. Reconstruction differences resulting from various CS sampling strategies. (a) Full data set for reference. (b) EPOCS reconstruction using 2D CS sampling with 25% shots (2D CSR). (c) EPOCS reconstruction using 1D CS sampling with 50% lines × 50% stations (1D CSR). (d) Difference between the full data set and 2D CSR. (e) Difference between the full data set and 1D CSR. Lower differences indicate better reconstruction fidelity. The display area spans 650 traces more than 10.5 s. T-power gain = 1 and scale = 2 for visibility. OBN Data courtesy of PETRONAS.

Table 2. MC map statistics and CS-R SNR for 1D CS and 2D CS sampling from 10% to 90%.

Sampling %	10%	20%	30%	40%	50%	60%	70%	80%	90%
CS1D MC	0.769	0.521	0.409	0.336	0.288	0.231	0.191	0.142	0.101
CS1D SNR (dB)	2.96	10.29	14.87	18.07	20.75	23.62	25.62	28.81	33.07
CS2D MC	0.221	0.165	0.142	0.117	0.116	0.093	0.091	0.071	0.064
CS2D SNR (dB)	8.63	16.07	20.2	23.27	26.13	28.41	31.28	33.8	37.34

reconstruction quality. Validation with the SEAM II synthetic data set demonstrated that 2D CS designs consistently outperform 1D approaches by achieving lower MC and higher SNRs across various sampling levels. These findings were further confirmed in real-world OBN surveys, where 2D CS layouts provided superior reconstruction fidelity and spectral preservation compared with legacy and 1D sampling strategies, highlighting the practical benefits of multidimensional CS for modern seismic acquisition.

Legacy data bin reduction

The drive for higher resolution seismic imaging often conflicts with the reality of legacy data sets acquired using coarser spatial sampling. Traditional approaches to address this limitation relied on regular decimation and deterministic interpolation, methods fundamentally flawed in their assumption that seismic data can be perfectly reconstructed through mathematical smoothness alone. These techniques routinely fail to distinguish between true geologic content and interpolation artifacts, either oversmoothing subtle stratigraphic features or introducing false discontinuities. The CSA based on the MC map framework provides a physics-based alternative by quantifying exactly how much information the existing acquisition geometry can theoretically deliver about a denser target grid.

At the core of this approach lies a rigorous evaluation of how

Downloaded from http://pubs.geoscienceworld.org/seg/tle/article-pdf/45/2/73/7765650/tle-v45-n2.pdf by Shivaji Maitra on 19 February 2026

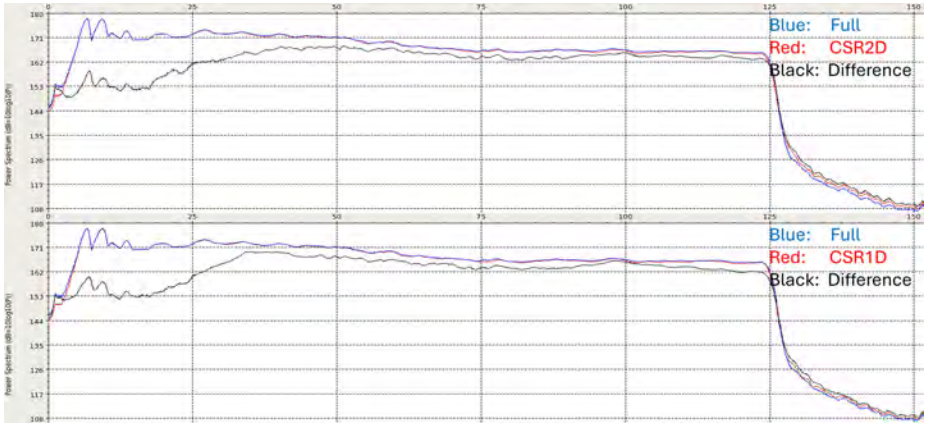

Figure 12. Amplitude spectra comparison from the shot "drop-and-recon" test. In each panel, three curves are shown: (1) full data set, (2) CS reconstruction (2D CS sampling with 25% shot sampling in the top panel and 1D CS sampling with 50% lines × 50% stations in the bottom panel), and (3) the difference between the full data set and the reconstruction.

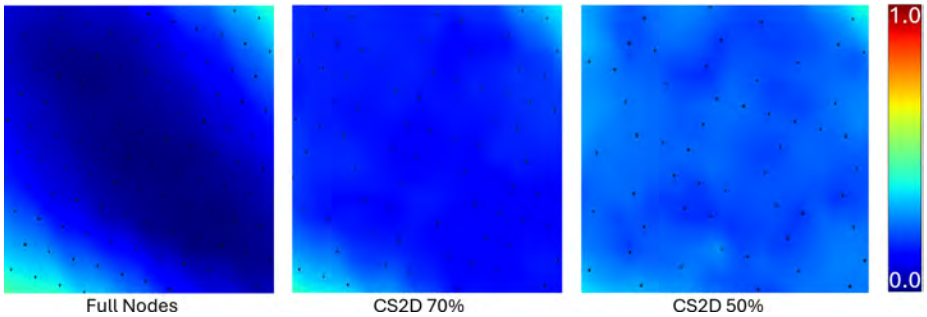

Figure 13. Node sampling layouts for three acquisition scenarios: full data (left), 2D CS design with 70% sampling (middle), and 2D CS design with 50% sampling (right). Background color represents the corresponding MC map, with lower values indicating better theoretical reconstructability.

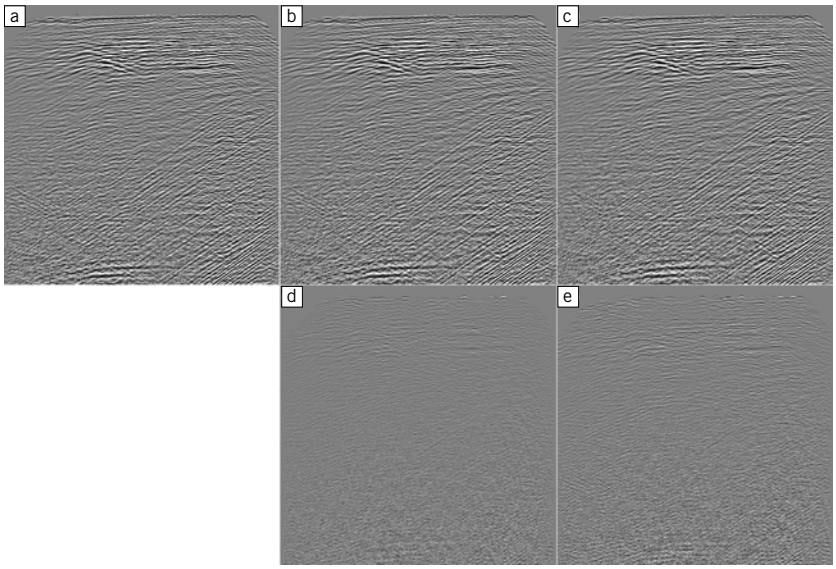

Figure 14. Comparison of raw stack sections from CSR applied to node-sampled OBN data. (a) Full data set stack (reference). (b) EPOCS reconstruction using 2D CS sampling of 70% nodes (CSR 70%). (c) EPOCS reconstruction using 2D CS sampling of 50% nodes (CSR 50%). (d) Difference between the full data set and CSR 70%. (e) Difference between the full data set and CSR 50%. The display area spans 500 traces over 10.5 s. T-power gain = 1 and scale = 2 for visibility. OBN data courtesy of PETRONAS.

irregular field sampling interacts with the desired reconstruction grid. Unlike theoretical analyses that assume ideal random sampling, the method begins by precisely mapping each physical source and receiver position from the original navigation data onto the target finer grid. This spatial registration honors the true acquisition geometry with all its operational imperfections, from source skids to receiver dropouts, which often serendipitously create favorable conditions for compressive reconstruction. The subsequent MC map calculation evaluates this mapping through localized analysis windows, generating a spatial map that distinguishes zones of high reconstructability (where the existing sampling provides sufficient independent information) from areas where the original acquisition proves too sparse or too regular for meaningful resolution enhancement.

Implementation proceeds through four systematic stages. First, the precise source and receiver coordinates are extracted from navigation files or SEG-Y headers, with particular attention to positional accuracy, which proves critical for reliable MC computation. Second, these irregularly sampled locations are mapped onto the desired denser grid through a Voronoi tessellation approach that preserves local sampling characteristics. Third, the MC values are calculated within sliding windows of practical size (typically 500 m × 500 m for land surveys), generating a spatial map of reconstruction potential. Finally, zones meeting an empirical threshold of MC <0.5 are flagged for sparse inversion processing.

The reconstruction uses an adapted EPOCS algorithm (Jiang et al., 2017) that dynamically adjusts its constraints based on local MC values, creating a spatially varying regularization scheme that represents a significant advancement over

Downloaded from http://pubs.geoscienceworld.org/seg/tle/article-pdf/45/2/73/7765650/tle-v45-n2.pdf by Shivaji Maitra on 19 February 2026

uniform approaches. In zones with favorable MC values below 0.4, the algorithm applies lighter transform-domain constraints to maximize resolution recovery, whereas the areas of marginal coherence (0.4–0.5) receive stronger regularization to maintain amplitude fidelity and prevent artifacts. The iterative process simultaneously enforces three key physical constraints: measurement consistency with the original traces through data fidelity terms, geologic plausibility via transform-domain sparsity promotion, and structural continuity using directional regularization operators. This physics-based approach fundamentally differs from conventional bin-interpolation methods by explicitly incorporating the actual wavefield sampling characteristics through the MC guidance, rather than relying on mathematical smoothness assumptions that often generate unrealistic results. The adaptive parameterization ensures optimal trade-offs between resolution enhancement and artifact suppression across different regions of the survey based on their inherent reconstructability.

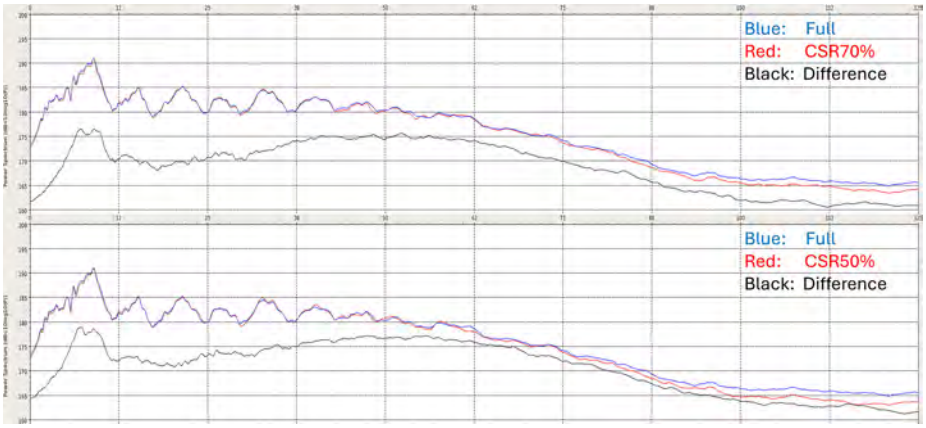

Figure 15. Amplitude spectra comparison from the node "drop-and-recon" test. Each panel shows three curves: (1) full data set, (2) CS reconstruction (top panel: 2D CS sampling with 70% nodes; bottom panel: 2D CS sampling with 50% nodes), and (3) the difference between the full data set and the reconstruction.

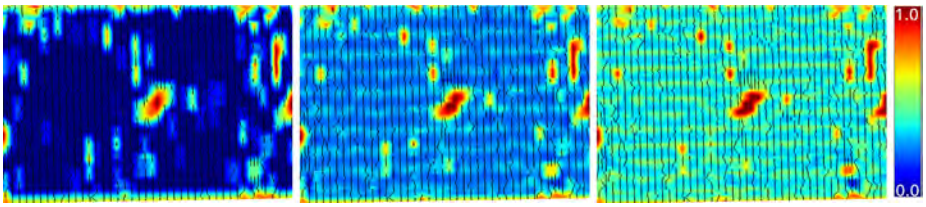

Figure 16. MC maps for different bin-reduction scenarios on a field data set with original receiver spacing of 165 ft. The three panels from left to right show MC maps for bin sizes of 165 ft (100% original), 125 ft (approximately 75%), and 100 ft (approximately 60%), respectively. Lower MC values indicate higher potential for accurate reconstruction.

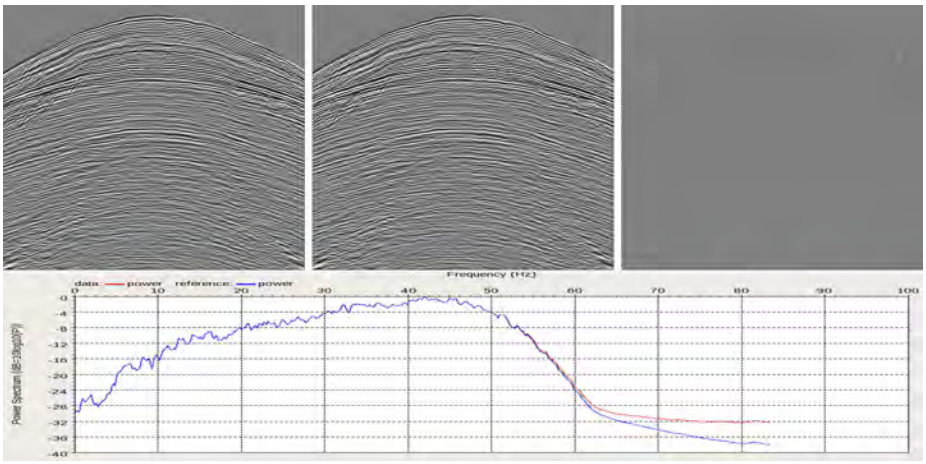

Figure 17. SEAM II synthetic test for bin-reduction validation. Top panel (left to right): reference gather at 18.75 m spacing, gather from 25 m data set after bin reduction to 18.75 m, and the difference between them. Bottom panel: amplitude spectrum comparison between the reference 18.75 m data and the bin-reduction result. *T*-pow gain = 1 and scale = 2 for visibility.

To validate the proposed bin-reduction method guided by the MC map, a series of tests were conducted on synthetic and field data sets.

First, MC maps were computed for reconstruction grids at different target bin sizes: 100%, 75%, and 60% of the original bin dimensions (Figure 16). As expected, smaller bin sizes (denser grids) resulted in increased MC values, indicating higher aliasing risk. The 75% bin size, however, maintained MC values below critical thresholds, suggesting that it provides a good balance between improved resolution and reconstruction stability.

Next, the method was evaluated on the SEAM II synthetic data set, which features a dense receiver spacing of 6.25 m. A 25-m sampling grid was bin-reduced to 18.75 m (75%) using the MC-guided CSR (Figure 17). The reconstructed gathers showed strong agreement with the full 18.75-m data set, confirming the method's ability to accurately recover fine-resolution data when MC values remain acceptable.

Finally, a real-world land case study tested the approach on legacy data acquired with 110 ft bins. The data set represents a depth image reprocessing project that merges nine legacy surveys across a total area of 1800 square miles. The CS-based reconstruction reduced the bin size to 82.5 ft (approximately 75%) without requiring new acquisition effort. The MC map confirmed that the original geometry provided sufficient incoherence to support sparse recovery.

The reconstructed volumes exhibit significant improvements in

Downloaded from http://pubs.geoscienceworld.org/seg/tle/article-pdf/45/2/73/7765650/tle-v45-n2.pdf by Shivaji Maitra on 19 February 2026

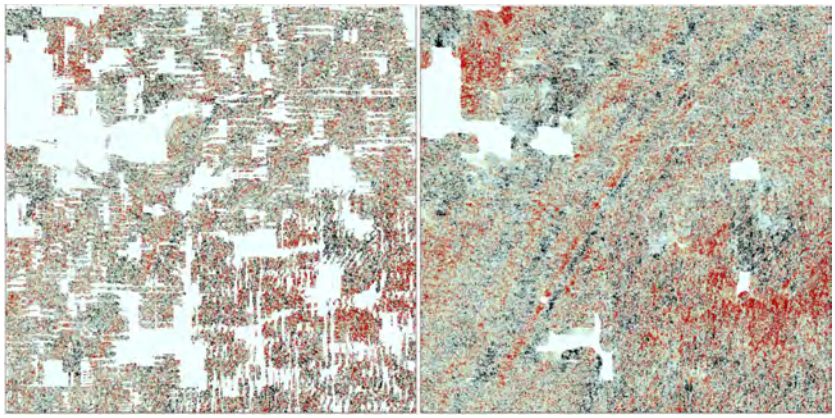

Figure 18. Offset vector tile (OVT) binned cube comparison: left: time slice from natural binning (110 ft); right: same views after 70% bin reduction via CSR (82.5 ft). The example area is approximately 40 k × 40 k ft. Seismic data owned or controlled by Seismic Exchange, Inc.; interpretation is that of Expand Energy Corporation.

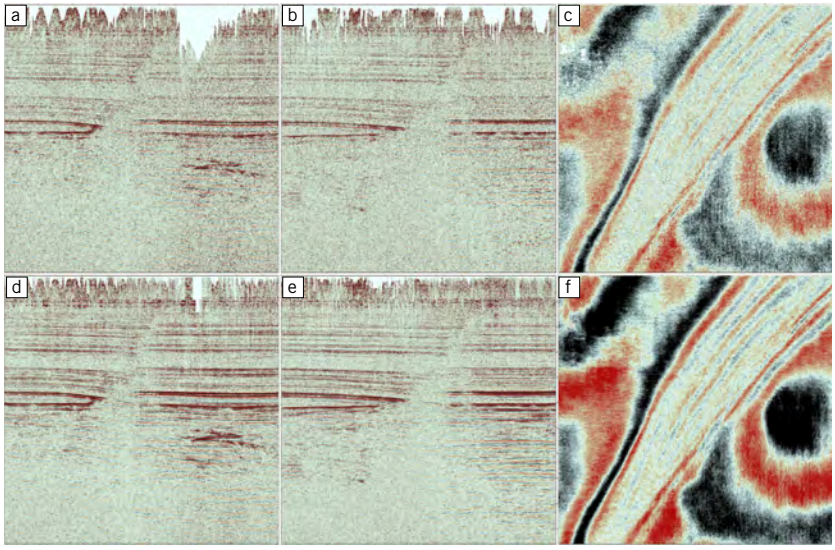

Figure 19. Offset vector tile (OVT) stack comparison: (a-c) inline, crossline, and time slice (2.2 s) from natural binning (110 ft) and (d-f) same views after 75% bin reduction via CSR (82.5 ft). The example area is approximately 40 k × 40 k ft × 5 s. Seismic data owned or controlled by Seismic Exchange, Inc.; interpretation is that of Expand Energy Corporation.

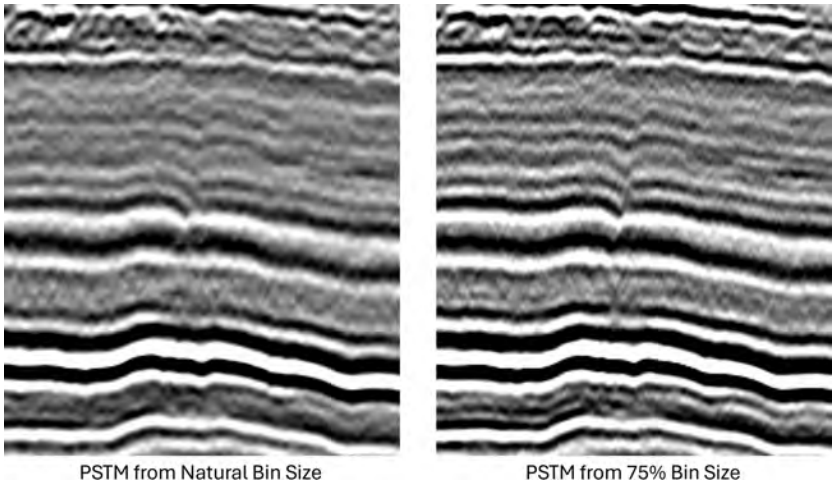

Figure 20. Prestack time migration (PSTM) stack from natural bin and 75% bin reduction by CSR. Seismic data owned or controlled by Seismic Exchange, Inc.; interpretation is that of Expand Energy Corporation.

imaging quality (Figures 18 and 19). Faults and discontinuities are more sharply resolved in inline and crossline directions. Time slices show improved lateral continuity of reflectors, particularly in complex structural areas. These improvements were achieved without the over-smoothed character or artificial continuity often introduced by conventional interpolation.

Unlike deterministic interpolation that assumes spatial smoothness, the CS approach adapts regularization strength based on local MC values, preserving geologic realism and amplitude integrity. Figure 20 shows that the prestack time migration (PSTM) stack of the reduced-bin volume maintains structural consistency and stratigraphic detail, demonstrating the robustness of the MC-guided CS reconstruction.

Together, these results confirm that the MC map provides a practical, physics-informed metric for guiding safe bin reduction. On SEAM II data, the reduced-bin reconstructions closely match higher-resolution ground truth. On field data, reducing bin size from 110 ft to 82.5 ft improved fault visibility without artifacts. By leveraging the natural irregularity in legacy data sets, this method achieves meaningful resolution enhancement without costly re-acquisition, making it a valuable tool for modern reprocessing workflows.

Conclusions

This study presents two complementary applications of CS in seismic acquisition and reprocessing, both leveraging the MC map as a central tool. Although distinct in scope, forward-looking survey design versus retrospective bin-reduction, the MC map provides a consistent framework for evaluating and improving sampling efficiency and reconstruction quality.

For new surveys, we introduced a multidimensional CS design

Downloaded from http://pubs.geoscienceworld.org/seg/tle/article-pdf/45/2/73/7765650/tle-v45-n2.pdf by Shivaji Maitra on 19 February 2026

methodology that uses 2D MC maps to optimize source and receiver geometry in inline and crossline directions. This approach was validated using synthetic data from the SEAM II model and real-world OBN acquisition. Results demonstrate that 2D CS designs provide superior reconstruction fidelity over traditional 1D designs, achieving higher SNRs and reducing acquisition requirements by up to 20% without sacrificing image quality.

In the context of legacy data, the MC map was applied to evaluate reconstructability and guide bin reduction to denser imaging grids. Through tests on synthetic and field data, we showed that reducing bin size to approximately 75% of the original spacing often achieves a favorable trade-off between resolution enhancement and reconstruction stability. Unlike traditional interpolation methods, this approach accounts for actual acquisition geometry and inherent sampling irregularity, ensuring realistic and physically consistent results.

Together, these findings underscore the versatility and value of the MC map as a diagnostic and design tool. Whether used to plan future surveys or to extract more value from existing data, it enables data-driven decisions that enhance seismic resolution, reduce costs, and increase confidence in reconstruction outcomes. This dual-role capability positions MC-guided CS methods as practical solutions for modern acquisition strategies and cost-effective legacy data enhancement. TLE

Acknowledgments

The authors would like to thank their colleagues for valuable discussions and insights and management for their support throughout this work. Special thanks go to PETRONAS, Expand Energy, and Seismic Exchange, Inc. for providing field data sets essential to the validation and application of the proposed methods.

Data and materials availability

Data associated with this research are confidential and cannot be released.

Corresponding author: taojiang@indepthgeo.com

References

Candès, E. J., 2006, Compressive sampling, International Congress of Mathematics: Madrid, Spain, 3, 1455–1452.

Candes, E. J., J. Romberg, and T. Tao, 2006, Robust uncertainty principles: Exact signal reconstruction from highly incomplete frequency information: IEEE Transactions on Information Theory, **52**, no. 2, 489–509, https://doi.org/10.1109/TIT.2005.862083.

Donoho, D. L., 2006, Compressed sensing: IEEE Transactions on Information Theory, **52**, no. 4, 1289–1306, https://doi.org/10.1109/TIT.2006.871582.

Donoho, D. L., and M. Elad, 2003, Optimally sparse representation in general (nonorthogonal) dictionaries via ℓ^1 minimization: Proceedings of the National Academy of Sciences, **100**, no. 5, 2197–2202, https://doi.org/10.1073/pnas.0437847100.

Hennenfent, G., and F. J. Herrmann, 2008, Simply denoise: Wavefield reconstruction via jittered undersampling: Geophysics, **73**, no. 3, V19–V28, https://doi.org/10.1190/1.2841038.

Herrmann, F. J., 2010, Randomized sampling and sparsity: Getting more information from fewer samples: Geophysics, **75**, no. 6, WB173–WB187, https://doi.org/10.1190/1.3506147.

Jiang, T., P. Eick, Y. Jiang, B. Gong, J. Tan, T. Li, K. Koster, et al, 2019, SEAM phase II Barrett model classic data study: Land compressive seismic acquisition: SEG Technical Program Expanded Abstracts, 137–141, https://doi.org/10.1190/segam2019-3215220.1.

Jiang, T., B. Gong, F. Qiao, Y. Jiang, A. Chen, D. Hren, and Z. Meng, 2017, Compressive seismic reconstruction with extended POCS for arbitrary irregular acquisition: SEG Technical Program Expanded Abstracts, 4272–4277, https://doi.org/10.1190/segam2017-17632472.1.

Jiang, T., Y. Jiang, D. Clark, and R. Gray, 2018, SEAM phase II Barrett model classic data study: Land compressive seismic acquisition: SEG Technical Program Expanded Abstracts, 86–90, https://doi.org/10.1190/segam2018-2997088.1.

Lewis, A., T. Mackay, J. Latchman, and T. Jiang, 2024: An assessment of compressive seismic reconstruction in the Delaware Basin, Lea County, New Mexico, SEG Technical Program Expanded Abstracts, 243–247, https://doi.org/10.1190/image2024-4094814.1.

Li, T., J. Tan, W. Chu, T. Jiang, Y. Jiang, P. Eick, K. Woller, et al, 2021, Permian Basin processing and handling shallow anomalies and permit holes: A compressive seismic acquisition and reconstruction case study: SEG Technical Program Expanded Abstracts, 69–73, https://doi.org/10.1190/segam2021-3582910.1.

Naghizadeh, M., and M. D. Sacchi, 2010, On sampling functions and Fourier reconstruction methods: Geophysics, **75**, no. 6, WB137–WB151, https://doi.org/10.1190/1.3503577.

Regone, C., J. Stefani, P. Wang, C. Gerea, G. Gonzalez, and M. Oristaglio, 2017, Geologic model building in SEAM Phase II — Land seismic challenges: The Leading Edge, **36**, no. 9, 738–749, https://doi.org/10.1190/tle36090738.1.

Zwartjes, P. M., and M. D. Sacchi, 2007, Fourier reconstruction of nonuniformly sampled, aliased seismic data: Geophysics, **72**, no. 1, V21–V32, https://doi.org/10.1190/1.2399442.

Downloaded from http://pubs.geoscienceworld.org/seg/tle/article-pdf/45/2/73/7765650/tle-v45-n2.pdf by Shivaji Maitra on 19 February 2026

Unlocking the potential of blended acquisition with independent simultaneous sourcing and dispersed source array onshore Abu Dhabi

Tomohide Ishiyama[1,2] and Afra Aljaberi[2]

https://doi.org/10.1190/tle-2025-1002

Abstract

The first 3D pilot program was acquired and processed using blended acquisition technology, featuring independent simultaneous sourcing and dispersed source array, to validate these concepts in a 3D setting and unlock their significant potential onshore Abu Dhabi. This paper introduced the pilot program, and the resulting enhancements in acquisition productivity was discussed. The deblended data reconstruction and imaging workflows were reviewed to evaluate their performance and the resulting data quality. This study demonstrated that blended acquisition using these novel methods can significantly reduce turnaround time and cost, while maintaining high data quality.

Introduction

Blended acquisition refers to the continuous recording of seismic responses from incoherent shooting, where the properties are defined by the arbitrary spatial and temporal distribution of sources and their shots within the blended-source array (Berkhout, 2008). This technology holds great potential for acquiring higher data quality with lower turnaround time and cost compared with traditional acquisition methods. In fact, it is becoming common practice in the industry today.

There are numerous examples that incorporate concepts of blended acquisition, such as distance-separated simultaneous sweep or slip sweep (Bouska, 2010) and managed sources and spread (MSS) (Bagaini et al., 2012). These conventional methods impose constraints on encoding and operations, such as requiring large distance separation between shot locations and lengthy time shifts between shot times in the blended-source array. These constraints help ensure that shot-generated wavefields do not overlap spatially or temporally — at least within the offset-time window of interest — thus enabling deterministic deblending with minimal crosstalk by isolating data in the space-time domain.

Independent simultaneous sourcing (ISS) (Howe et al., 2008) is a novel concept, where sources fire independently and simultaneously in a decentralized manner, without synchronization. Various signaturing techniques can be applied, where each shot in the blended-source array is encoded with a unique signature, producing distinguishable wavefields. This signature uniqueness becomes an additional blending property, enabling more sophisticated deblending through decoding or deconvolution. Numerous examples of ISS have been implemented onshore and offshore worldwide (e.g., Kommedal et al., 2016; Stone et al., 2018; Yang et al., 2021).

Dispersed source array (DSA) (Berkhout, 2012; Caporal, Blacquiere, and Davydenko, 2016) is another innovative concept, where the blended-source array comprises different types of sources rather than identical ones — for example, several narrow-frequency-banded sources instead of a single broad-frequency-band source. These frequency-banded sources are randomly distributed and emit spectrally banded wavefields, allowing straightforward deblending via frequency-domain filtering.

As an evolution of this concept, temporally signatured and/or modulated and spatially dispersed source array (S-/M-DSA) (Ishiyama, 2022, 2023a) combines various signaturing and/or modulation in the time domain with DSA in the space domain. This approach relaxes encoding constraints and enhances operational flexibility, enabling nonuniform sampling and nonpatterned shooting in space and time. There are fewer examples of DSA than ISS; for instance, Jeong et al. (2022) applied DSA and validated the concept onshore Saudi Arabia, and Ishiyama (2023b) conducted a 2D pilot program using S-/M-DSA onshore Abu Dhabi.

Recently, we acquired and processed the first 3D pilot program using ISS and DSA onshore Abu Dhabi to validate these concepts in a 3D setting and unlock their potential in the region (Ishiyama, Aljaberi, and Hu, 2024). In this paper, we first introduce the pilot program and discuss the resulting enhancements in acquisition productivity. We then review the deblended data reconstruction and imaging workflows and evaluate their performance and the resulting data quality.

Pilot program

We acquired a 3D pilot program in a desert area onshore Abu Dhabi, conducted during a 3D production survey in the region. The pilot area spans 9.6 km × 7.2 km, forming an orthogonal patch without rolling receivers. Source lines were arranged in the east–west direction at 100 m intervals, with a shot point interval of 25 m. Receiver lines were deployed in the north–south direction at 200 m intervals, with a receiver point interval of 25 m (Table 1). Two pilot surveys — ISS and DSA — were acquired over the same area. By contrast, the production survey adopted MSS with a conventional distance-time rule: a minimum distance separation of 8000 m and time shifts greater than 3 s among shots in the blended-source array. Shot

Manuscript received 13 July 2025; revision received 22 October 2025; accepted 3 November 2025.
[1]INPEX Corporation, Minato-ku, Tokyo, Japan. E-mail: tomohide.ishiyama@inpex.co.jp.
[2]ADNOC, Abu Dhabi, UAE. E-mail: afra.aljaberi@adnoc.ae.

Downloaded from http://pubs.geoscienceworld.org/seg/tle/article-pdf/45/2/73/7765650/tle-v45-n2.pdf by Shivaji Maitra on 19 February 2026

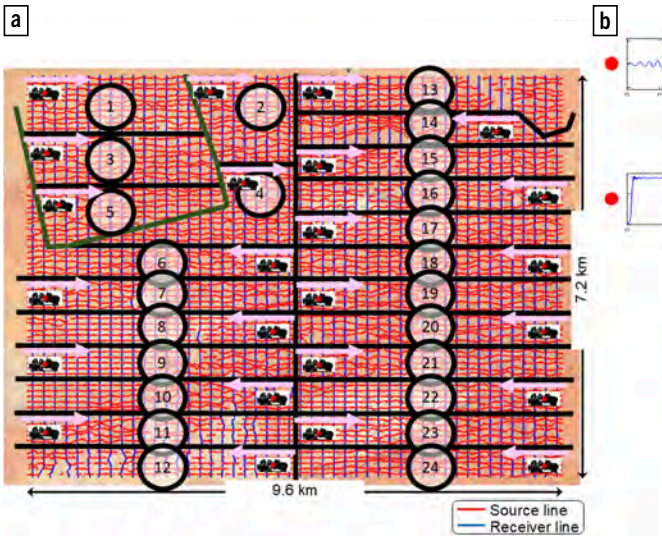

Figure 1. (a) Source spread and (b) reference sweep for the ISS survey.

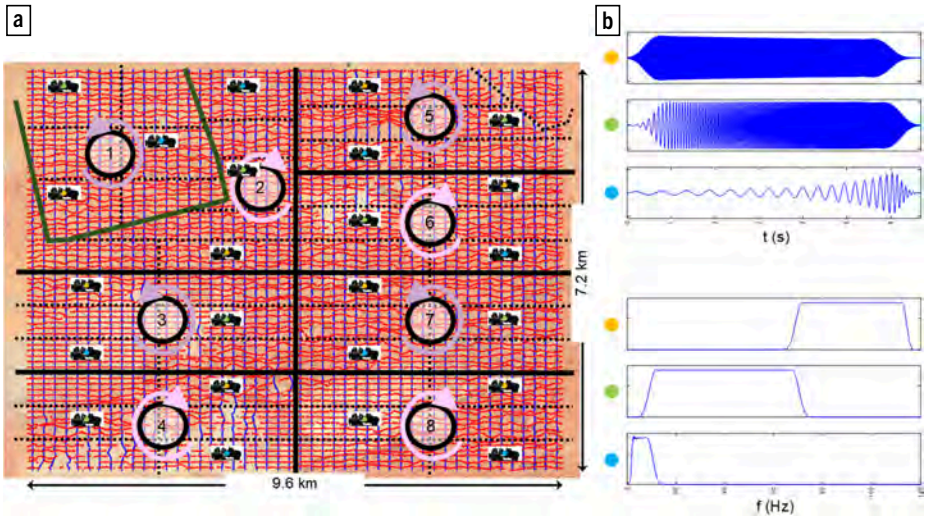

Figure 2. (a) Source spread and (b) reference sweeps for the DSA survey.

Table 1. Geometry parameters for the 3D pilot program.

Geometry	An orthogonal patch without roll
SP interval	25 m
SL interval	100 m
SL length	9.6 km
Nominal number of SPs	27,648 SPs (=384 SPs/SL × 72 SLs)
RP interval	25 m
RL interval	200 m
RL length	7.2 km
Nominal number of RPs	13,824 RPs (=288 RPs/RL × 48 RLs)

RL, receiver line. RP, receiver point. SL, source line. SP, shot point.

and receiver preplots were redesigned and rearranged to bypass natural and anthropogenic obstacles, such as massive sand dunes in the south and a fenced farm in the northwest.

Figure 1a illustrates the source spread for the ISS survey. The blended-source array consisted of 24 sources, with 24 fleets (i.e., one source per fleet). Each fleet covered a source spread of 4.8 km × 0.6 km (nominally 1152 shot points), forming an independent sourcing area where a single broad-frequency-band source fired independently at each shot point. Figure 1b shows the reference sweep, which spans 1.5–120 Hz. The sweep length was 18 s, with a listening time of 6 s, resulting in a recording time of 24 s. The sweep was a low-dwell type, increasing the duration spent at low frequencies and reducing the drive level to achieve a flat spectrum.

Figure 2a illustrates the source spread for the DSA survey. The DSA also included 24 sources, but organized into eight fleets, each containing three frequency-banded sources. Each fleet covered a source spread of 4.8 km × 1.8 km (nominally 3456 shot points) in each independent sourcing area. Multiple frequency-banded sources fired independently and simultaneously at each shot point, meaning that each shot point was occupied three times — once by each frequency-banded source. This resulted in three frequency-banded shot gathers after correlation with each reference sweep and ultimately a full-frequency-band gather after vertical stacking during processing. The nature of the DSA concept allows multiple sources within an independent sourcing area, as they emit spectrally banded, distinguishable, and thus deblendable wavefields. Furthermore, it allows a larger independent sourcing area so that, for a given frequency band, blending noise could come farther away from shots with larger distance separation.

Figure 2b shows the reference sweeps for the DSA survey. The sweep bands for the three frequency-banded sources were low frequency (1.5–12 Hz), mid frequency (8–72 Hz), and high frequency (68–115 Hz). The frequency overlaps were tested and decided in the field to achieve a flat spectrum after vertical stacking, though the flatness depends on surface conditions at shot locations. Each sweep had a length of 6.7 s, with its own sweep rate — approximately dividing the 18 s sweep length of the broad-frequency-band source by the number of frequency

Downloaded from http://pubs.geoscienceworld.org/seg/tle/article-pdf/45/2/73/7765650/tle-v45-n2.pdf by Shivaji Maitra on 19 February 2026

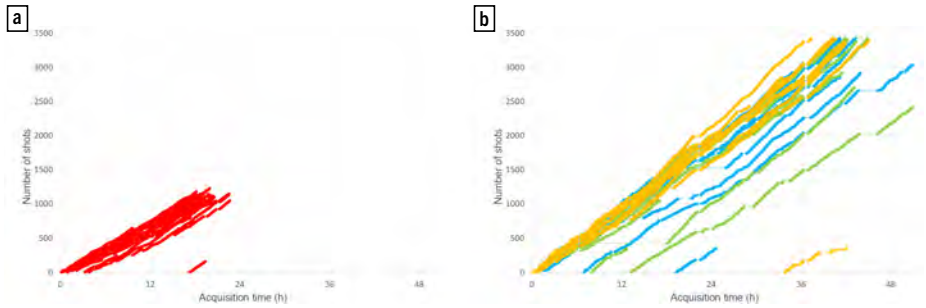

Figure 3. Productivity plots of acquisition time versus the number of shots for every source in the blended-source array: (a) ISS survey and (b) DSA survey. Red indicates shots from the broad-frequency-band sources. Blue, green, and orange indicate shots from the frequency-banded sources: the low-, mid-, and high-frequency sources, respectively.

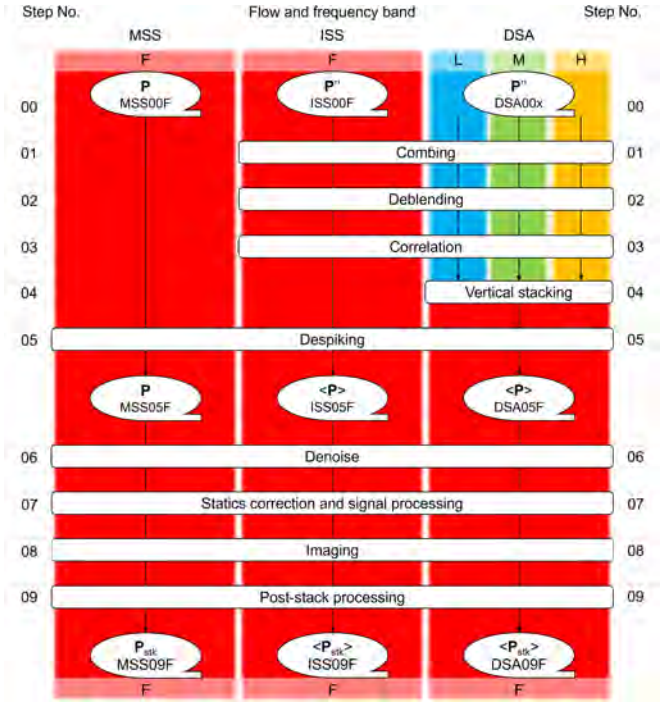

Figure 4. Processing flows with their inputs, outputs, and steps for the pilot surveys. The steps 01–05 are for deblended data reconstruction, and the steps 06–09 are for imaging. Red indicates the full frequency band. Blue, green, and orange indicate the low-, mid-, and high-frequency bands, respectively.

Table 2. Blending parameters and resulting acquisition time for the pilot surveys.

Pilot survey	MSS	ISS	DSA
Number of sources	2	24	24
Number of fleets	2	24	8
Independent sourcing area (km × km)	—	4.8 × 0.6	4.8 × 1.8
Sweep length (s)	18.0	18.0	6.7
Acquisition time (h)	288	24	48

bands (three). The listening time remained 6 s, resulting in a recording time of 12.7 s.

Acquisition productivity

We evaluated the acquisition productivity enhanced by ISS and DSA. Figure 3 shows the productivity plots of acquisition time versus the number of shots for every source in the blended-source array for the ISS and DSA surveys, respectively. Table 2 reveals the acquisition time read from the productivity plots.

For the ISS survey with nominal 1152 shots for every fleet in each independent sourcing area, the total time was about 24 h (Figure 3a). For the DSA survey with nominal 3456 simultaneous shots for every fleet in each independent sourcing area, the total time after subtracting downtime was about 48 h (Figure 3b). When some vibrators had technical problems during the operations, spare vibrators replaced the ones to minimize the downtime and assure continuous operations always with 24 vibrators.

In addition, assume MSS for the pilot survey, where at most two sources in the blended-source array could fairly simultaneously fire with certain distance separation and time lags, based on the distance-time rule used in the production survey. For this MSS survey, the total time might be approximately 288 h, taking into consideration the time duration of 24 h for the ISS survey.

Table 2 summarizes the actual acquisition time for the ISS and DSA surveys and the estimated time for the MSS survey. Assuming the MSS survey as the benchmark, the ISS survey shows a significantly shorter duration, resulting in substantially higher productivity. This improvement is primarily due to increasing the number of fleets while reducing the size of the independent sourcing area. A trade-off, however, is the increased blending fold, which can make deblending more challenging.

For the DSA survey, the acquisition time is also shorter than the benchmark, leading to higher productivity. This is additionally attributed to the reduction in sweep length, proportional to the number of frequency bands. A key advantage of the DSA concept is that it naturally simplifies and strengthens deblending due to the spectral separation of wavefields.

In conclusion, ISS and DSA considerably enhance acquisition productivity compared with conventional blending methods.

It should be noted that certain spatial sampling concepts could further improve acquisition productivity. These include the following:

- Nonuniform sampling, inspired by compressive sensing (CS) (Herrmann, 2010; Mosher et al., 2014), where shot and/or receiver points are sampled in a nonuniform and undersampled manner.
- Multiscale sampling, derived from the DSA concept (Berkhout, 2012), where frequency-banded sources are distributed according to the Nyquist criterion for each

Downloaded from http://pubs.geoscienceworld.org/seg/tle/article-pdf/45/2/73/7765650/tle-v45-n2.pdf by Shivaji Maitra on 19 February 2026

frequency band. Low-frequency sources are optimally sparsely sampled, whereas high-frequency sources are relatively densely sampled. This decreases the number of shots, particularly for low-frequency sources, thereby increasing the acquisition productivity.

However, these advanced sampling strategies are beyond the scope of this pilot program.

Deblended data reconstruction performance

We processed the pilot data sets, and Figure 4 illustrates the respective processing flows for the ISS and DSA surveys, along with the MSS survey (i.e., the production survey). We first applied deblended data reconstruction to the blended data sets. The flows include several steps: combing or pseudodeblending, which extracts each shot record within an appropriate time window from a continuous record; deblending and correlation with the reference sweep; vertical stacking to merge frequency

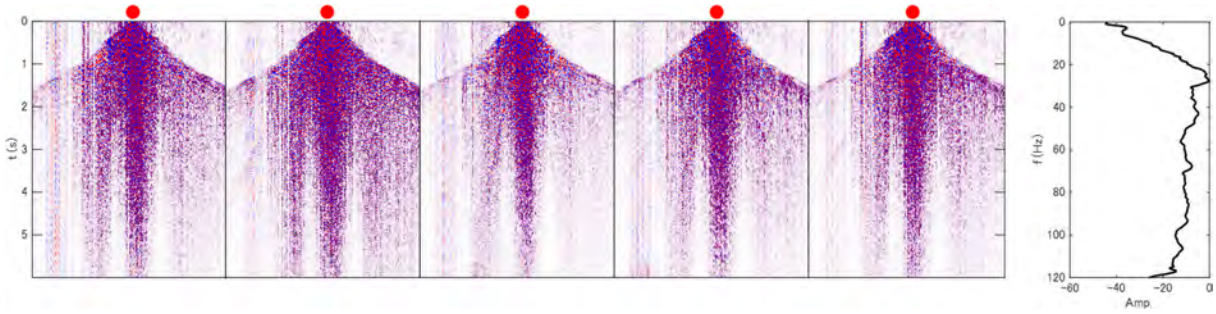

Figure 5. Raw data along with their spectrum from the MSS survey. The shot gathers are from five shot points around the center of the patch. Compare the benchmark data with **Figure 6b** for the ISS survey and **Figure 7d** for the DSA survey.

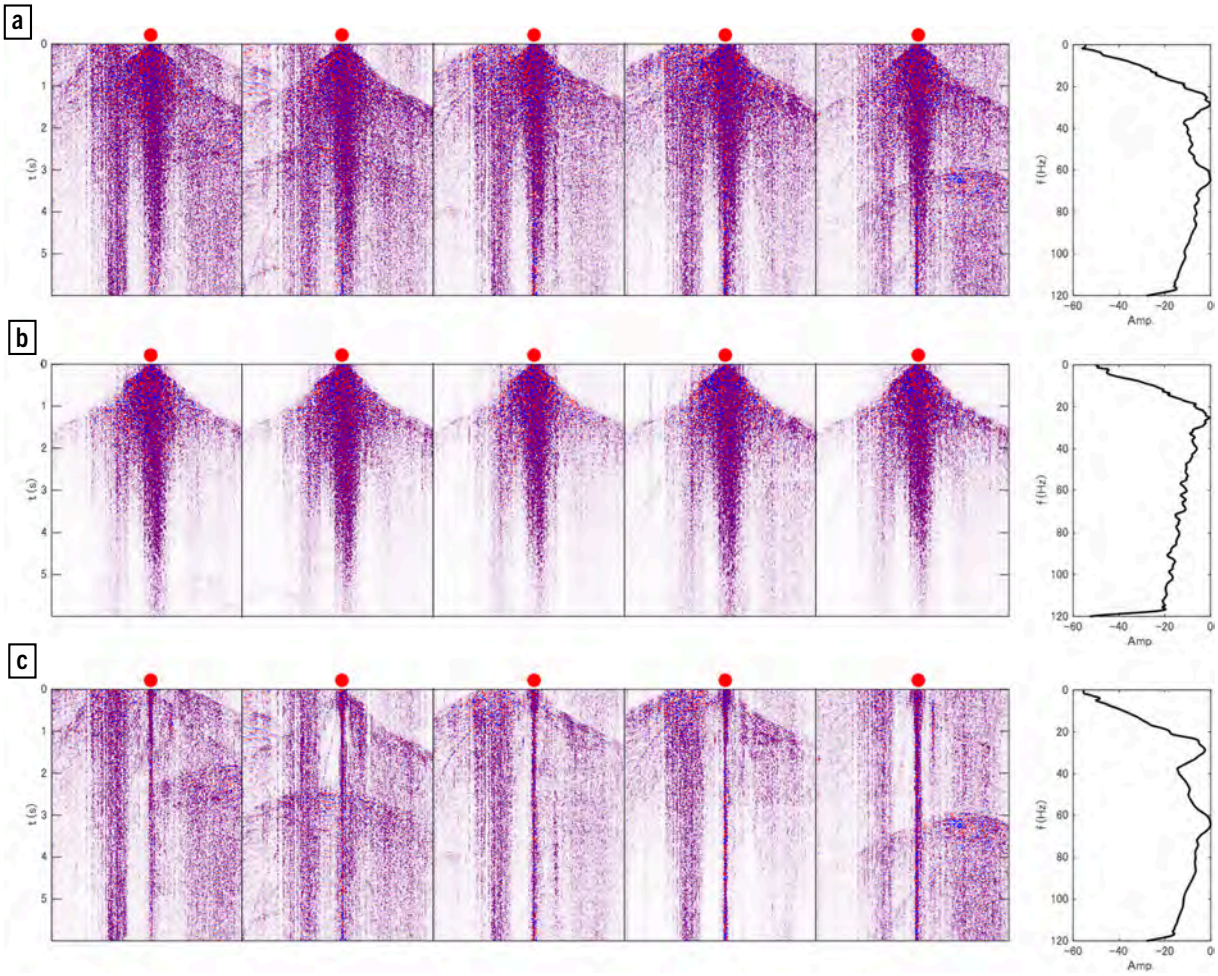

Figure 6. Deblended data reconstruction results along with their spectra for the ISS survey. The shot gathers are from five shot points around the center of the patch: (a) pseudodeblended gathers, (b) deblended gathers, and (c) difference between the two gathers.

Downloaded from http://pubs.geoscienceworld.org/seg/tle/article-pdf/45/2/73/7765650/tle-v45-n2.pdf by Shivaji Maitra on 19 February 2026

bands into a full frequency band (for the DSA survey); and despiking to suppress harmonic noise. An iterative optimization scheme based on sparse inversion (Song et al., 2019) was applied for deblending. The same processing parameters and velocity model were used across all flows as consistently as possible to minimize any differences due to processing effects.

Figure 5 presents the raw data from the MSS survey, which serves as a form of unblended data and acts as the benchmark. Although considered a reference, the benchmark data still contain residual harmonic noise, which will be addressed in subsequent processing stages.

Figure 6 presents the deblended data reconstruction results for the ISS survey. Figure 6a shows the pseudodeblended data and their spectrum, obtained by combing the blended data, followed by correlation for display purposes. The shot-generated wavefields exhibit severe overlap and interference across the full frequency band. Figure 6b displays the deblended data and their spectrum, in which the blending signal (i.e., the target shot-generated wavefields) is effectively extracted and separated through successful deblending. Figure 6c displays the difference between the two data sets and their spectrum, which primarily contains blending noise (i.e., shot-generated

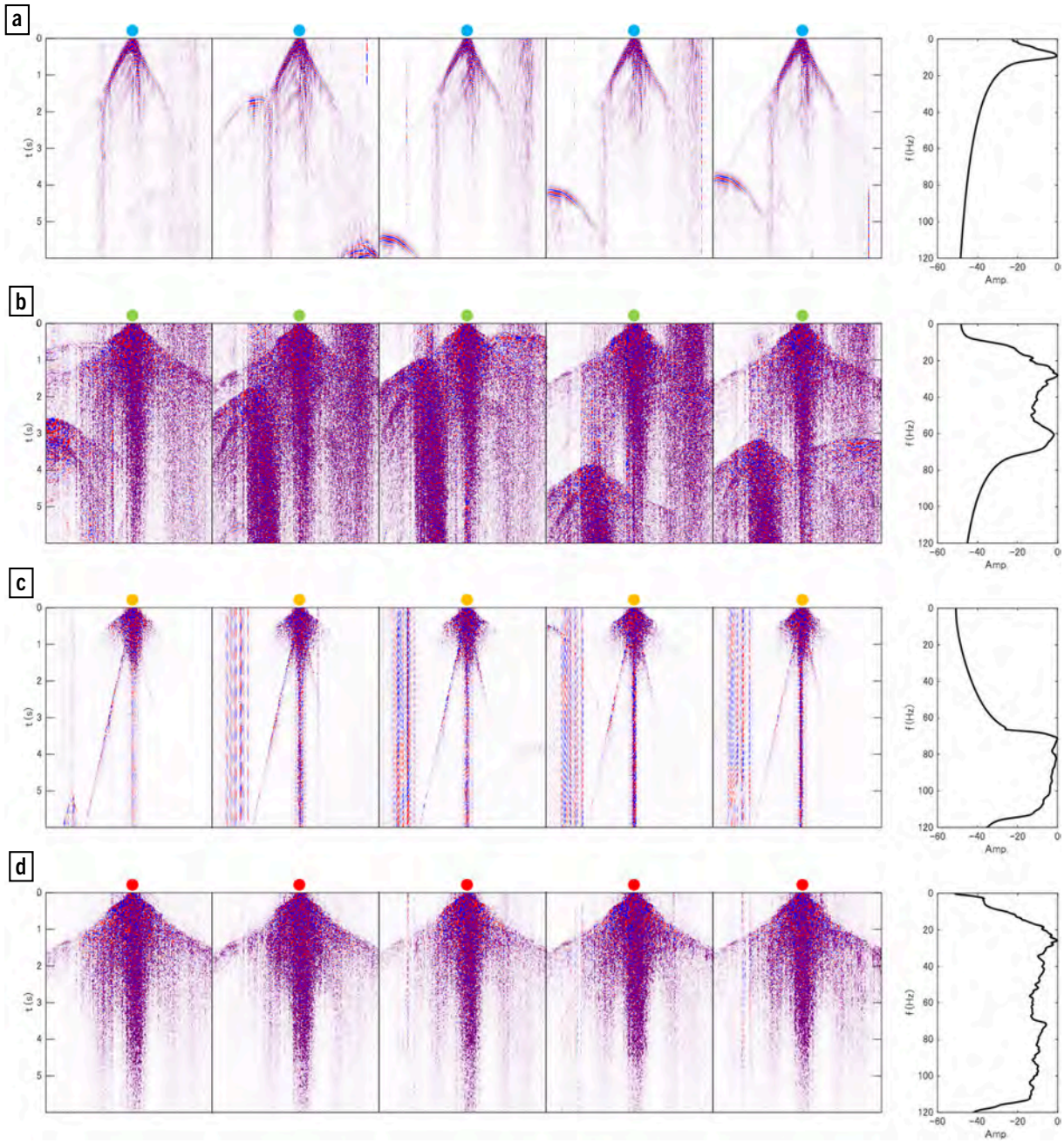

Figure 7. Deblended data reconstruction results along with their spectra for the DSA survey. The shot gathers are from five shot points around the center of the patch: (a) pseudodeblended gathers in the low-frequency band, (b) ones in the mid-frequency band, (c) ones in the high-frequency band, and (d) deblended and vertical-stacked gathers.

Downloaded from http://pubs.geoscienceworld.org/seg/tle/article-pdf/45/2/73/7765650/tle-v45-n2.pdf by Shivaji Maitra on 19 February 2026

wavefields other than the target ones). This confirms that the deblended data were successfully reconstructed from the blended input.

Figure 7 presents the deblended data reconstruction results for the DSA survey. Figure 7a–7c shows the pseudodeblended data sets in each frequency band and their spectra, obtained by combing the blended data, followed by correlation for display purposes. The shot-generated wavefields are already separated into distinct frequency bands by correlating the blended data with each reference sweep.

Figure 7d shows the deblended and vertically stacked data in the full frequency band and their spectrum. After effective deblending in each frequency band, the spectral energy is fully recovered and well balanced across the full frequency band through vertical stacking. This confirms that full-frequency-band deblended data were successfully reconstructed from the frequency-banded blended inputs.

In fact, the results from the ISS and DSA surveys closely resemble the benchmark data, further validating that the deblended data reconstruction was successfully achieved.

Imaging performance

We then applied imaging to the deblended data sets. The flows include several conventional steps: denoising to attenuate ground-roll noise; statics correction and signal processing; and prestack imaging followed by poststack processing (Figure 4).

We introduced several quantitative attributes — normalized root mean square (NRMS), predictability, amplitude spectrum, and signal-to-noise ratio (S/N) relative to the benchmark — to evaluate imaging performance and resulting data quality. NRMS and predictability are commonly used to assess repeatability or similarity in 4D seismic studies (Kragh and Christie, 2002). NRMS ranges from 0% to 200%, with values below 35% generally considered good, and predictability ranges from 0% to 100%, with values above 85% regarded as acceptable.

Figure 8 shows the final image from the MSS survey, serving as the benchmark. Figure 9 presents the stack sections at each processing stage for the ISS survey. Figure 9a shows the result after deblended data reconstruction, Figure 9b after denoising and signal processing, and Figure 9c the final image, along with its NRMS and predictability metrics. As the imaging flow progresses, various types of noise are attenuated, signals are enhanced, and the subsurface is increasingly well imaged. Correspondingly, the NRMS decreases to 34% on average, and predictability increases to 93%.

Figure 10 shows the final image for the DSA survey, along with its NRMS and predictability. Similar to

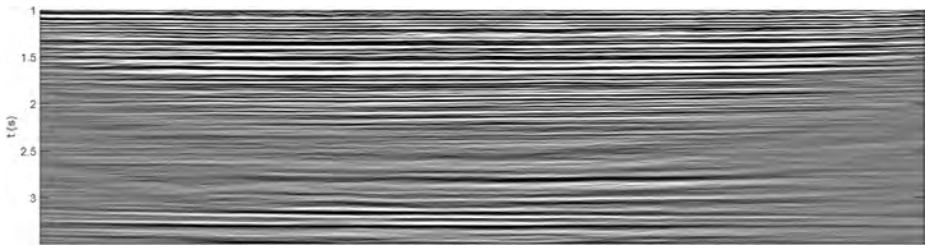

Figure 8. Imaging results from the MSS survey. The final image is from an inline around the center of the patch.

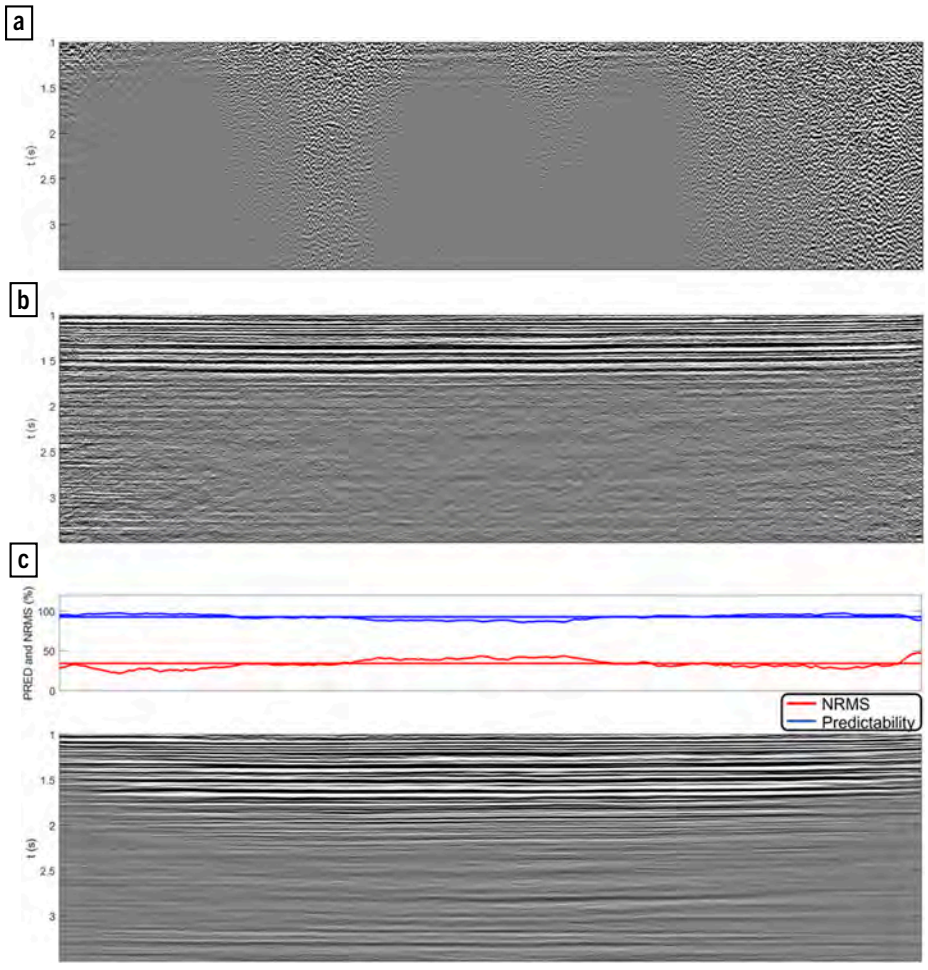

Figure 9. Imaging results for the ISS survey. The stack section is from an inline around the center of the patch. (a) Stack section after deblended data reconstruction, (b) one after denoising and signal processing, and (c) the final image along with its NRMS and predictability in the curves and the average values in the straight lines.

Downloaded from http://pubs.geoscienceworld.org/seg/tle/article-pdf/45/2/73/7765650/tle-v45-n2.pdf by Shivaji Maitra on 19 February 2026

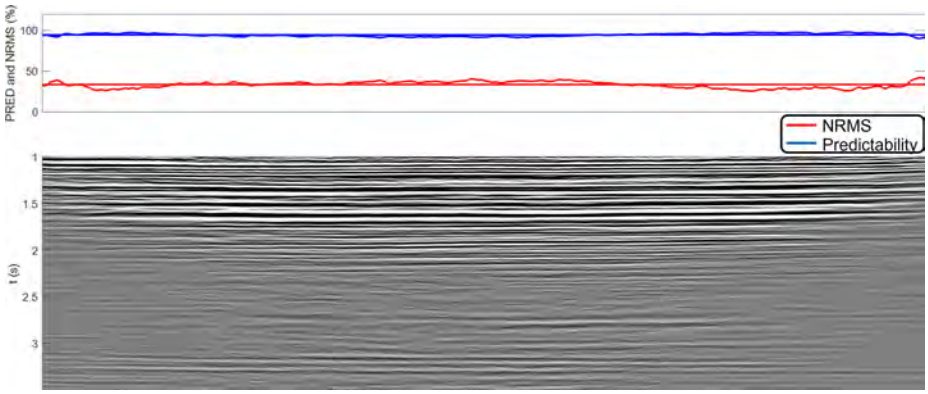

Figure 10. Imaging results for the DSA survey. The final image is from an inline around the center of the patch, along with its NRMS and predictability in the curves and the average values in the straight lines.

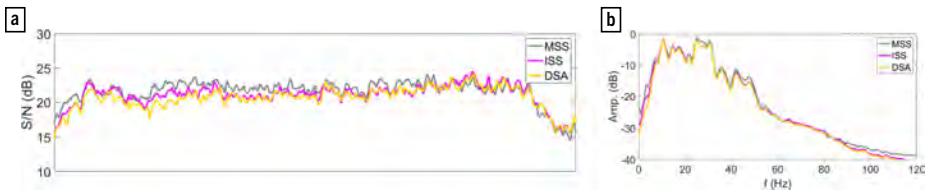

Figure 11. (a) Absolute S/N of the final images along the inline for the pilot surveys. (b) Amplitude spectra of the final images across the full frequency band for the pilot surveys.

Table 3. Resulting quantitative attributes of the final images for the pilot surveys.

Pilot survey	MSS	ISS	DSA
NRMS	—	34.2	33.6
Predictability	—	92.8	94.5
ΔAmplitude (dB)	—	−1.0	−1.4
ΔS/N (dB)	—	−0.5	−0.9
Absolute S/N (dB)	21.9	21.4	21.0

the ISS survey, the subsurface is well imaged and retains a broad frequency bandwidth. The NRMS also decreases to 34% on average, and predictability increases to 95%.

Figure 11 presents the absolute S/N and amplitude spectra of the final images for all surveys.

Table 3 summarizes the quantitative attributes of the final images. For the ISS and DSA surveys, the average NRMS is below 35% relative to the benchmark image, and the average predictability is above 90%. Furthermore, the average differences in S/N and amplitude spectrum are approximately −1 dB compared with the benchmark. These analyses indicate that the final images show no discernible differences from the benchmark. In conclusion, ISS and DSA enable deblended data reconstruction followed by imaging with high repeatability across the full frequency band.

Conclusions

We acquired and processed the first 3D pilot program using ISS and DSA onshore Abu Dhabi. These novel methods substantially improve acquisition productivity compared with conventional blending methods. Regarding processing performance, the deblended data can be reliably reconstructed from the blended input for ISS. The same holds true for DSA, with high repeatability across the full frequency band. This demonstrates that blended acquisition using these innovative methods can significantly reduce turnaround time and cost while maintaining high data quality.

There is room to improve these methods further by adopting:

- Optimized sweep design, particularly for frequency bands and overlaps, of frequency-banded sources for DSA.
- Advanced spatial sampling concepts such as nonuniform sampling based on CS and multiscale sampling derived for DSA.
- Sophisticated deblended data reconstruction algorithms, which can handle deblending, reconstruction, and vertical stacking jointly and simultaneously.

We will validate and include these options in ISS and DSA in the future.

It should be noted that health, safety, and environmental risks to field crews and greenhouse gas emissions are roughly proportional to turnaround time. This implies that the technology offers not only faster, cheaper, and higher-quality acquisition, but also safer and more environmentally responsible operations. Having confirmed and unlocked its great potential, we are committed to adopting this technology in future seismic operations. TLE

Acknowledgments

We thank ADNOC and INPEX for their support for this research and permission to publish this paper. All views and recommendations expressed in this paper are of the authors and may not necessarily be of the authors' employers.

Data and materials availability

Data associated with this research are confidential and cannot be released.

Corresponding author: tomohide.ishiyama@inpex.co.jp

References

Bagaini, C., M. Daly, and I. Moore, 2012, The acquisition and processing of dithered slip-sweep vibroseis data: Geophysical

Downloaded from http://pubs.geoscienceworld.org/seg/tle/article-pdf/45/2/73/7765650/tle-v45-n2.pdf by Shivaji Maitra on 19 February 2026

Prospecting, **60**, no. 4, 618–639, https://doi.org/10.1111/j.1365-2478.2012.01085.x.
Berkhout, A. J. "Guus," 2008, Changing the mindset in seismic data acquisition: The Leading Edge, **27**, no. 7, 924–938, https://doi.org/10.1190/1.2954035.
Berkhout, A. J., 2012, Blended acquisition with dispersed source arrays: Geophysics, **77**, no. 4, A19–A23, https://doi.org/10.1190/geo2011-0480.1.
Bouska, J., 2010, Distance separated simultaneous sweeping, for fast, clean, vibroseis acquisition: Geophysical Prospecting, **58**, no. 1, 123–153, https://doi.org/10.1111/j.1365-2478.2009.00843.x.
Caporal, M., G. Blacquiere, and M. Davydenko, 2016, 3D seismic acquisition with decentralized dispersed source arrays: 86th Annual International Meeting, SEG, Expanded Abstracts, 240–244, https://doi.org/10.1190/segam2016-13948420.1.
Herrmann, F. J., 2010, Randomized sampling and sparsity: Getting more information from fewer samples: Geophysics, **75**, no. 6, WB173–WB187, https://doi.org/10.1190/1.3506147.
Howe, D., M. Foster, T. Allen, B. Taylor, and I. Jack, 2008, Independent simultaneous sweeping — A method to increase the productivity of land seismic crews: 78th Annual International Meeting, SEG, Expanded Abstracts, 2826–2830, https://doi.org/10.1190/1.3063932.
Ishiyama, T., 2022, Method and system for seismic acquisition using a dispersed source array and spectrally non-overlapping sources: United States Patent, **US11262466B2**.
Ishiyama, T., 2023a, Blended acquisition with temporally signatured/modulated and spatially dispersed source array: Concept and method: Geophysical Prospecting, **72**, no. 2, 512–523, https://doi.org/10.1111/1365-2478.13428.
Ishiyama, T., 2023b, Blended acquisition with temporally signatured/modulated and spatially dispersed source array: The first pilot survey onshore Abu Dhabi: Geophysical Prospecting, **72**, no. 3, 938–954, https://doi.org/10.1111/1365-2478.13445.
Ishiyama, T., A. Aljaberi, and F. Hu, 2024, July 24, Blended acquisition with independent simultaneous sourcing and dispersed source array: Deblended-data-reconstruction processing: Fourth International Meeting for Applied Geoscience & Energy, SEG/AAPG, Expanded Abstracts, 2008–2012, https://doi.org/10.1190/image2024-4093808.1.
Jeong, W., C. Tsingas, and M. S. Almubarak, 2022, Deblending and merging of 3D multi-sweep seismic blended data: Geophysical Prospecting, **70**, no. 2, 246–261, https://doi.org/10.1111/1365-2478.13156.
Kommedal, J., A. Gino, W. Sean, and W. Lawrence, 2016: ISS on ice: Seismic acquisition in the Arctic, 86th Annual International Meeting, SEG, Expanded Abstracts, 6–10, https://doi.org/10.1190/segam2016-13866643.1.
Kragh, E., and P. Christie, 2002, Seismic repeatability, normalized RMS, and predictability: The Leading Edge, **21**, no. 7, 640–647, https://doi.org/10.1190/1.1497316.
Mosher, C., C. Li, L. Morley, Y. Ji, F. Janiszewski, R. Olson, and J. Brewer, 2014, Increasing the efficiency of seismic data acquisition via compressive sensing: The Leading Edge, **33**, no. 4, 386–391, https://doi.org/10.1190/tle33040386.1.
Song, J., P. Li, W. Wang, Z. Qian, P. Sun, and H. Xue, 2019, Separating Highly-Blended 3D Land Data by Sparse Inversion: 81st Conference & Exhibition, EAGE, Extended Abstracts, 1–5, https://doi.org/10.3997/2214-4609.201901053.
Stone, J., S. Wolfarth, H. Prastowo, D. Priyambodo, T. Manning, and J. Etgen, 2018, Tangguh ISS® ocean-bottom node program: A step change in data density, cost efficiency, and image quality: 88th Annual International Meeting, SEG, Expanded Abstracts, 146–150, https://doi.org/10.1190/segam2018-2996870.1.
Yang, J., X. He, J. Mei, R. Huang, Q. Li, K. Fu, and J.-P. van Gestel, 2021, September 1, Sim-source for 4D: Learnings from processing the first ISS OBN monitor survey at Atlantis: First International Meeting for Applied Geoscience & Energy, SEG/AAPG, Expanded Abstracts, https://doi.org/10.1190/segam2021-3582875.1.



10–12 Feb – Al Khobar, Saudi Arabia
SEG | DGS | SPE KSA Workshop: Bridging the Gap: Geosciences to Engineering
Registration open

16–18 Mar – Luanda, Angola
Realizing the Energy Potential of Angola Symposium
Early bird savings end 15 Feb

30 Mar–1 Apr – Al Khobar, Saudi Arabia
Near Surface Modeling, Imaging, and Characterization
Early bird savings end 28 Feb

14–16 Apr – Al Ain, UAE
8th International Conference on Engineering Geophysics
Early bird savings end 15 Feb

21–23 Apr – Abu Dhabi, UAE
Next Generation Geophysical Land & Shallow Water Acquisition Technologies
Early bird savings end 20 Mar

28–30 Apr – Sharm El Sheikh, Egypt
Mediterranean and Red Sea Exploration Summit
Early bird savings end 27 Mar

12–14 May – Muscat, Oman
New Advances in Seismic Interpretation
Call for abstracts closes 16 Feb

...and many more!

Current information as of 19 January. Please check ***seg.org/events*** *for up-to-date information and more events.*

Downloaded from http://pubs.geoscienceworld.org/seg/tle/article-pdf/45/2/73/7765650/tle-v45-n2.pdf by Shivaji Maitra on 19 February 2026

Self-supervised vision transformers for classification in unconventional shales

Rafiq Darwis Mohammad[1], Deepak Devegowda[1], Mark Curtis[1], Chandra Rai[1], Sanjana Mudduluru[1], and Sai Kiran Maryada[1]

https://doi.org/10.1190/tle-2025-0061

Abstract

Deep learning has significantly advanced image segmentation and classification, with convolutional neural networks (CNNs) traditionally dominating due to their translation and rotation invariance. However, vision transformers (ViTs) are emerging as powerful alternatives, particularly for capturing long- and short-range dependencies without requiring large, labeled data sets. These labeled data sets are time- and resource-intensive to acquire and are the major drawback of CNN-based approaches. In this study, a ViT-based architecture was applied to classify scanning electron microscopy (SEM) images from 22 unconventional shale plays across North and South America and Europe. Our data set comprised 22,440 grayscale backscattered electron SEM images. Our goal was to identify the source of the image from among 22 different unconventional plays. A reasonable classifier should possess a low rate of misclassification; however, persistent misclassification of an image from one specific play for another indicates microstructural similarities that can be exploited for operational purposes. A classifier such as the one developed in this paper can be used on any grayscale SEM image to identify a digital analog. Our approach was fully self-supervised. Using a teacher–student ViT framework, the model learned progressively without human-annotated labels. Over time, the networks distilled patterns from the data, learning distinguishing features between classes. This was then exploited by pairing the ViT-based algorithm with a k-nearest neighbors (k-NN) classifier that groups the images. These groups, remarkably, corresponded to the source of the images, and an accuracy exceeding 95% was consistently achieved. Remarkably, without prior training on labeled data, the model successfully identified key image features that inform its classification through attention maps. Our study underscores the remarkable ability of ViTs embedded in a student–teacher framework to learn underlying features and enable rapid, self-supervised classification.

Introduction

Focused ion beam-scanning electron microscopy (FIB-SEM) is an essential tool in digital rock physics, enabling high-resolution computational analysis of rock properties (Andrä et al., 2013). Widely used for visualizing, modeling, and characterizing nanoscale features in shales (Curtis, 2010; Lemmens et al., 2011; Shabro et al., 2014; Goral et al., 2015; Cudjoe et al., 2019, 2020), FIB-SEM also supports a broad range of petrophysical analyses. These include pore-throat diameter distributions, pore connectivity, and tortuosity (Dewers et al., 2012), quantitative evaluations of porosity, permeability, and transport properties (Yoon and Dewers, 2013), qualitative assessments of pore morphology (Ma et al., 2015), detailed pore classification and comparative analyses of shale formations for gas storage potential (Zhou et al., 2016), and permeability prediction (Avdonin et al., 2021).

FIB-SEM images contain important features that are necessary for petrophysical and reservoir evaluation (Curtis, 2010). These features can be extracted either manually, by carefully examining each image, or automatically, by using a feature extractor. For image-derived feature extraction, there have been several classical developments such as Sobel (Vincent and Folorunso, 2009), Scale-Invariant Feature Transform (SIFT) (Lowe, 2004), and Gray-Level Co-occurrence Matrix (GLCM) (Haralick et al., 2007). Applications of these algorithms can be seen in the work of Nakashima et al. (2017), Yoshida et al. (2018), and Gonzalez et al. (2019). More recently, there has been a rapid adoption of machine learning for feature extraction in several applications. Several of these machine learning approaches depend heavily on labeled data sets (Du et al., 2020; Yang et al., 2024; Yu et al., 2025). In contrast, other studies (Sen et al., 2019; Kim and Byun, 2021; Wibawa et al., 2023) have shown that self-supervised learning can reduce or even eliminate the need for large, labeled data sets. The emergence of transfer learning has advanced feature extraction by enabling representations from a single pretrained backbone to be reused across a wide range of downstream tasks (Caron et al., 2021; Koroteev, 2021), including image classification.

Image classification is a core task in computer vision, typically involving the categorization of images based on textures and features (Feng et al., 2019; Fang et al., 2020; Paneru and Jeelani, 2021). In the context of FIB-SEM imaging in this study, this involves labeling images of shales with the geologic formation they were sourced from. Traditionally, this task has relied on manual interpretation that is time-intensive and prone to subjective bias. In contrast, deep learning models enable automated classification that is faster, more consistent, and more scalable. Correct classifications capture distinctive microstructural features across different shale plays, whereas misclassification can reveal microstructural

Manuscript received 14 May 2025; revision received 25 August 2025; accepted 10 November 2025.

[1]University of Oklahoma, Department of Petroleum and Geological Engineering, Norman, Oklahoma. E-mail: rafiqdarwis.mohd@gmail.com; deepak.devegowda@ou.edu; mcurtis@ou.edu; crai@ou.edu; sanjana@ou.edu; sai.maryada@ou.edu.

Downloaded from http://pubs.geoscienceworld.org/seg/tle/article-pdf/45/2/73/7765650/tle-v45-n2.pdf by Shivaji Maitra on 19 February 2026

similarities, possibly indicating shared petrophysical characteristics (H. Zhang et al., 2021; Knaup et al., 2022). Systematic classification also facilitates comparative analysis across plays (Keller et al., 2011). Classifying FIB-SEM images by geologic play also enables the use of tailored models to analyze pore structures, organic matter distributions, and mineral compositions, which are the critical inputs for petrophysical modeling and reservoir evaluation (Loucks et al., 2009; Passey et al., 2010; Chalmers et al., 2012).

Classifying FIB-SEM images of shale samples presents a distinct set of challenges. First, the imaging process itself varies from image to image, with the use of different devices, different imaging parameters, and possibly different operators. Machine learning models, unfortunately, can potentially learn from imaging artifacts, thereby compromising the classification process. Standardization of the images is therefore necessary. Second, the microstructural similarity between different formations can further complicate classification tasks (Knaup et al., 2019, 2022). Figure 1 shows FIB-SEM images from the Montney, Haynesville, and Eagle Ford formations. Because the Montney and Haynesville samples appear visually similar, accurate classification can be more challenging.

The second challenge lies in the limitations of existing classification methods. Convolutional neural networks (CNNs) have been the dominant architecture for image classification (Krizhevsky et al., 2012; Hsu et al., 2020; Rakesh et al., 2022) because they are translation-invariant and harness the differences and similarities between spatially adjacent pixels. CNNs have been extensively applied to geologic image classification tasks, including shale FIB-SEM images (Knaup et al., 2019; H. Zhang et al., 2021; Knaup et al., 2022), core samples (Wang et al., 2014; Kathrada and Adillah, 2019; B. Zhang et al., 2021; Carpenter, 2024), and thin sections (Mosser et al., 2022; Tolstaya et al., 2023).

However, CNNs have limited capacity to capture long-range spatial dependencies (Raghu et al., 2021; Azad et al., 2024). In contrast, vision transformers (ViTs) have emerged as a more promising tool, capturing long-range relationships through the concept of self-attention (Dosovitskiy et al., 2020; Caron et al., 2021). Nonetheless, CNN and ViT classifiers require a robust training process that depends on the availability of large, high-quality labeled data sets. Unfortunately, this is an especially demanding requirement in domains like FIB-SEM shale imagery, where expert labeling is time-consuming and resource-intensive.

This study overcomes the need for large, manually labeled data sets by using a self-supervised learning framework that relies on the use of ViTs. Although the concept of self-supervised learning has also been applied with CNNs, they have achieved relatively limited success. Kong (2023) reports accuracies as low as 32% on the well-known modified national institute of standards and technology (MNIST) data set for handwritten digit classification. This is likely because CNNs are adept at capturing local or short-range relationships but weaker at quantifying long-range spatial dependencies.

In a very recent work, Cheng et al. (2025) showed that transformer-based encoders work well as feature extractors for detecting and describing stylolite zones in oil reservoirs using supervised learning. In another recent study, Mohammad et al. (2025) demonstrated the use of a ViT architecture for self-supervised segmentation of shale SEM images, applying a STEGO-based framework (Hamilton et al., 2022) to delineate pores, organic matter, and inorganic material. Building on this idea, our study applies a ViT as a feature extractor for SEM images but within a self-supervised setup. This removes the need for large, manually labeled data sets. Unlike the work by Mohammad et al. (2025), which focused on pixel-level segmentation, this study uses a self-supervised ViT framework for classification, leveraging the extracted representations to distinguish SEM images by play. To our knowledge, this is the first study to use a self-supervised ViT-based model for extracting features from shale SEM images for classification purposes rather than for segmentation, as in Mohammad et al. (2025). We then use the extracted features to classify the SEM images by play. Although this study focuses on source-based classification, the same workflow can be extended to other tasks such as lithology, facies, or rock type classification or more detailed geologic interpretation.

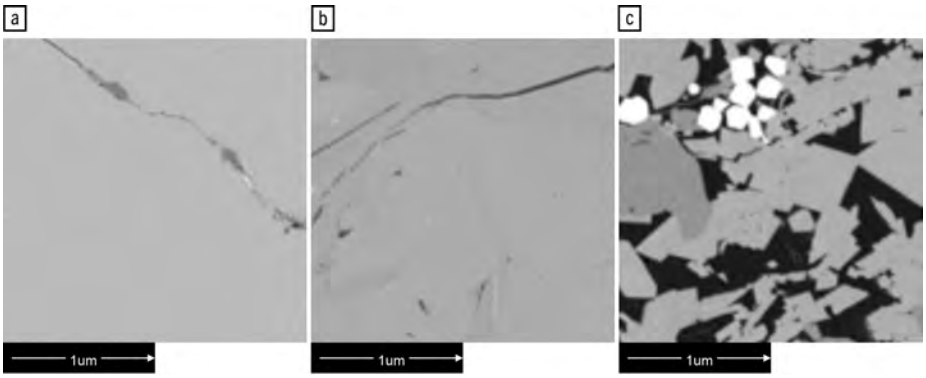

Figure 1. Examples of SEM images from (a) Montney, (b) Haynesville, and (c) Eagle Ford Gas plays. Misclassification between Montney and Haynesville often occurs due to the absence of distinct features in both formations.

Objective and importance of the study

In this work, we demonstrate the use of a self-supervised classifier of FIB-SEM images of unconventional shale plays. Although the classification can be performed by lithology, or pore types, or thermal maturity or mineralogy, in this work, we label images by their source, which is one of 22 different shale plays. These images are sourced from a single well or a few neighboring wells in each play.

The classifier was developed to demonstrate the feasibility of

Downloaded from http://pubs.geoscienceworld.org/seg/tle/article-pdf/45/2/73/7765650/tle-v45-n2.pdf by Shivaji Maitra on 19 February 2026

applying self-supervised learning to FIB-SEM image classification across these plays. Because the data set represents localized geologic conditions, the model is not intended to generalize beyond this scope but to establish a baseline framework. For data beyond this range, such as basin-wide data sets with higher geologic variability, the model would need to be retrained on the new data since it cannot reliably predict features it has not previously encountered.

When using our image data set and classifying by play or source, accurate classification of a new image indicates microstructural uniqueness specific to that play. Conversely, consistent misclassification suggests that the source of the image shares microstructural features with the predicted play.

This classifier is particularly useful for quickly evaluating images from new or undeveloped shale acreage. By highlighting microstructural commonalities between new and existing plays, it can accelerate the learning curve for selecting drilling fluids, bits, and designing completions and production management strategies, especially when detailed petrophysical and geologic data are unavailable. The workflow described in this paper therefore offers a rapid method for analyzing samples like drill cuttings to guide these key decisions.

This work uses self-supervised learning algorithms that are described later, but Knaup et al. (2022) demonstrated a similar workflow using a CNN-based classifier and labeled FIB-SEM images. Their work shows that CNN-based classifiers trained on SEM images can classify shale formations with high accuracy. Their work also shows systematic misclassification where microstructural similarities exist, for example, misclassification of the Vaca Muerta (Gas Window) with Haynesville due to shared intragranular calcite porosity and Point Pleasant with Duvernay because both contained mixed mineral phases with organic matter and intergranular porosity. In another case, Vaca Muerta (Oil Window) was strongly misidentified as La Luna, reflecting their shared abundance of calcite grains. Even in cases of misclassification, the correct formation frequently appeared as the second-highest probability, as shown in Figure 2, indicating that these overlaps highlight genuine cross-play analog relationships rather than random errors. Deep learning misclassifications therefore reinforce the geologic principle that microstructural analogs, such as pore geometries, mineral associations, or patterns, provide valuable comparative insights into reservoir characterization, which in turn can be used to leverage best practices from one play to another newer play.

Description of the data set

The data set used in this study comprises 22,440 FIB-SEM grayscale backscattered electron (BSE) images collected from 22 shale plays across North and South America and Europe. Each image was standardized to 8-bit depth to align with common machine-learning image preprocessing pipelines (Caron et al., 2021; Dosovitskiy et al., 2020), and because the grayscale contrast of microstructure in shale SEM images is sufficiently captured within 256 grayscale levels. Images were resized to 224 × 224 pixels to match the standard input resolution used by Dosovitskiy et al. (2020) in the original implementation of ViT, ensuring full compatibility with the ViT framework adopted in this study. In addition, using 8-bit, 224 × 224 images provides the necessary balance between preserving microstructural detail and maintaining computational efficiency for model training. The images were acquired by randomly cropping an original, smaller set of images with a larger field of view that were associated with a few wells in each play. This approach captured the spatial heterogeneity of the source images; however, because the images were limited to a single well or a few adjacent wells, the data set has a lesser degree of heterogeneity compared with a more systematic, unbiased large-scale sampling of each play.

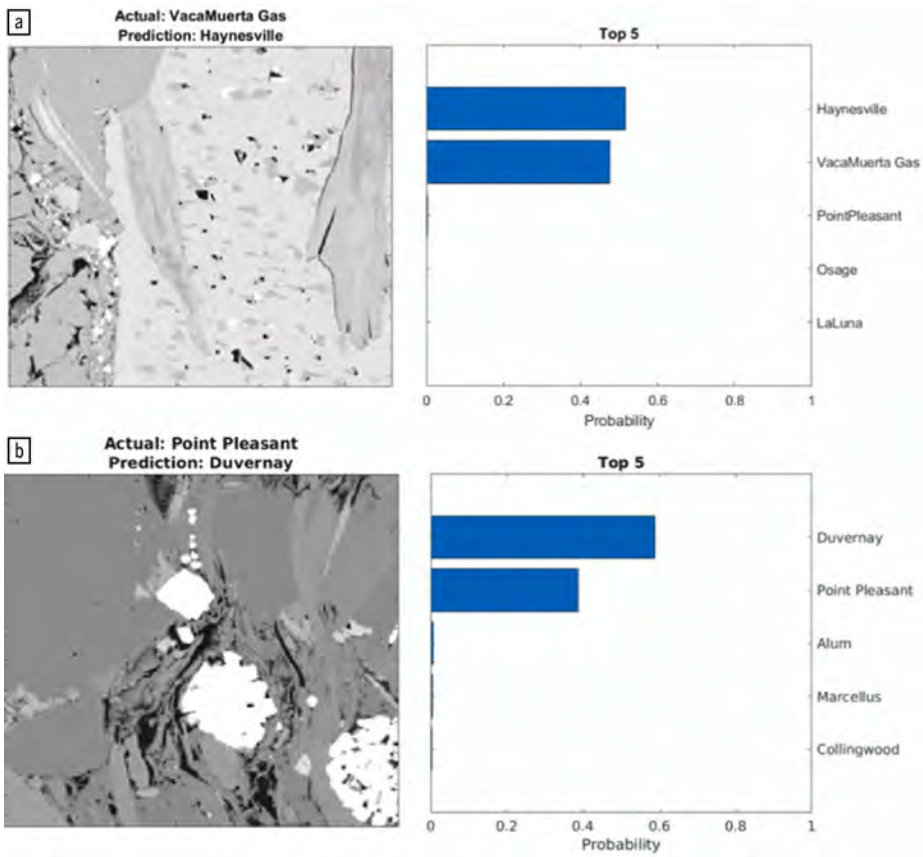

Figure 2. Examples of SEM images misclassified by a CNN-based classifier: (a) Vaca Muerta (Gas Window) predicted as Haynesville and (b) Point Pleasant predicted as Duvernay. For each case, the five formations with the highest classification probabilities are displayed to the right of the corresponding image. Image adapted from **Knaup et al. (2022)**.

Downloaded from http://pubs.geoscienceworld.org/seg/tle/article-pdf/45/2/73/7765650/tle-v45-n2.pdf by Shivaji Maitra on 19 February 2026

Additionally, H. Zhang et al. (2021) examined FIB-SEM image classification at resolutions of 10, 25, and 50 nm per pixel using a CNN-based classifier. They concluded that when comparing the performance of CNN models of similar complexity, there was little to no difference in the accuracy of classification, and consequently, in our work, we only use an image resolution of 50 nm per pixel, which has the lowest computational cost while retaining sufficient detail for classification tasks, including those that may contain only a single grain. Because of the random cropping used to generate the images, feature-poor images will likely be fewer in number.

The data set was split into 80% for training and 20% for testing and prediction. To further enhance consistency, all images were normalized based on their mean and standard deviation. This reduces variability in absolute pixel values and prevents bias toward certain grayscale ranges.

Description of a ViT

We start by introducing the architecture and core principles of a ViT, which serves as the backbone of the self-supervised classifier used in this paper.

Originally introduced for natural language processing tasks such as machine translation, transformers (Vaswani et al., 2017) laid the groundwork for advanced language models like Generative Pre-trained Transformer (GPT) (Radford, 2018; Wu et al., 2023) and Bidirectional Encoder Representations from Transformers (BERT) (Kenton and Toutanova, 2019; Koroteev, 2021) because they excel at processing sequential data, such as words in a sentence. This architecture was later adapted for computer vision tasks through ViTs (Dosovitskiy et al., 2020), which treat image patches as sequential tokens. The self-attention mechanism (Vaswani et al., 2017) in ViTs then enables quantifying relationships between adjacent image patches as well as those farther away, capturing local and global information, and providing a more complete spatial representation of the image.

The original ViT architecture, as illustrated in Figure 3 (Dosovitskiy et al., 2020), serves as the foundation for our classification algorithm. In the following section, we provide a brief overview of the image processing steps involved in enabling classification.

1) Generating input patches: ViT begins by dividing an input image into small, nonoverlapping patches. As illustrated in Figure 3, the image is split into nine distinct patches, each treated as an individual token. Each patch is then flattened from its original 2D pixel format into a 1D vector. This vector is subsequently passed through a linear projection layer, which applies trainable weights and biases for dimensionality reduction, facilitating efficient processing in subsequent layers.
2) Encoding positional information: The linearly projected tokens lack inherent information about their spatial positions within the image. To preserve the spatial structure, a positional encoding vector is added to each token. These enriched vectors, now containing content and positional context, are then passed to the transformer encoder as input.
3) The classification token: A special classification token, denoted as [CLS], is prepended to the sequence of image patches, assigned as patch 0 and bringing the total number of tokens to 10. Initially, initialized with random values, the [CLS] token learns to aggregate information from all other tokens as it passes through the trained ViT layers. The final representation of the [CLS] token is then used for downstream classification tasks.
4) The attention mechanism: Attention can broadly be defined as the relationship between pixels or patches within an image. It was originally defined to extract relationships between words in a sentence (Vaswani et al., 2017) and was later adapted for images (Vaswani et al., 2017; Dosovitskiy et al., 2020). The computation of attention is as follows: the attention head contains three weight matrices called the Query (Q), Key (K), and Value (V) matrices. The matrices represent networks with learnable weights. Each matrix operates upon the input tokens (with the positional encoding) to generate the Query, Key, and Value vectors. For each input token, the Q matrix operating on the input token generates a Query vector. For all the N input tokens, we also get N Key vectors. To assess the similarity between the fourth token and all other tokens, we "compare" the fourth Query vector with all the other N Key vectors. This is done by using a dot product between the Query and Key vectors. This scalar similarity index is multiplied with each Value (V) token and the result added together to get the attention map corresponding to fourth input tokens. In other words, a weighted average of the

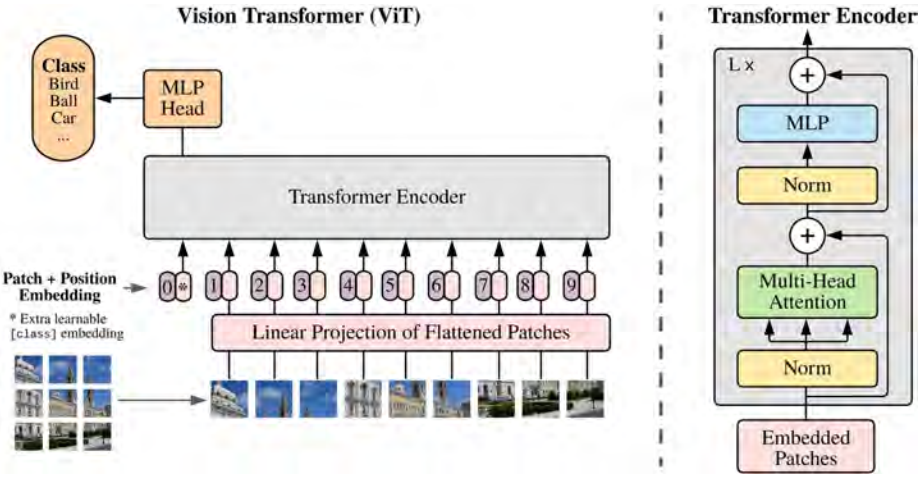

Figure 3. ViT architecture adapted from Dosovitskiy et al. (2020). In our work, we only use a transformer encoder. In the figure, MLP stands for Multilayer Perceptron.

Downloaded from http://pubs.geoscienceworld.org/seg/tle/article-pdf/45/2/73/7765650/tle-v45-n2.pdf by Shivaji Maitra on 19 February 2026

Value vectors is executed where the weights are the dot product between the Query and Key vectors. This forms the attention matrix.

Conceptually, the process can be described with an example: at the start of training, the weight matrices for Query, Key, and Value are initialized randomly, and their roles are arbitrary. As training progresses, the Query matrix perhaps learns to identify pores and its spatial juxtaposition to the organic and inorganic material, adjusting its weights accordingly. The Key matrix also learns to represent relevant features such as pores and their spatial arrangement in the image. For an image from a specific play with a specific spatial arrangement of pores, organic material, and inorganic material, the Query vector with the highest similarity to a specific Key vector passes on information that is relevant for downstream processing. The Value matrix is trained to preserve the original information of each token. Once a high Query-Key similarity is found, the corresponding Value vector is weighted accordingly, ensuring that relevant information is retained in the final attention output.

5) Multihead attention: Rather than relying on a single attention mechanism, ViTs typically use multihead attention. With two attention heads, the second head effectively computes the attention of the first attention head, which in turn captures a wider scope in the image. Recall that a single head of attention focuses on interpatch relationships only, but two heads can potentially gauge how a composite of two or three patches relates to another composite of two or three patches. With multiple heads, the information captured tends to contain global context as opposed to neighboring or local relationships.

A single ViT can be trained for classification tasks using labeled data (Bazi et al., 2021; Karuppasamy, 2023; Kim and Chung, 2024). As with any supervised learning task, this would involve successively feeding labeled images to the ViT and adjusting model parameters to minimize discrepancies between the model predictions and the labels. However, in this paper, we demonstrate how two ViTs operating in parallel as teacher and student networks can automatically extract features by progressively learning from one another during training on unlabeled images, which is without supervision.

Feature extraction with self-distillation with no labels

Next, we demonstrate how a pair of initially untrained student and teacher ViTs operating in tandem allows for knowledge distillation from one network to the other and enables classification of images. The specific algorithm we use in this work is self-distillation with no labels (DINO) (Caron et al., 2021). As shown in Figure 4, the DINO architecture consists of two ViT networks: the teacher and the student ViT network. Both networks are independently and randomly initialized at the start of the training process.

In Figure 4, DINO processes an input image x, generating two augmented views, x1 and x2. Image augmentation is a technique that introduces variation by modifying the appearance of an image to provide diverse learning perspectives (Goodfellow et al., 2016; Wang and Qi, 2022). To create these augmented views (image x1 and image x2) from the same image x, DINO randomly applies augmentation such as horizontal flipping, brightness adjustment, and Gaussian blur, ensuring that the student and teacher networks receive distinct yet related representations of the image. Additionally, DINO uses different cropping strategies: the student network receives a local crop (covering less than half of the augmented image), whereas the teacher network is given a global crop (covering more than half of the augmented image) (Caron et al., 2021).

Images x1 and x2 then pass through the student and teacher network, respectively, to produce the probability distributions, p1 and p2, corresponding to the image classes. Prior to and during the training, p1 and p2 will likely be different, and the network uses these differences to fine-tune the student and teacher parameters using backpropagation. The teacher network is further updated as a weighted sum of its own parameters and the student network parameters. Subsequent training with additional images ensures that the student and teacher networks output a similar label for the same input image x. By using local as well as global crops of an image, the networks learn local and larger-scale representations that can be used for classification. It is important to reiterate that the input image x is not labeled. Instead, the networks learn to assign the images to the same class or label. There are a few other considerations in the model architecture to ensure that the teacher and student do not converge on other trivial solutions and refer the reader to the original paper by Caron et al. (2021).

Training DINO. Caron et al. (2021) trained a ViT model using the ImageNet data set (Deng et al., 2009) and released a set of pretrained weights that can be used for computer vision problems. This pretrained ViT can then be leveraged

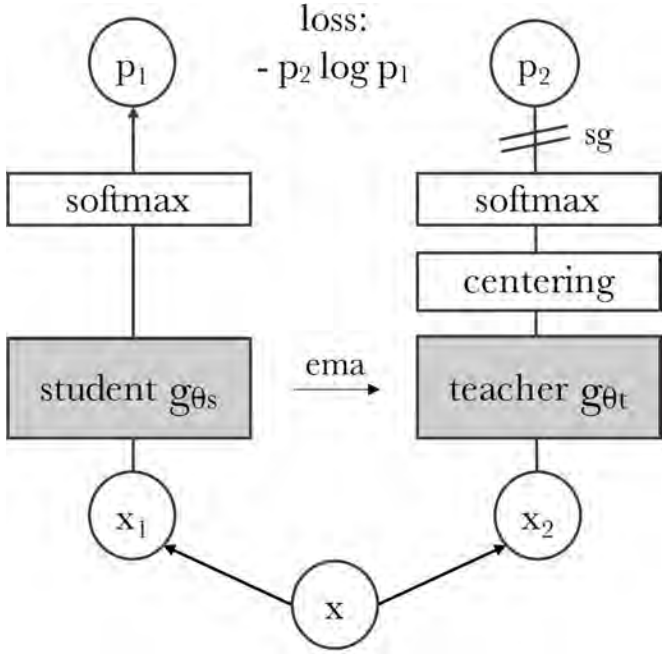

Figure 4. DINO architecture consists of two networks: a student and a teacher. Both are identical ViT networks but have different parameter sets (Caron et al., 2021).

Downloaded from http://pubs.geoscienceworld.org/seg/tle/article-pdf/45/2/73/7765650/tle-v45-n2.pdf by Shivaji Maitra on 19 February 2026

for a variety of downstream tasks, such as image classification, segmentation, and object detection (Elharrouss et al., 2024).

Using a pretrained backbone offers several advantages. There are significant savings in cost and computational effort by avoiding the need to train a machine learning model from scratch. However, a pretrained model cannot be generalized easily to data sets significantly different from the original training set. In our initial experiments, we used the published pretrained weights as the backbone and obtained a top 1 classification accuracy of less than 5% (see Table 1). We provide an explanation of top 1 classification accuracy in a later section. Clearly, the pretrained ViT backbone is unable to generalize to grayscale SEM images in unconventional shales.

To address this limitation, we retrained the DINO model from scratch using 80% of the FIB-SEM data set. Because the original DINO was developed for RGB images, we follow the procedure documented in Pfaendler et al. (2023) for our grayscale data set. We also retain the original hyperparameters from Caron et al. (2021) but modified the data augmentation workflow to include random horizontal flipping, cropping, and Gaussian blur, as well as solarization and brightness adjustments.

The resulting ViT model, trained specifically on FIB-SEM images, now serves as the backbone for the postprocessing image classification task. This version, referred to as the FIB-SEM backbone, encodes the FIB-SEM images in the form of [CLS] token vectors.

The self-supervised classifier as a feature extractor

In traditional CNN-based classifiers, deep learning features acquired from the last layer of the network contain globally relevant information of the input image. On the other hand, the intermediate feature maps point to local features necessary for classification (Prince, 2023). In ViTs, this information is contained in an attention map that provides a visual representation of how the model interprets and prioritizes different regions of an image (Dosovitskiy et al., 2020; Caron et al., 2021). Our model consists of 12 transformer blocks stacked sequentially. Each block contains a multihead self-attention mechanism that captures relationships between image patches, enabling the model to learn local and global dependencies. As the input passes through each block, the model progressively constructs more abstract and comprehensive representations. For a given input image, we extracted the attention maps from the final transformer block to visualize the regions that the ViT considers most relevant for classification.

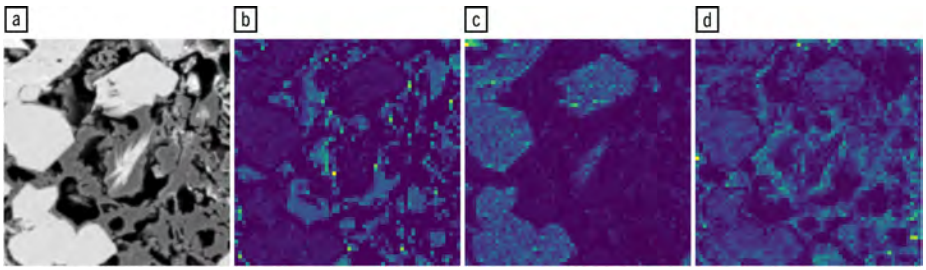

Figure 5. Example of attention maps from the ViT network for a sample image from the Vaca Muerta Gas play. (a) original sample image, (b) highlights how one attention head focuses on pores, and (c and d) illustrate attention heads capturing inorganic matter and organic matter within the image, respectively.

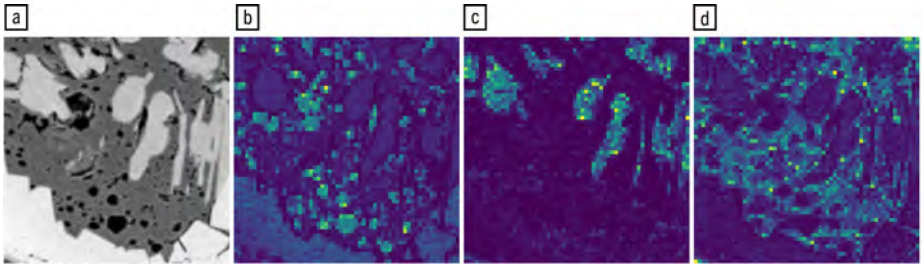

Figure 6. Example of attention maps from the ViT network for a sample image from the Eagle Ford Oil play. (a) original sample image, (b) highlights how one attention head focuses on pores, and (c and d) illustrate attention heads capturing inorganic matter and organic matter within the image, respectively.

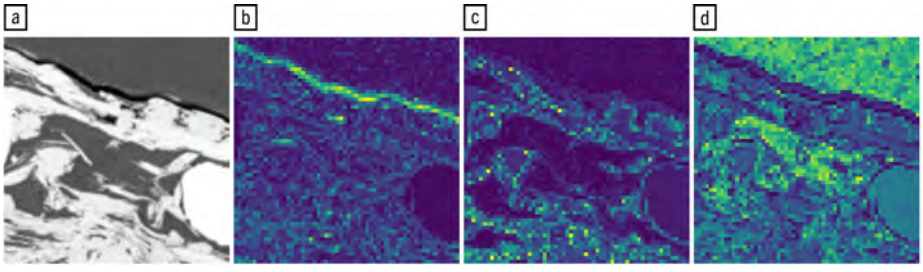

Figure 7. Example of attention maps from the ViT network for a sample image from the Marcellus play: (a) original sample image, (b) highlights how one attention head focuses on pores, and (c and d) illustrate attention heads capturing inorganic matter and organic matter within the image, respectively.

Figures 5–7 illustrate how the self-supervised learning algorithm consistently segments key microstructural features in SEM images, including pores, organic matter, and inorganic matter. In these figures, pores are represented by the darkest grayscale values, organic matter appears in medium grayscale, and inorganic matter is shown as the lightest grayscale. Figures 5 and 6 highlight pores embedded within the organic matrix, whereas Figure 7 reveals microfracture-related pores occurring at the boundaries between organic and inorganic matter. The feature extractor effectively distinguishes these components, with column (b) capturing pores, column (c) capturing inorganic matter, and column (d) capturing organic matter. Although this is outside the scope of the current work, these attention

Downloaded from http://pubs.geoscienceworld.org/seg/tle/article-pdf/45/2/73/7765650/tle-v45-n2.pdf by Shivaji Maitra on 19 February 2026

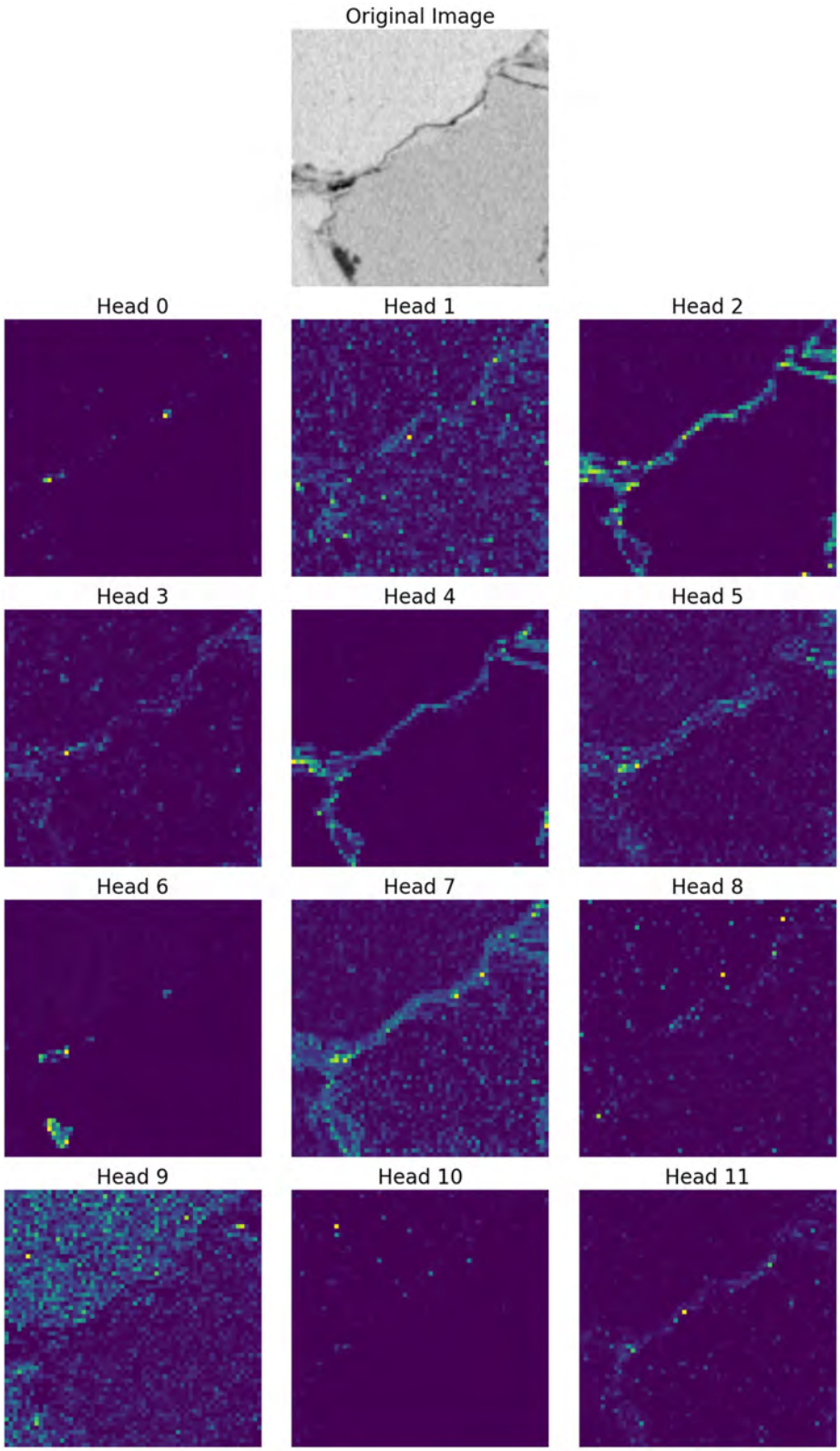

Figure 8. Example of an attention map for a sample from the Collingwood play. The numbers represent the output of each of the 12 attention heads in the ViT network. We can clearly see that the attention plots show that the networks quickly learn to identify key features (fracture in heads 2 and 4, pores in head 6, and inorganic in head 9) without any training.

maps may be used for downstream tasks such as the estimation of porosity or even using the spatial arrangement of these features to predict elastic moduli (Maryada et al., 2025).

As labeled per-pixel ground truth data were not available for this data set, quantitative verification of the attention map segmentation could not be performed. However, we have performed quantitative verification against synthetic images to show the utility of the attention maps. This is forthcoming in a different paper that follows from our prior work in Mohammad et al. (2025) where we demonstrate how the concept of attention is critical for self-supervised segmentation tasks. The segmentation can then be leveraged for additional downstream tasks such as estimation of petrophysical and mechanical properties, such as in Maryada et al. (2025) and Livingstone et al. (2025), where CNN feature maps enable quantification of elastic moduli and petrophysical properties.

Figures 8 and 9 further demonstrate the attention maps generated across all 12 heads, each emphasizing distinct structural aspects of the SEM images. Figure 8 presents an example of an attention map for a sample from the Collingwood play. The SEM image shows inorganic material in light gray at the top and some other inorganic material in a darker shade at the bottom, separated by a fracture. Pores appear as dark spots in the bottom left. Notably, heads 2 and 4 focus on the fracture, head 6 highlights the pores, and head 9 captures the inorganic material, clearly distinguishing it from the other inorganic regions. In Figure 9, the SEM image from the Duvernay play depicts the inorganic material in two different shades of gray, with organic matter embedded as darker gray areas within the lighter gray inorganic material. Here,

Downloaded from http://pubs.geoscienceworld.org/seg/tle/article-pdf/45/2/73/7765650/tle-v45-n2.pdf by Shivaji Maitra on 19 February 2026

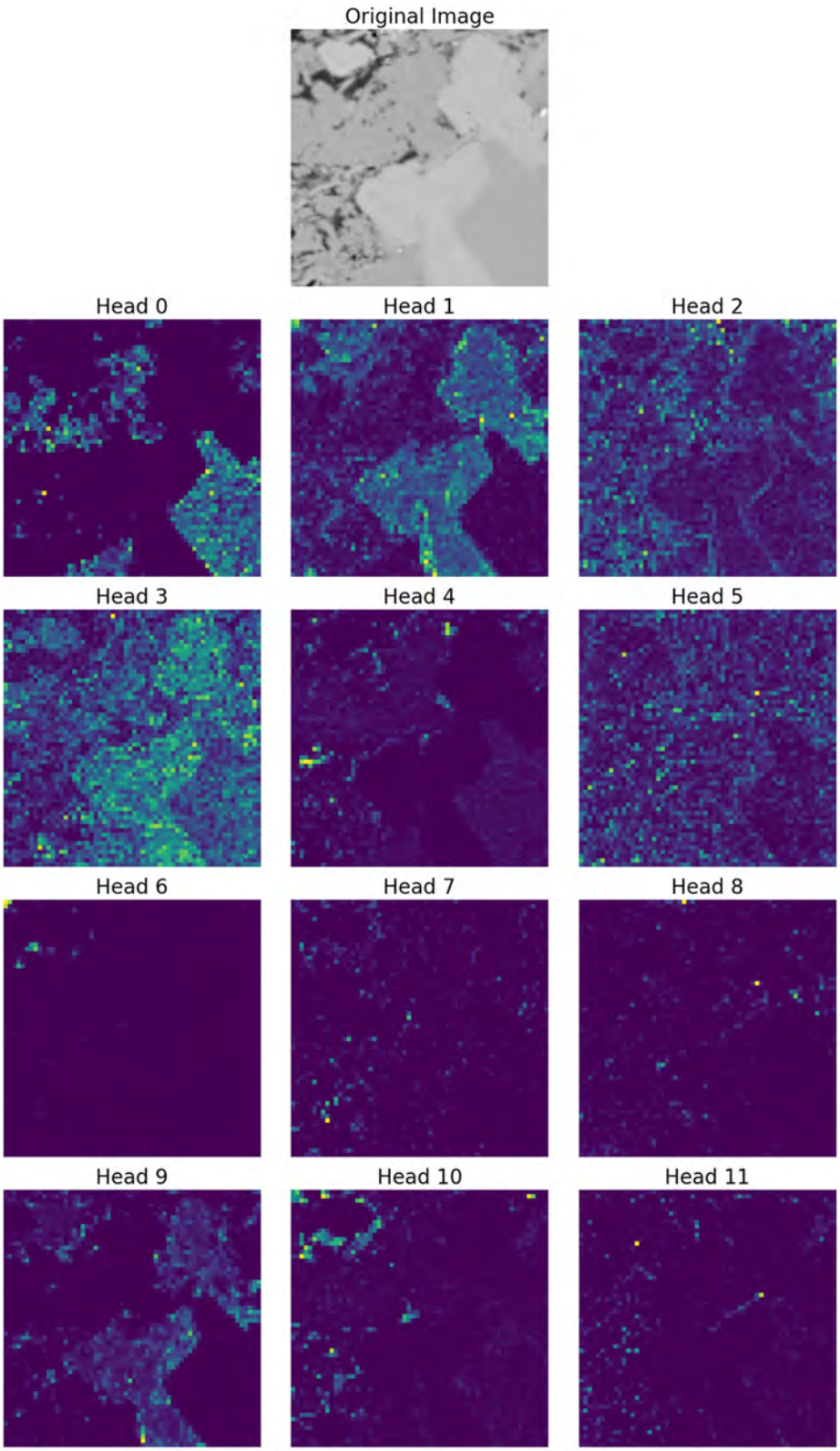

Figure 9. Example of an attention map for a sample from the Duvernay play for each of the 12 attention heads in the ViT network. Similar to Figure 8, the networks quickly learn to identify key features (inorganic in heads 0 and 1 and organic in head 10), without any training.

head 0 highlights the darker gray inorganic regions, heads 1 and 9 capture the lighter gray areas, and head 10 identifies the organic material embedded within the inorganic matrix.

More notably, these attention maps were generated from test images without any prior training. They demonstrate how the model leverages interactions between patches, as outlined in the ViT framework, to recognize patterns and features within the images. These identified features are then aggregated into a classification token, which enables effective image classification. This visualization offers insight into the underlying model reasoning, showcasing its ability to differentiate between various textures and patterns, ultimately contributing to high classification accuracy.

Downstream task — image classification by play

The *k*-nearest neighbors (*k*-NN) algorithm predicts the label of a new data point by performing a local search neighbors and assigning the majority class label among its *k*-NN (Cover and Hart, 1967; Papanikolaou et al., 2021). In this study, we use the *k*-NN as a postprocessing step for image classification. Following the training step, we now have [CLS] token vectors associated with each training image. To classify a test image, we first compute its [CLS] token using the trained FIB-SEM backbone and then measure the similarity between this token and the [CLS] tokens of its nearest neighbor images using the dot product (Caron et al., 2021; Pfaendler et al., 2023). We then rank the neighbors based on similarity and select the top 1 and top 2 most similar ones to assign class labels to the test images.

Downloaded from http://pubs.geoscienceworld.org/seg/tle/article-pdf/45/2/73/7765650/tle-v45-n2.pdf by Shivaji Maitra on 19 February 2026

Table 1. *k*-NN classification accuracy using ViT pretrained on ImageNet.

k-NN	Top 1 (%)
5	1.36
10	1.92
50	3.74
100	4.39
200	4.55
500	4.55

Finally, we compute the confusion matrix between the predicted and known test labels.

For illustration, in a 5-nearest neighbors (5-NN) approach, the classification process for a test image x follows the steps outlined in Table 2.

We test various values of **k** (5, 10, 50, 100, 200, and 500) and measure the top 1 and top 2 prediction accuracies for each case. The results, as presented in Table 3, demonstrate that the model performance is consistent and remains highly accurate across all **k** values, with only minor variations. These results indicate that the model reliably predicts the correct outcome regardless of the number of nearest neighbors considered. Additionally, the consistently high top 2 accuracy reflects the

Table 2. Steps for predicting the label associated with an image "x" using the *k*-NN classifier.

Steps	Example					
Compute the classification token (feature representation) for image x.						
Compute the dot product between image x's classification token and all stored training tokens to measure similarity.	Training image		Class		Similarity score	
	Image A		1		0.9	
Identify the top five highest similarity scores, representing the 5-nearest neighbors (5-NN) of image x.	Image B		2		0.8	
	Image C		3		0.7	
	Image D		1		0.6	
	Image E		1		0.5	
Apply temperature scaling (T = 0.1) to weight the top five nearest neighbor (5-NN) images based on their similarity scores.	Training image		Similarity score		Weight	
	Image A		0.9		Exp (0.9/0.1) = 8103	
	Image B		0.8		Exp(0.8/0.1) = 2981	
	Image C		0.7		Exp(0.7/0.1) = 1096	
	Image D		0.6		Exp(0.6/0.1) = 403	
	Image E		0.5		Exp(0.5/0.1) = 148	
Generate a one-hot encoding for the classes of the top five nearest neighbors (5-NN).	Class	Image A	Image B	Image C	Image D	Image E
	1	1	0	0	1	1
	2	0	1	0	0	0
	3	0	0	1	0	0
Calculate the weighted score for each class based on the assigned weights.	Class		Compute weighted score		Weighted score	
	1		(8103 × 1)+(0 × 2981)+(0 × 1096)+(403 × 1)+(148 × 1)		8654	
	2		(0 × 8103)+(2981 × 1)+(0 × 1096)+(0 × 403)+(0 × 148)		2981	
	3		(0 × 8103)+(0 × 2981)+(1096 × 1)+(0 × 403)+(0 × 148)		1096	
Determine the predicted class for image x. In this case, image x is classified as Class 1, as it has the highest weighted score.	Class			Weighted score		
	1			8654		
In this example, the top 1 class is Class 1, while the top 2 classes consist of class 1 and class 2.	2			2981		
	3			1096		

Downloaded from http://pubs.geoscienceworld.org/seg/tle/article-pdf/45/2/73/7765650/tle-v45-n2.pdf by Shivaji Maitra on 19 February 2026

ability of the model to predict the correct class among its two most probable predictions.

This study evaluated the consistency of the model's predictions by varying the number of nearest neighbors (**k**) considered during classification. As illustrated in Table 2, increasing **k** introduces more neighboring images and potentially additional classes when predicting the label of an input image **x**. A well-generalized model should maintain stable predictions across a reasonable range of **k** values. In this study, accuracy remained nearly invariant across **k**, which suggests that the model has learned well-separated class representations that retain images from the same class closely clustered. This stable performance across different neighborhood sizes when applied to the test data indicates the model's generalizability.

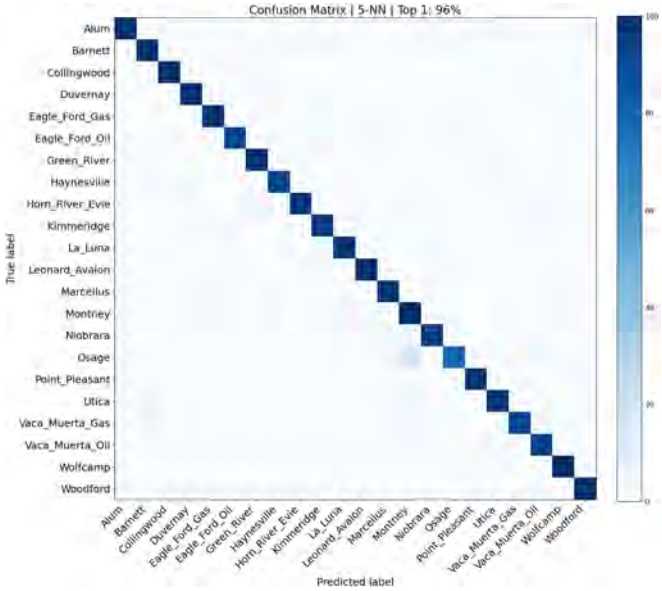

Figure 10. Confusion matrix for 5-NN classification model with an accuracy of 96%.

Figure 10 shows the model classification performance using confusion matrices for 5-NN. The confusion matrices for other choices of k for the k-NN algorithm were similar and not shown here for brevity. In Figure 10, the diagonal elements of the confusion matrix indicate the number of correct predictions, and off-diagonal terms represent misclassifications, which are relatively sparse.

Examples of misclassified images. In this section, we discuss a few misclassified samples and attempt to showcase what might be causing the errors. Although the misclassification rate is less than 5%, it might be instructive to understand the underlying cause. The first row in Figure 11 displays images that were misclassified, and the second row shows randomly selected images associated with the predicted label for comparison.

1) Column (a) — The true label is Eagle Ford Oil, but the image is classified as Leonard Avalon. Both images display elongated intragranular pores, which may have led the model to group them together.
2) Column (b) — The true label is Haynesville, but the image is classified as Montney. Both samples exhibit microfractures combined with isolated intragranular pores, producing a similar overall texture.
3) Column (c) — The true label is Barnett, but the image was classified as Alum. Both samples are organic-rich and display randomly oriented clay and inorganic material.

These examples suggest that the model is sensitive to shared microstructural signatures across plays, even when the formations themselves are distinct. Rather than treating these as simple misclassifications, such overlaps can be interpreted as potential cross-play analogs. In practice, recognizing that formations with different geologic histories can exhibit similar pore-scale features may provide valuable analogs for reservoir evaluation, particularly when direct data from a target play are limited. These misclassified images point to underlying geologic similarities at the microstructural scale. Using the classifier on samples from newer previously unseen plays, for instance, can provide microstructural analogies across formations, thereby providing a means to leverage information from one play to another across formation boundaries.

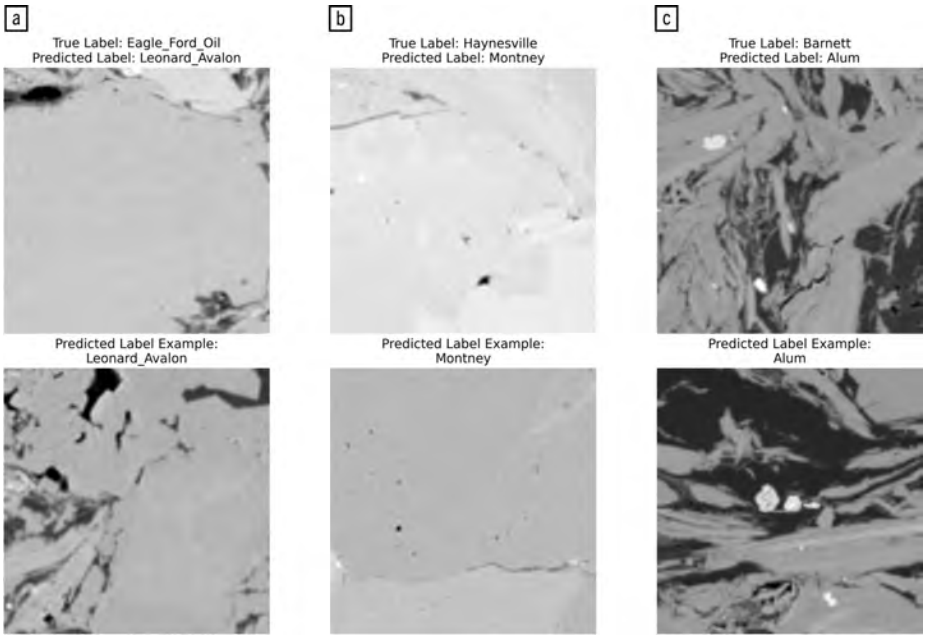

Figure 11. Examples of misclassified images. The first row displays the misclassified images along with their true labels and corresponding predicted labels. The second row provides reference examples of the predicted labels for comparison. Column (a) presents an example of misclassification from the Eagle Ford Oil play, (b) from the Haynesville play, and (c) from the Barnett play.

Downloaded from http://pubs.geoscienceworld.org/seg/tle/article-pdf/45/2/73/7765650/tle-v45-n2.pdf by Shivaji Maitra on 19 February 2026

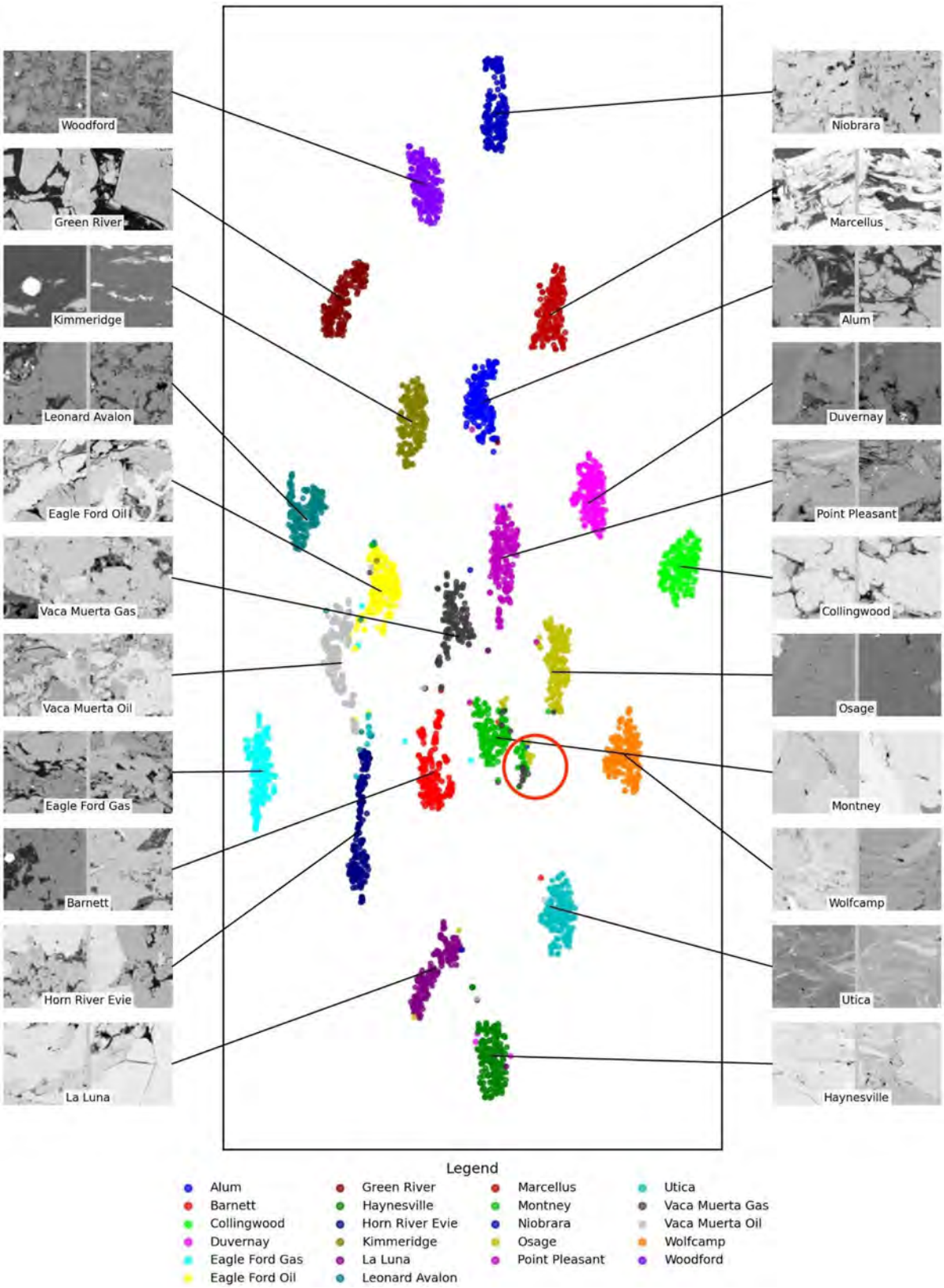

Figure 12. t-SNE visualization of the test images in the learned feature space. The plot shows well-defined clusters, with plays that share similar textures and microstructural characteristics positioned close to one another. The red circle shows a few samples from Vaca Muerta Gas sharing similar characteristics as the Montney, which is also reflected in the confusion matrix in **Figure 10**.

Downloaded from http://pubs.geoscienceworld.org/seg/tle/article-pdf/45/2/73/7765650/tle-v45-n2.pdf by Shivaji Maitra on 19 February 2026

Table 3. *k*-NN classifier results for various *k*-values using the FIB-SEM backbone.

k-NN	Top 1 (%)	Top 2 (%)
5	96	97
10	96	97
50	96	98
100	96	98
200	95	98
500	95	97

Distance-based clustering plot

Figure 12 presents a t- distributed stochastic neighbor embedding (t-SNE) plot (Maaten and Hinton, 2008) that visualizes how SEM images from different plays are arranged within the learned feature space. The input to this visualization consists of the raw feature vectors extracted from the test SEM images using our trained FIB-SEM ViT backbone; therefore, it reflects how the backbone organizes samples in feature space based solely on their extracted representations. t-SNE reduces these high-dimensional vectors into a two-dimensional map by converting distances between data points into probabilities that reflect their relative similarity. Because it preserves the local structure, the method makes clusters and relationships easier to interpret in a low-dimensional space. Only test data were used to generate this plot. Although t-SNE is not a part of our workflow, it is instructive to visualize these images and assess similarities and differences.

The visualization shows that the test SEM images form well-defined clusters corresponding to their respective plays. Several plays, including Niobrara, Woodford, Kimmeridge, Collingwood, Green River, and Wolfcamp, appear as tight and compact groups with no stray samples. Plays with similar textures or microstructural characteristics also appear closer to one another in the feature space, such as the Eagle Ford Oil and Vaca Muerta Oil samples.

These distance-based clustering measures, performed independently using the trained ViT backbone, demonstrate how each play is distinct and how a select few possess shared characteristics. The Niobrara, Marcellus, Woodford, and Collingwood samples form unique clusters in Figure 12. On the other hand, samples that share visually similar microstructures share similar areas of the t-SNE plot. Examples include Vaca Muerta Oil and Eagle Ford Oil samples. Nearby, there are also samples from the Horn River Evie, Vaca Muerta Gas, Montney, Osage, and the Barnett, indicating shared characteristics. A comparison of this plot with the confusion matrix in Figure 10 shows misclassifications that largely mirror the cluster arrangements. For example, we observe in Figure 10, the misclassification of Vaca Muerta Gas samples as Montney, which is reflected in the t-SNE plot of Figure 12 (highlighted in the red circle).

Conclusions

In this study, we explore the application of self-supervised learning with a model based on a ViT architecture for classifying shale SEM images, and the following conclusions can be drawn from this work:

1) The self-supervised classifier shows a high accuracy and a low rate of misclassification.
2) The misclassified images indicate shared microstructural features between two plays. These cross-play analogs can be used to guide completion design, drilling, and reservoir management when a more complete petrophysical and geologic analysis is absent. For example, shared features in images from a newer undeveloped acreage can be used to accelerate the learning curve for completion practices and production strategies for the new locations.
3) This study shows that self-supervised ViTs can serve as effective feature extractors for SEM images of unconventional shales, eliminating the need for large, manually labeled data sets. The model successfully captures critical microstructural features that distinguish shale plays.
4) Using the feature extractor as the backbone, the FIB-SEM image classification by play using *k*-NN classifiers achieves consistently high accuracy across 22 shale plays despite subtle variations in imaging conditions and microstructural similarities between formations.
5) The integration of attention mechanisms within the ViT model provides valuable insights into the features prioritized by the model during learning.

These findings show that self-supervised ViTs can function as powerful feature extractors, eliminating the reliance on large manually labeled data sets and capturing key microstructural differences between shale plays. When paired with *k*-NN classifiers, the learned features enable accurate and consistent classification across 22 shale plays, even in the presence of subtle imaging and microstructural variations. Importantly, the integration of attention mechanisms provides interpretability, revealing the features emphasized by the model during learning.

Future work may expand the post-classification analysis to better interpret the learned representations. This includes identifying the most discriminating parameters that drive classification decisions and potential sources of misclassification. Further comparison with explicit image-based metrics could also provide complementary insights into the relationship between learned features and microstructural characteristics. TLE

Data and materials availability

The data used in this work are not publicly available. They may be obtained, at cost, by contacting Dr. Chandra Rai, crai@ou.edu.

Downloaded from http://pubs.geoscienceworld.org/seg/tle/article-pdf/45/2/73/7765650/tle-v45-n2.pdf by Shivaji Maitra on 19 February 2026

Appendix A – Example of SEM images from all plays

Corresponding author: deepak.devegowda@ou.edu

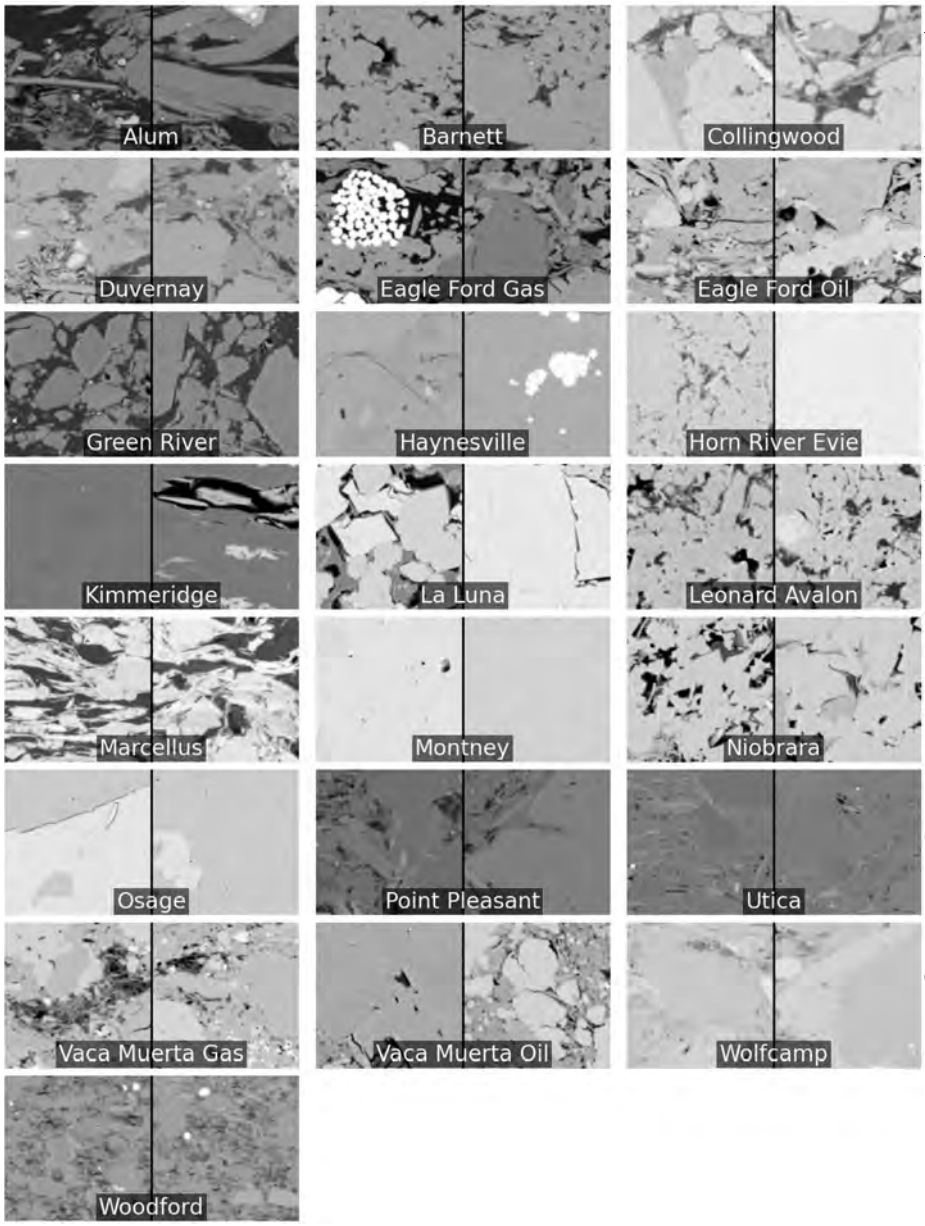

Figure A 1. Example of SEM images from each play used in this study. In general, we can observe a few similarities between the randomly selected Montney and Haynesville images and the Leonard-Avalon and Eagle Ford samples, which led to the misclassification described in Figure 11. Not all images in these plays share similar characteristics. Although we did observe several instances of misclassification of Barnett samples as Alum, the misclassified images are distinct from what is shown above for the Barnett. This is simply because different regions of play can exhibit different characteristics.

References

Andrä, H., N. Combaret, J. Dvorkin, E. Glatt, J. Han, M. Kabel, Y. Keehm, et al., 2013, Digital rock physics benchmarks—Part I: Imaging and segmentation: Computers & Geosciences, **50**, 25–32, https://doi.org/10.1016/j.cageo.2012.09.005.

Avdonin, A., M. Ebadi, and V. Krutko, 2021, Application of high-contrast μct and fib-sem for the improvement in the permeability prediction of tight rock samples: SPE Russian Petroleum Technology Conference, SPE, D031S018R005, https://doi.org/10.2118/206588-MS.

Azad, R., A. Kazerouni, M. Heidari, E. K. Aghdam, A. Molaei, Y. Jia, A. Jose, et al., 2024, Advances in medical image analysis with vision Transformers: A comprehensive review: Medical Image Analysis, **91**, 103000, https://doi.org/10.1016/j.media.2023.103000.

Bazi, Y., L. Bashmal, M. M. A. Rahhal, R. A. Dayil, and N. A. Ajlan, 2021, Vision transformers for remote sensing image classification: Remote Sensing, **13**, no. 3, 516, https://doi.org/10.3390/rs13030516.

Caron, M., H. Touvron, I. Misra, H. Jégou, J. Mairal, P. Bojanowski, and A. Joulin, 2021: Emerging properties in self-supervised vision transformers: IEEE/CVF international conference on computer vision, 9650–9660, https://doi.org/10.1109/ICCV48922.2021.00951.

Carpenter, C., 2024, Machine-learning techniques classify, quantify cuttings lithology: Journal of Petroleum Technology, **76**, no. 1, 92–94, https://doi.org/10.2118/0124-0092-JPT.

Chalmers, G. R., R. M. Bustin, and I. M. Power, 2012, Characterization of gas shale pore systems by porosimetry, pycnometry, surface area, and field emission scanning electron microscopy/transmission electron microscopy image analyses: Examples from the Barnett, Woodford, Haynesville, Marcellus, and Doig units: AAPG Bulletin, **96**, no. 6, 1099–1119, https://doi.org/10.1306/10171111052.

Cheng, J., B. He, and R. Horne, 2025, A data-driven approach for stylolite

Downloaded from http://pubs.geoscienceworld.org/seg/tle/article-pdf/45/2/73/7765650/tle-v45-n2.pdf by Shivaji Maitra on 19 February 2026

detection: SPE Journal, **30**, no. 1, 1–12, https://doi.org/10.2118/214831-PA.
Cover, T., and P. Hart, 1967, Nearest neighbor pattern classification: IEEE Transactions on Information Theory, **13**, no. 1, 21–27, https://doi.org/10.1109/TIT.1967.1053964.
Cudjoe, S., Q. Fu, J. S. Tsau, R. Barati, R. Goldstein, B. Nicoud, A. Baldwin, et al., 2020, A reconstructed core-scale model of the lower eagle ford shale through fib-sem: sem-eds, and microscopy for gas huff-n-puff simulation: SPE Improved Oil Recovery Conference, SPE, D021S033R002, https://doi.org/10.2118/200379-MS.
Cudjoe, S., S. Liu, R. Barati, F. Hasiuk, R. Goldstein, J. Tsau, and D. Mohrbacher, 2019, Pore-scale characterization of eagle ford outcrop and reservoir cores with sem/bse, eds fib-sem, and lattice boltzmann simulation, spe-195805-ms spe annual technical conference and exhibition: Society of Petroleum Engineers, **30**, https://doi.org/10.2118/195805-MS.
Curtis, M. E., 2010, Structural characterization of gas shales on the micro-and nano-scales: Canadian Unconventional Resources and International Petroleum Conference, SPE–137693, https://doi.org/10.2118/137693-MS.
Deng, J., W. Dong, R. Socher, L. J. Li, K. Li, and L. Fei-Fei, 2009, ImageNet: A large-scale hierarchical image database: 2009 IEEE Computer Society Conference on Computer Vision and Pattern Recognition Workshops (CVPR Workshops), Miami, FL, 248–255, https://doi.org/10.1109/CVPR.2009.5206848.
Dewers, T. A., J. Heath, R. Ewy, and L. Duranti, 2012, Three-dimensional pore networks and transport properties of a shale gas formation determined from focused ion beam serial imaging: International Journal of Oil, Gas and Coal Technology, **5**, no. 2/3, 229, https://doi.org/10.1504/IJOGCT.2012.046322.
Dosovitskiy, A., L. Beyer, A. Kolesnikov, D. Weissenborn, X. Zhai, T. Unterthiner, M. Dehghani, et al., 2020, An image is worth 16x16 words: Transformers for image recognition at scale: arXiv Preprint arXiv:2010.11929.
Du, X., Y. Jin, X. Wu, Y. Liu, X. Wu, O. Awan J. Roth, et al, 2020, Classifying cutting volume at shale shakers in real-time via video streaming using deep-learning techniques: SPE Drilling & Completion, **35**, no. 3, 317–328, https://doi.org/10.2118/194084-PA.
Elharrouss, O., Y. Akbari, N. Almadeed, and S. Al-Maadeed, 2024, Backbones-review: Feature extractor networks for deep learning and deep reinforcement learning approaches in computer vision: Computer Science Review, **53**, 100645, https://doi.org/10.1016/j.cosrev.2024.100645.
Fang, W., P. E. D. Love, H. Luo, and L. Ding, 2020, Computer vision for behaviour-based safety in construction: A review and future directions: Advanced Engineering Informatics, **43**, 100980, https://doi.org/10.1016/j.aei.2019.100980.
Feng, X., Y. Jiang, X. Yang, M. Du, and X. Li, 2019, Computer vision algorithms and hardware implementations: A survey: Integration, **69**, 309–320, https://doi.org/10.1016/j.vlsi.2019.07.005.
Gonzalez, A., L. Kanyan, Z. Heidari, and O. Lopez, 2019, Integrated multi-physics workflow for automatic rock classification and formation evaluation using multi-scale image analysis and conventional well logs: SPWLA Annual Logging Symposium, SPWLA, D033S001R001, https://doi.org/10.30632/T60ALS-2019_A.
Goodfellow, I., Y. Bengio, and A. Courville, 2016, Deep Learning: The MIT Press.
Goral, J., I. Miskovic, J. Gelb, and M. Andrew, 2015, Correlative xrm and fib-sem for (non) organic pore network modeling in woodford shale rock matrix: International Petroleum Technology Conference, PTC, D021S005R001, https://doi.org/10.2523/IPTC-18477-MS.
Hamilton, M., Z. Zhang, B. Hariharan, N. Snavely, and W. T. Freeman, 2022, Unsupervised semantic segmentation by distilling feature correspondences, https://doi.org/10.48550/arXiv.2203.08414.
Haralick, R. M., K. Shanmugam, and I. H. Dinstein, 2007, Textural features for image classification: IEEE Transactions on Systems, Man, and Cybernetics, **SMC-3**, no. 6, 610–621, https://doi.org/10.1109/TSMC.1973.4309314.
Hsu, C.Y., C.C. Tseng, S.L. Lee, and B.Y. Xiao, 2020, Image classification using convolutional neural networks with different convolution operations: 2020 IEEE International Conference on Consumer Electronics - Taiwan (ICCE-Taiwan), IEEE, 1–2, https://doi.org/10.1109/ICCE-Taiwan49838.2020.9258148.
Karuppasamy, A., 2023, Recent vit based models for breast cancer histopathology image classification: 14th International Conference on Computing Communication and Networking Technologies (ICCCNT), IEEE, 1–5, https://doi.org/10.1109/ICCCNT56998.2023.10306739.
Kathrada, M., and B. J. Adillah, 2019, Visual recognition of drill cuttings lithologies using convolutional neural networks to aid reservoir characterisation: SPE Reservoir Characterisation and Simulation Conference and Exhibition, SPE, D031S020R003, https://doi.org/10.2118/196675-MS.
Keller, L. M., L. Holzer, R. Wepf, and P. Gasser, 2011, 3D geometry and topology of pore pathways in Opalinus clay: Implications for mass transport: Applied Clay Science, **52**, no. 1–2, 85–95, https://doi.org/10.1016/j.clay.2011.02.003.
Kenton, J. D. M. W. C., and L. K. Toutanova, 2019, Bert: Pre-training of deep bidirectional transformers for language understanding: Proceedings of NAACL-HLT, 4171–4186.
Kim, D., and J. Byun, 2021, September 1, Automatic computation of relative geologic time volume using self-supervised learning: SEG International Exposition and Annual Meeting, SEG, D011S048R002, https://doi.org/10.1190/segam2021-3581832.1.
Kim, G. I., and K. Chung, 2024, Vit-Based Multi-Scale Classification Using Digital Signal Processing and Image Transformation: IEEE Access.
Knaup, A., J. Jernigen, M. Curtis, D. Devegowda, C. Sondergeld, and C. Rai, 2022, Application of deep learning to shale microstructure classification: Marine and Petroleum Geology, **144**, 105842, https://doi.org/10.1016/j.marpetgeo.2022.105842.
Knaup, A. S., J. D. Jernigen, M. E. Curtis, J. W. Sholeen, J. J. Borer IV, C. H. Sondergeld, and C. S. Rai, 2019, Unconventional reservoir microstructural analysis using sem and machine learning: SPE/AAPG/SEG Unconventional Resources Technology Conference, URTeC, D023S042R005, https://doi.org/10.15530/urtec-2019-638.
Kong, S., 2023, Self-supervised image classification using convolutional neural network: 3rd International Conference on Power, Electronics and Computer Applications (ICPECA), IEEE, 1283–1290, https://doi.org/10.1109/ICPECA56706.2023.10075949.
Koroteev, M. V., 2021, Bert: A review of applications in natural language processing and understanding: arXiv Preprint arXiv:2103.11943.
Krizhevsky, A., I. Sutskever, and G. E. Hinton, 2012, Imagenet classification with deep convolutional neural networks: Advances in Neural Information Processing Systems, 25.
Lemmens, H., A. Butcher, and P. Botha, 2011, Fib/sem and sem/edx: A new dawn for the sem in the core lab?: Petrophysics, **52**, 452–456.

Downloaded from http://pubs.geoscienceworld.org/seg/tle/article-pdf/45/2/73/7765650/tle-v45-n2.pdf by Shivaji Maitra on 19 February 2026

Livingstone, L., P. Yeturi, I. Cherukuri, D. Devegowda, M. Curtis, C. Rai, and S. K. Maryada, 2025, Deep learning-based estimation of petrophysical properties for unconventional shales from SEM images: ADIPEC, ADIPEC, SPE–229323.

Loucks, R. G., R. M. Reed, S. C. Ruppel, and D. M. Jarvie, 2009, Morphology, genesis, and distribution of nanometer-scale pores in siliceous mudstones of the mississippian barnett shale: Journal of Sedimentary Research, **79**, no. 12, 848–861, https://doi.org/10.2110/jsr.2009.092.

Lowe, D. G., 2004, Distinctive image features from scale-invariant keypoints: International Journal of Computer Vision, **60**, no. 2, 91–110, https://doi.org/10.1023/B:VISI.0000029664.99615.94.

Ma, Y., N. Zhong, L. Cheng, Z. Pan, H. Li, Q. Xie, and C. Li, 2015, Pore structure of two organic-rich shales in southeastern chongqing area: Insight from focused ion beam scanning electron microscope (fib-sem): Petroleum Geology & Experiment, **37**, 1–8, https://doi.org/10.7603/s40972-015-0018-2.

Mohammad, R. D., D. Devegowda, C. Rai, M. Curtis, S. Mudduluru, and S. K. Maryada, 2025, Self-supervised learning using vision transformer architecture for rock image segmentation: SPE Europec featured at EAGE Conference and Exhibition, SPE–225609.

Mosser, L., G. Ghon, and G. Baechle, 2022, Interpretation of deep neural networks for carbonate thin section classification: Second International Meeting for Applied Geoscience & Energy, SEG/AAPG, Expanded Abstracts, 371–375, https://doi.org/10.1190/image2022-3748082.1.

Maaten, L. v. d., and G. Hinton, 2008, Visualizing data using t-SNE: Journal of Machine Learning Research, **9**, no. Nov, 2579–2605.

Maryada, S.K., D. Devegowda, C. Rai, M. Curtis, D. Ebert, and G. Danala, 2025, An improved data-driven method for the prediction of elastic properties in unconventional shales from SEM images: Geoenergy Science and Engineering, **254**, 214043, https://doi.org/10.1016/j.geoen.2025.214043.

Nakashima, S., T. Sakamoto, H. Yasuhara, and K. Kishida, 2017, Observation and quantification of fracture aperture in granite core using x-ray tomography and edge detection technique: ARMA US Rock Mechanics/Geomechanics Symposium, ARMA, ARMA-2017–0247.

Paneru, S., and I. Jeelani, 2021, Computer vision applications in construction: Current state, opportunities & challenges: Automation in Construction, **132**, 103940, https://doi.org/10.1016/j.autcon.2021.103940.

Papanikolaou, M., G. Evangelidis, and S. Ougiaroglou, 2021, Dynamic k determination in *k*-NN classifier: A literature review: 12th International Conference on Information, Intelligence, Systems & Applications (IISA), IEEE, 1–8, https://doi.org/10.1109/IISA52424.2021.9555525.

Passey, Q. R., K. Bohacs, W. L. Esch, R. Klimentidis, and S. Sinha, 2010, From oil-prone source rock to gas-producing shale reservoir–geologic and petrophysical characterization of unconventional shale-gas reservoirs: SPE International Oil and Gas Conference and Exhibition in China, SPE, SPE-131350-MS, https://doi.org/10.2523/131350-MS.

Pfaendler, R., J. Hanimann, S. Lee, and B. Snijder, 2023, Self-supervised vision transformers accurately decode cellular state heterogeneity: Systems Biology, https://doi.org/10.1101/2023.01.16.524226.

Prince, S. J., 2023, Understanding deep learning, in Book Understanding deep learning: MIT press.

Radford, A., 2018, Improving language understanding by generative pre-training.

Raghu, M., T. Unterthiner, S. Kornblith, C. Zhang, and A. Dosovitskiy, 2021, Do vision transformers see like convolutional neural networks?: Advances in Neural Information Processing Systems, **34**, 12116–12128.

Rakesh, K., G. Namita, and R. Kulkarni, 2022, Image recognition, classification and analysis using convolutional neural networks: 2022 First International Conference on Electrical, Electronics, Information and Communication Technologies (ICEEICT), IEEE, 1–4, https://doi.org/10.1109/ICEEICT53079.2022.9768474.

Sen, S., S. Kainkaryam, C. Ong, and A. Sharma, 2019, Interpolation of regularly sampled prestack seismic data with self-supervised learning: SEG International Exposition and Annual Meeting, SEG, D023S023R006, https://doi.org/10.1190/segam2019-3215774.1.

Shabro, V., S. Kelly, C. Torres-Verdín, K. Sepehrnoori, and A. Revil, 2014, Pore-scale modeling of electrical resistivity and permeability in FIB-SEM images of organic mudrock: Geophysics, **79**, no. 5, D289–D299, https://doi.org/10.1190/geo2014-0141.1.

Tolstaya, E., A. Shakirov, and M. Mezghani, 2023, Lithology prediction from drill cutting images using convolutional neural networks and automated dataset cleaning: Abu Dhabi International Petroleum Exhibition and Conference, SPE, D021S053R001, https://doi.org/10.2118/216418-MS.

Vaswani, A., N. Shazeer, N. Parmar, J. Uszkoreit, L. Jones, A. Gomez, and Ł. Kaiser, 2017, Attention is all you need: Advances in Neural Information Processing Systems.

Vincent, O. R., and O. Folorunso, 2009, A descriptive algorithm for sobel image edge detection: Proceedings of informing science & IT education conference (InSITE), 97–107, https://doi.org/10.28945/3351.

Wang, G., Y. Ju, T. R. Carr, C. Li, and G. Cheng, 2014, Application of artificial intelligence on black shale lithofacies prediction in marcellus shale, appalachian basin: Unconventional Resources Technology Conference, Denver, Colorado, USA, Society of Exploration Geophysicists, American Association of Petroleum, Tulsa, OK, USA, 1970–1980, https://doi.org/10.15530/urtec-2014-1935021.

Wang, X., and G.J. Qi, 2022, Contrastive Learning with Stronger Augmentations: IEEE Transactions on Pattern Analysis and Machine Intelligence, **45**, 5549–5560, https://doi.org/10.1109/TPAMI.2022.3203630.

Wibawa, R., R. Rosyadi, M. Nancy, and R. Irfani Hasya Fulki, 2023, March 1, Unlocking the potential of unlabeled data in building deep learning model for dynamometer cards classification by using self-supervised learning: International Petroleum Technology Conference, IPTC, D012S001R004, https://doi.org/10.2523/IPTC-23026-EA.

Wu, T., S. He, J. Liu, S. Sun, K. Liu, Q.L. Han, and Y. Tang, 2023, A brief overview of chatgpt: The history, status quo and potential future development: IEEE/CAA Journal of Automatica Sinica, **10**, no. 5, 1122–1136, https://doi.org/10.1109/JAS.2023.123618.

Yang, L., K. Zhang, H. Zhang, L. Zhang, J. Yao, Y. Wang, Y. Yang, et al., 2024, Predicting oil production after enhancement techniques using multidimensional feature representation learning: A case study of profile control technique: SPE Journal, **29**, no. 8, 3876–3891, https://doi.org/10.2118/221461-PA.

Yoon, H., and T. A. Dewers, 2013, Nanopore structures, statistically representative elementary volumes, and transport properties of chalk: Geophysical Research Letters, **40**, no. 16, 4294–4298, https://doi.org/10.1002/grl.50803.

Yoshida, R., S. Nakashima, Y. Yoshizu, C. Song, and K. Kishida, 2018, Co-registration of ct images by sift method and observation of temporal changes in granite fracture aperture under long-term

Downloaded from http://pubs.geoscienceworld.org/seg/tle/article-pdf/45/2/73/7765650/tle-v45-n2.pdf by Shivaji Maitra on 19 February 2026

loading: ARMA US Rock Mechanics/Geomechanics Symposium, ARMA, ARMA-2018–1253.

Yu, Z., D. Yan, and C. D. Adenutsi, 2025, Geologically constrained deep learning for lithofacies identification of mixed terrestrial shale reservoirs: Permian Fengcheng Formation, Mahu Sag, Junggar Basin, Western China: SPE Journal, **30**, no. 5, 2653–2672, https://doi.org/10.2118/225443-PA.

Zhang, B., S. Chen, Y. Xiao, L. Zhang, and C. Wang, 2021, Vision-based sedimentary structure identification of core images using transfer learning and convolutional neural network approach: SPE/AAPG/SEG Unconventional Resources Technology Conference, URTEC, D021S039R002, https://doi.org/10.15530/urtec-2021-5375.

Zhang, H., M. T. Kasumov, D. Devegowda, and M. E. Curtis, 2021, Do we really need deep learning? A study on play identification using sem images: SPE/AAPG/SEG Unconventional Resources Technology Conference, URTEC, D021S039R004, https://doi.org/10.15530/urtec-2021-5562.

Zhou, S., G. Yan, H. Xue, W. Guo, and X. Li, 2016, 2D and 3D nanopore characterization of gas shale in Longmaxi formation based on FIB-SEM: Marine and Petroleum Geology, **73**, 174–180, https://doi.org/10.1016/j.marpetgeo.2016.02.033.

Downloaded from http://pubs.geoscienceworld.org/seg/tle/article-pdf/45/2/73/7765650/tle-v45-n2.pdf by Shivaji Maitra on 19 February 2026

Reviews

Coordinated by Sergio Chávez-Pérez

Introduction to Catastrophe Risk Modelling: A Physics-Based Approach, by Arnaud Mignan, ISBN 978-1-009-43738-7, 2024, Cambridge University Press, 368 p. US$140 (hardback), US$64.99 (e-book or paperback).

Almost every day we read about another catastrophe: a war, a flood, an earthquake, a tornado, a famine. Their consequences aren't academic: family and friends almost drowned in a recent flood; our home insurance has almost doubled in the last few years. I got this book to better understand catastrophes and what can be done to lessen their impact on our lives.

It's not often that I review a book that delivers what I hoped for. In this case, it delivered a comprehensive discussion of perils, hazards, and risks; examples of how those risks can be modeled; and an overview of how models contribute to catastrophe risk mitigation and management.

This is a textbook. It has six chapters organized in three parts: Basics of Catastrophe Modelling, Advanced Catastrophe Modelling, and Catastrophe Risk Management. Each chapter includes boxes with examples or relevant information, and they conclude with exercises. There are numerous tables, figures, and charts. Most of the figures are in black and white, which is usually adequate. For some reason there is a section in the middle of the book with color versions of selected figures. The mathematics underlying every section in the book are presented simply and clearly. My memory of statistical mathematics is vague, but it was sufficient to understand the concepts presented. The author repeatedly emphasizes that the models he presents are simplistic, and that when applied to real-life applications they are much more complicated. Numerous references allow the reader to explore topics in greater depth.

The book adopts a definition for catastrophe from the United Nations International Strategy for Disaster Reduction (2009): "a serious disruption of the functioning of a community or a society involving widespread human, material, economic or environmental losses and impacts, which exceeds the ability of the affected community or society to cope using its own resources."

The need to cope with catastrophes drives our desire to understand them and quantify the risks associated with them.

Part 1: The first chapter provides a useful description of relevant terms and concepts (catastrophe, disaster, peril, hazard, risk, uncertainty, randomness, probability) and the basic components of a catastrophe model. It also includes a comprehensive description of perils, covering everything from earthquakes to epidemics, cyberattacks, and asteroid impacts. The second chapter describes probabilistic hazard assessment. It discusses point, line and area sources, event size distributions, and event intensity footprints. The third chapter builds on the previous chapters to derive the risk model framework: risk as a function of hazard, exposure, and vulnerability.

Part 2: The fourth chapter extends the static models to dynamic hazards such as wildfires and epidemics. The fifth chapter extends the models to include cascading events, events temporally clustered such as a tsunami triggered by an earthquake. It includes discussion of large-scale catastrophes such as societal or environmental collapse.

Part 3: Chapter 6 discusses the fundamentals of insurance: how risks can be reduced or managed. It includes brief but important sections on uncertainties and risk perception.

Most of us have experienced a catastrophe, either a global event like the COVID-19 pandemic or a local event like a flood. It has been said that a single death is a tragedy; a million deaths are a statistic. This book focuses on statistics: the probability of an earthquake, the value of infrastructure. It is important, however, to never forget the tragedies.

I enjoyed this book. I would recommend it to anyone who is interested in the fundamentals of quantifying risks.

— Ray Wood
Hastings, New Zealand

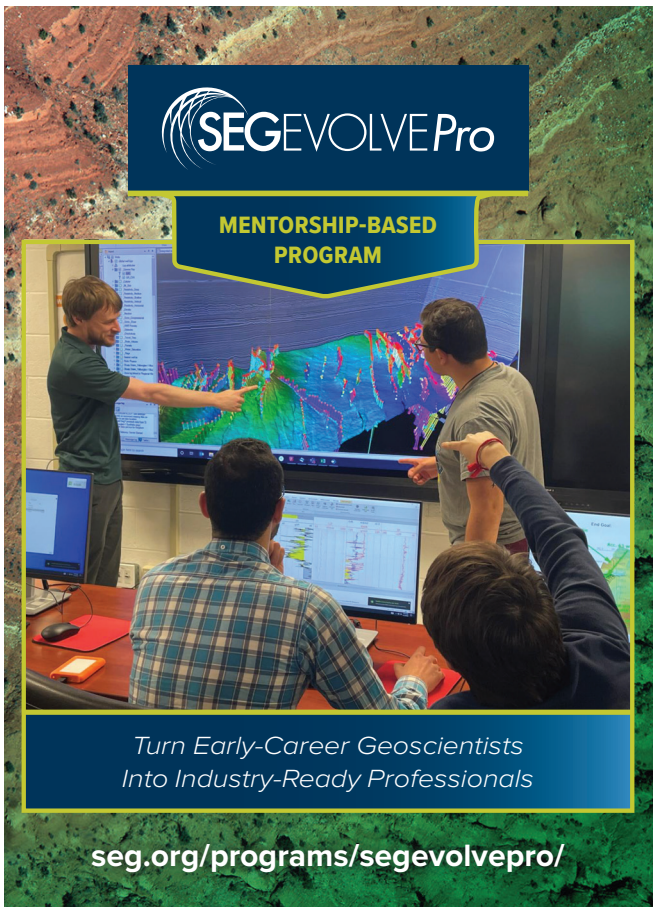

Downloaded from http://pubs.geoscienceworld.org/seg/tle/article-pdf/45/2/73/7765650/tle-v45-n2.pdf by Shivaji Maitra on 19 February 2026

Memorial

José (Pepo) R. Arce Alleva
5 January 1970 to 2 December 2025



Jose Pepo Arce answering audience questions during the Near-Surface Geophysics Student Career Panel at the International Meeting for Applied Geoscience & Energy, August 2025.

"Hello. How are you doing, my friend?" Instantaneously warm, inviting, and genuine, this greeting was precisely how Pepo was. He greeted everyone with this heartfelt question, and everyone who received it felt the warmth and sincerity behind it.

First and foremost, Pepo was a loving and devoted family man. If you sat and talked with Pepo, he would tell you about his wonderful wife, Maria Fé, and if you were fortunate, you would get to meet her at a conference or elsewhere. You would instantly be struck by how perfect Pepo and Maria Fé were together. In fact, years after first meeting them together, you'd still remember how wonderful they were as a team. Pepo would also talk about his son, José Francisco, who was determined, like Pepo, not to become a geophysicist. Before he went to university in the Netherlands, we met him at SEG's 89th annual meeting in San Antonio, Texas. His daughter, Ana Paula, has been studying medicine in Lima and is a brilliant student. His brother, Gianfranco, has always been involved in and engaged with the success of Arce Geofísicos, alongside the rest of the family, and will continue its legacy. Pepo loved to talk about his family. They were his heart and soul.

Pepo had many interests outside geophysics and geosciences, such as an affection for animals, particularly cats. He supported a cat shelter in Lima that rescued hundreds of kittens over the decades. A passion for airplanes and flying motivated him to obtain a pilot's license and fly his own airplane. Many who knew Pepo probably had the chance to experience his passion for wine firsthand and share it with him. Pepo was a true Renaissance man.

Pepo was a second-generation geophysicist who was determined that he would be a computer scientist instead. His father, also Jose but known as Pepe, was an influential and renowned geophysicist who started Arce Geofísicos in 1960. He knew better, as most fathers do. Pepo went to university in the United States, where he received a BSc in geology and geophysics from the Missouri University of Science and Technology in Rolla. He went on to receive his MSc in geophysical engineering from the University of Arizona, where he met and worked with some of the biggest names in mineral geophysics, and where he found that he, too, had developed a love for geophysics.

Returning home to Lima, he worked with his father at their joint company, Arce Geofísicos, and in 2010, began running the business after his father retired. An office in Medellín, Colombia, opened at that time, and a recent office in Argentina was just launched. He learned the business side of geophysics from his father. He took over running the family business, delivering tens of thousands of geophysical surveys across South and Central America, and consulting in Canada, expanding the range of services that the company offers with bold investments in state-of-the-art instrumentation and software, always with an eye to innovative applications.

Pepo was always interested in advancing technologies and seeking new ways to apply them through his company. While Pepo's expertise covered virtually all geophysical methods, above all, he had a knack for navigating with ease between geological issues and geophysical applications across sectors such as mining, geotechnical engineering, and groundwater. He approached every problem with enthusiasm and a high level of technical skill. His business expertise and consistent drive helped Arce Geofísicos expand and grow across the Americas.

Pepo will be remembered for his equanimity and generosity. Always ready to offer support, he taught his colleagues to seek solutions rather than assign blame. His resilience was contagious; through his guidance, he inspired individuals to reach their full potential, strengthening the entire team. He was a champion of the entrepreneurial spirit within his profession, promoting healthy competition that fostered collective growth. Whether in professional practice or business ventures, Pepo always offered the proper counsel at the right moment.

Pepo's influence extended beyond business. He always valued education and felt that part of his mandate was to give back and to help others learn about geoscience, especially geophysics. He taught geophysics at the Peruvian Catholic University for decades and would be found at events conducting workshops to help educate the next generation of geophysicists. Recently, he pushed to make sustainability part of the geoscience curriculum and to make it possible for the SEG Honorary Lecture (HL) to visit that university. During the HL visit,

Downloaded from http://pubs.geoscienceworld.org/seg/tle/article-pdf/45/2/73/7765650/tle-v45-n2.pdf by Shivaji Maitra on 19 February 2026

what stood out was the students' high regard for Pepo, expressed with respect and gratitude.

Pepo was also involved with geoscience societies for decades, reaching high levels of leadership and demonstrating an eagerness to help create and enhance the work of those with whom he collaborated. He was involved with and became president of his home society, the Peruvian Geological Society, in 2012–2013, as well as the chair of the Latin American Geological Congress in 2008. Through the decades, he served in leadership roles and helped to lead various Congresses through the years. He was a longtime member of the Society of Economic Geologists, was elected a fellow, became a regional vice president for South America in 2015, and was active on many committees. Pepo was elected president of the Society of Economic Geologists, beginning in 2026, and served as president-elect until his untimely passing. Pepo was a member of the Society of Exploration Geophysicists since high school, when his father signed him up. He was proud of his record of continuous attendance at the SEG Annual Meeting and IMAGE since becoming a member in the late 1980s, with only two exceptions. Over the years, not only was Pepo active at annual meetings, but he also led numerous SEG committees, including the Justice, Equity, Diversity, and Inclusion Committee, the Meetings Review and Planning Committee, and the Field Camps Subcommittee. He was an active member of the Latin America Regional Advisory Committee and served several times as District Representative on the SEG Council. He served as guest editor for a special section on mining and minerals exploration in the journal *Interpretation* and on numerous task forces to address specific challenges, demonstrating great enthusiasm and strategic aptitude. He ran for a director-at-large position on the SEG Board of Directors in 2022 and for treasurer in 2024. Most important to the authors of this Memorial, Pepo served as chair of the Mining Committee in 2015–2016 and the Near-Surface Technical Section in 2018–2019, and was active with both groups throughout his life, leading technical sessions, mentoring students and early-career members, and sponsoring various events. He was a positive force for both communities and has deeply impacted many lives across the globe through them.

At IMAGE 2025, he served as co-chair of several technical sessions and was a generous panelist at the Near Surface pavilion, gracefully conveying his legendary positivity to students and young professionals. With him by their side, any difficulty seemed easily surmountable. Yet, his untimely passing leaves a void that today seems impossible to fill.

He is survived by his wife of 27 years, Maria Fé, their children, José and Ana, a fur family of adoring cats, fellow aviators, and an immeasurebly long list of students and colleagues whose lives are better for having known him.

Downloaded from http://pubs.geoscienceworld.org/seg/tle/article-pdf/45/2/73/7765650/tle-v45-n2.pdf by Shivaji Maitra on 19 February 2026







Downloaded from http://pubs.geoscienceworld.org/seg/tle/article-pdf/45/2/73/7765650/tle-v45-n2.pdf by Shivaji Maitra on 19 February 2026

Membership

Applications for Active membership have been received from the candidates listed below. This publication does not constitute election but places the names before the membership at large in accordance with SEG's Bylaws, Article III, Section 5. If any member has information bearing on the qualifications of these candidates, it should be sent to the SEG president within 30 days.

Requirements for membership

Active: Eight years of professional experience practicing or teaching geophysics or a related scientific field. Membership applications and details of other types of membership, including Associate, Student, and Corporate, may be obtained at https://seg.org/membership.

For Active membership

Abdelaziz, Aser (Egypt, Arab Republic)
Aghazade, Kamal (Poland)
Akosah, Fred (Ghana)
Al-Harrasi, Othman (Oman)
Barron, Sheldon (USA)
Caulfield, Daniel (Canada)
Chen, Hang (USA)
Cheng, Tianjian (China)
Cordray, Rob (USA)
Coulibaly, Pape Moussa (Senegal)
Dey, Ayon (USA)
Dubey, Chandra (India)
Edmunds, Alexander Chase (Canada)
ElSaaid, Mohamed (Egypt, Arab Republic)
Funk, Jonathan (USA)
Gonzalez, Magdalena (USA)
Graul, Patrick (USA)
Guo, Yu (China)
Hansen, Benn (USA)
Huang, Shang (Canada)
Imana, Marcello (Sweden)
Jaiswal, Abhinav (India)
Kumar, Ankit (Malaysia)
Larcher, Alix (France)
Lewis, Olivia (USA)
Lin, Xulu (Australia)
Liu, Lichao (China)
Liu, Zhonghan (China)
Machado, Gabriel (USA)
Mueller, Emery (USA)
Obosu , KingChrist (Ghana)
Pare, Andrew (USA)
Pham, Dung (Viet Nam)
Purdue, Gregory (Canada)
Siegel, Jacob (USA)
Uviase, Efe (Nigeria)
Vega Ramirez, Luis Angel (Mexico)
Vien, Nam (Canada)
Wang, Meng (China)
Wang, Ying (Norway)
Zhang, Chong (China)



Downloaded from http://pubs.geoscienceworld.org/seg/tle/article-pdf/45/2/73/7765650/tle-v45-n2.pdf by Shivaji Maitra on 19 February 2026

Meetings Calendar

See https://seg.org/events/events-calendar for the latest updates.

FEBRUARY 2026

10–12 FEB
FWI Beyond Structure Interpretation — Benefits and Challenges
https://seg.org/calendar_events/fwi-beyond-structure-interpretation-benefits-and-challenges
Houston, Texas, USA

10–12 FEB
SEG | DGS Workshop: Bridging the Gap: Geosciences to Engineering
https://seg.org/calendar_events/bridging-the-gap-geosciences-to-engineering
Al Khobar, Saudi Arabia

18–20 FEB
2026 NAPE Summit
https://napeexpo.com/summit
Houston, Texas, USA

23–27 FEB
8th International Workshop on Rock Physics
https://www.8iwrp.auckland.ac.nz
Auckland, New Zealand

MARCH 2026

16–18 MAR
Realizing the Energy Potential of Angola Symposium
https://seg.org/calendar_events/energy-potential-angola-margin-2026
Luanda, Angola

23–25 MAR
6th Net Zero Emissions Workshop
https://seg.org/calendar_events/net-zero-emissions-workshop-2026
Virtual

30 MAR–1 APR
Carbon Capture, Utilization, and Storage (CCUS)
https://ccusevent.org/2026
The Woodlands, Texas, USA

30 MAR–1 APR
Near Surface Modeling, Imaging, and Characterization
https://seg.org/calendar_events/near-surface-modeling-imaging-and-characterization
Al Khobar, Saudi Arabia

APRIL 2026

14–16 APR
8th International Conference on Engineering Geophysics
https://conferences.uaeu.ac.ae/iceg2025/en/index.shtml
Al Ain, UAE

15–17 APR
Asia Pacific Offshore Exploration Symposium
https://seg.org/calendar_events/the-asia-pacific-deep-water-and-offshore-exploration-adeep-symposium
Bali, Indonesia

21–23 APR
Next Generation Land & Shallow Water Acquisition Technologies
https://seg.org/calendar_events/land-shallow-water-acquisition-technologies-2026
Abu Dhabi, UAE

28–30 APR
Mediterranean and Red Sea Exploration Summit
https://seg.org/calendar_events/mediterranean-red-sea-2026
Sharm El Sheikh, Egypt

MAY 2026

4–7 MAY
Offshore Technology Conference (OTC)
https://2026.otcnet.org
Houston, Texas, USA

6–8 MAY
Artificial Intelligence & High-Performance Geophysics Workshop
https://events.sbgf.org.br/index.php?w=AIHPG26#pages
Natal, Rio Grande do Norte, Brazil

12–14 MAY
New Advances in Seismic Interpretation
https://seg.org/calendar_events/new-advances-in-seismic-interpretation
Muscat, Oman

18–21 MAY
Advancing Data Analytics and Machine Learning for Exploration Geophysics
https://seg.org/calendar_events/advancing-data-analytics-machine-learning-for-exploration-geophysics
Houston, Texas, USA

JUNE 2026

3–4 JUN
Innovative Geoscience Across the Upstream Lifecycle
https://seg.org/calendar_events/innovative-geoscience-throughout-the-upstream-lifecycle-in-shallow-water-and-transition-zones
Brunei

16–17 JUN
SEG/SPE Injection-induced Seismicity Workshop
https://seg.org/calendar_events/seg-spe-injection-induced-seismicity-workshop
Banff, Alberta, Canada

22–24 JUN
Unconventional Resources Technology Conference (URTeC)
https://urtec.org/2026
Houston, Texas, USA

29 JUN–2 JUL
Projecting the Future of Subsurface Characterization with Seismology: Technical Dialogues from the Next Generation of Geoscientists
https://seg.org/calendar_events/projecting-the-future-of-subsurface-characterization-with-seismology
Virtual

Downloaded from http://pubs.geoscienceworld.org/seg/tle/article-pdf/45/2/73/7765650/tle-v45-n2.pdf by Shivaji Maitra on 19 February 2026

seg.org

Refreshed and Enhanced!

Launches 1 March 2026



SEG

LEVEL UP your geophysics skills with **FREE Virtual Lectures**



Geophysical Contribution for Sustainable Agriculture and Environmental Management

Middle East and Africa Honorary Lecturer

Ahmed Elshenawy • 18 Feb • 12 Mar



From Dictionary Learning to Deep Learning in Geophysical Technology

South and East Asia Honorary Lecturer

Jianwei Ma

22 Mar • 8 Apr

seg.org/events/events-calendar

Select 'Lecture' from event format

Introducing the New SEG Communications Center!

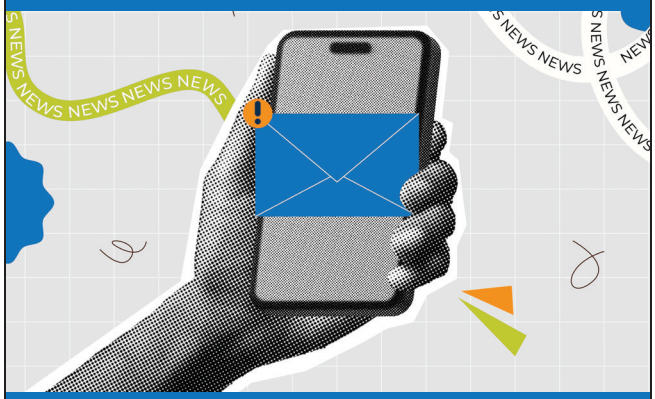

We are excited to announce the launch of our **new communications center**, designed to help us better tailor our updates to your specific interests!

Review and complete your preferences in the new center to ensure you receive the most relevant information, including SEG newsletters, event announcements, and professional updates.

Set Your Email Preferences ›

Downloaded from http://pubs.geoscienceworld.org/seg/tle/article-pdf/45/2/73/7765650/tle-v45-n2.pdf by Shivaji Maitra on 19 February 2026

The tools, people, and moments that built a geophysics career

In episode 281 of SEG's Seismic Soundoff podcast, Betty Johnson shares how her early career in gravity and magnetics grew from curiosity, hands-on learning, and rapidly changing technology. She explains how potential field methods remain valuable for addressing energy, water, and climate challenges because they are affordable, scalable, and deeply rooted in the earth's history. Listen to the full episode, as well as any past episode, at at https://seg.org/podcasts.

Andrew Geary: How did the energy crisis of the 1970s change the way you approached your work?

Betty Johnson: I started my career in the middle of the crisis, so I did not really get to experience that shift. In fact, I probably got my job because of the crisis, because it was all hands-on deck at the time. And I was quite driven by a patriotic duty to work in oil and gas. It's hard to imagine that because we don't think about that these days. At the time there was a lot of capital being invested in exploration and particularly frontier areas, which is why gravity and magnetics was booming — as well as all the technological shifts causing a lot of geophysics to be acquired and interpreted. During that time, there were many offshore lease sales all around the country. There were many spec surveys and even spec interpretations happening, so we just had an endless queue of data to work on. A lot of those spec surveys actually introduced me to my colleagues in the industry. Many of those are lifelong friendships now.

Geary: Multidisciplinary work is something I feel is a little buzzwordy today. Did you find you understanding that back then unique?

Johnson: I think as a gravity and mag interpreter, you have to understand the other disciplines that you're working in, and particularly geology. While I was really driven by the curiosity of geophysics, I was equally driven by the curiosity of geology. I went to college in the Los Angeles Basin. My first job was in the Los Angeles Basin, and I worked there for nearly 20 years. You're surrounded by geology. At the time, there were a lot of controversial field puzzles that we would go out in the field and argue about, and I just got sucked into that. I think having that good geology understanding — particularly tectonics — is absolutely critical in gravity and mag. As we moved offshore, that cross-disciplinary approach to many of our offshore projects became fundamental — not only because you had to work with your colleagues, but in order to interpret the gravity and magnetic data, you really had to understand all the different aspects of the subsurface. And then of course, there's the people side of things and being able to understand the business. Of course, that came over time throughout my career, but that's an equally important, if not more important, aspect of the multidisciplinary approach. I would say it's probably even more important now than it was when I started.



Geary: How have you seen the culture of geophysics changing the workplace, and where do you hope it progresses now that you're out of it?

Johnson: We've experienced a lot of change, and I address some of that culture in the article (*The Leading Edge*, vol. 44, no. 9, 738–741). But today there's a critical mass of women in the industry, and geophysics is culturally very diverse. Geophysics as a field is global, and I think the globalization of geophysics has actually contributed to the diversity in the field. So things have changed a lot, including company policies and benefits. In the latter part of my career, I was fortunate that I worked for Chevron. Chevron has always been on the cutting edge of diversity and inclusion. And so that was a privilege to not only work in that environment, but as a talent manager to be able to champion that. And professional organizations like SEG are also realizing the importance of diversity and inclusion as an ethical issue. And that is also making a difference. There's still a lot of work to be done, but I think the real key to that work is in the educational pipeline. Earth science as a whole — geophysics is no exception — is a very leaky pipeline, particularly in the United States. As a talent manager, we always had a pool that had far less women to draw from than males.

Geary: After all these decades, why do you think gravity and magnetic methods still are important?

Johnson: Well, fundamentally, I have this belief that the earth's gravity field actually embeds the entirety of geologic history. And our job is to decode that. So, if you believe that, you know that using the gravity data is part of telling that story. On a more practical level, gravity and magnetics is significantly less expensive than many other geophysical techniques, and it can be done at a scale that often cannot be done with the other geophysical techniques — and also in areas that are challenging to access, whether that's physical access or political access. And literally we have global data sets that can be used for various kinds of problems, so that keeps our specialty alive. TLE

Downloaded from http://pubs.geoscienceworld.org/seg/tle/article-pdf/45/2/73/7765650/tle-v45-n2.pdf by Shivaji Maitra on 19 February 2026

Rising to the Challenge...

"We believe in challenging the industry status quo in everything we do. The way we challenge the status quo is by making our software accurate, scientifically rigorous,fast, simple to use and easy to understand."

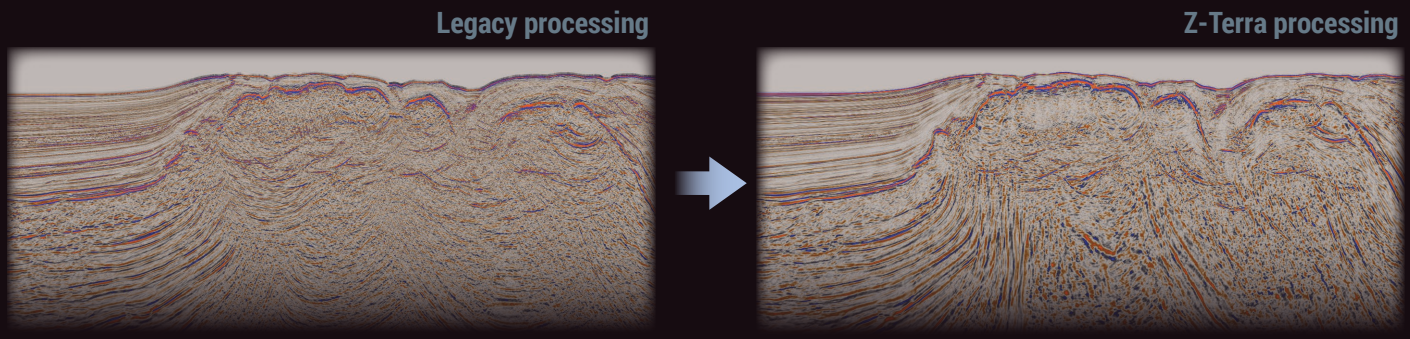

Data courtesy of MCG

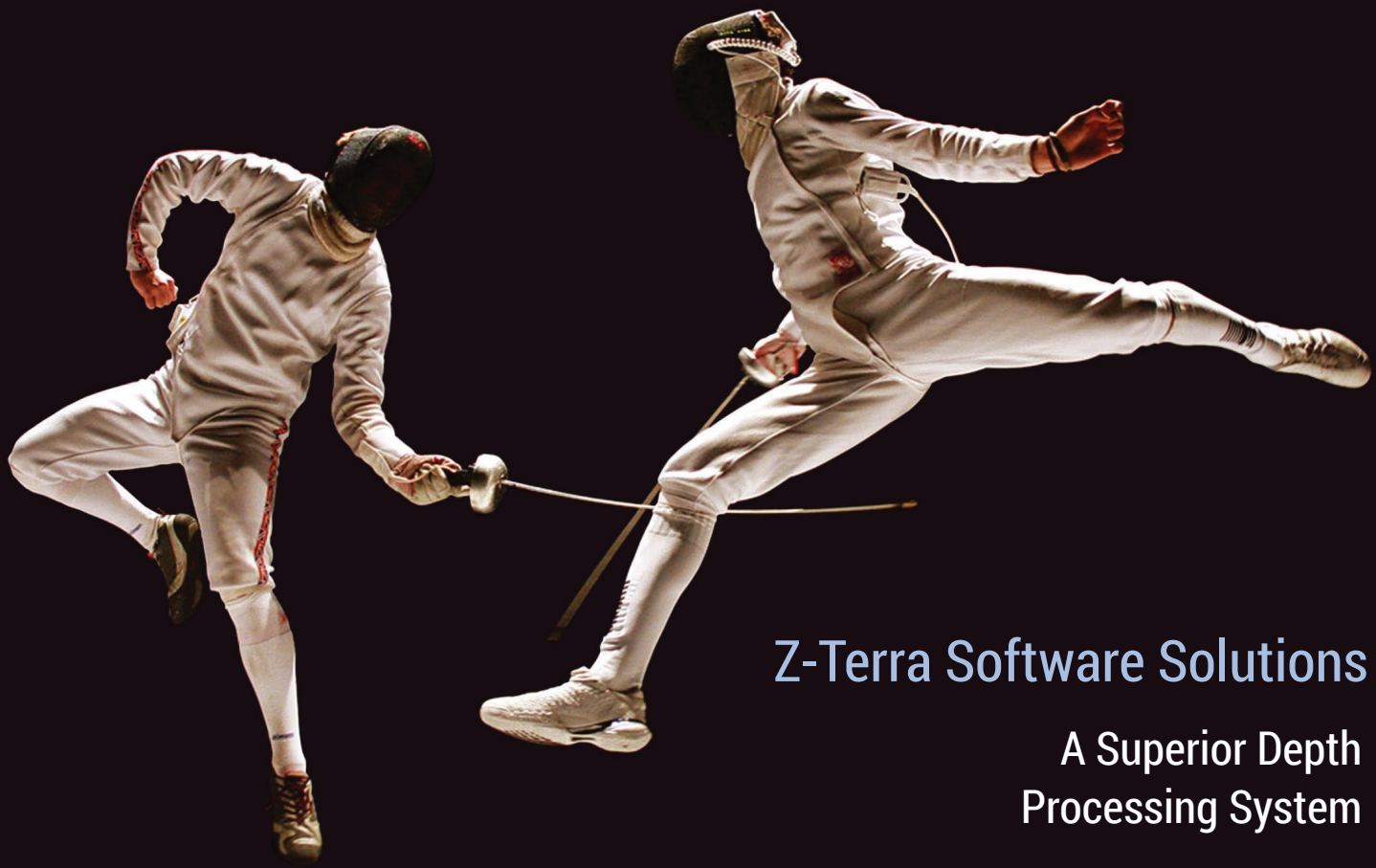

Z-Terra Software Solutions

A Superior Depth Processing System

HOUSTON
17171 Park Row, Suite 247
Houston, TX 77084
USA

THE HAGUE
Stationsplein 6, 5th Floor
Voorburg 2270 JB
The Netherlands

RIO DE JANEIRO
Av. Nilo Pecanha 50
Edificio De Paoli, Sala 1616
Rio de Janeiro, RJ Brazil

BUENOS AIRES
Av. Lima 575, 8th floor
Buenos Aires C1073AAK
Argentina

KUALA LUMPUR
Dialog Tower, No. 15, Jalan PJU 7/5,
Mutiara Damansara, 47810 Petaling Jaya,
Selangor Darul Ehsan, Malaysia

www.z-terra.com

Downloaded from http://pubs.geoscienceworld.org/seg/tle/article-pdf/45/2/73/7765650/tle-v45-n2.pdf by Shivaji Maitra on 19 February 2026